

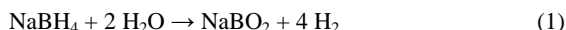
HYDROGEN GENERATION VIA COMBUSTION OF METAL BOROHYDRIDE/ALUMINUM/WATER MIXTURES

Evgeny Shafirovich, Victor Diakov, and Arvind Varma

School of Chemical Engineering, Purdue University
480 Stadium Mall Drive, West Lafayette, IN 47907

Background and Approach

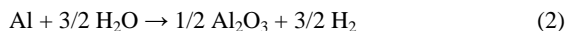
Alkali and alkaline earth metal borohydrides are known to be an excellent source of hydrogen, which can be generated by reactions of these compounds with water or oxidizing agents. Hydrolysis of sodium borohydride is a well-known process [1], extensively studied for hydrogen generation. Aqueous alkaline NaBH_4 solutions are stable and their contact with selected catalysts leads to the reaction



Water in this process is simultaneously a reactant and an additional source of hydrogen. As a result, borohydrides provide high hydrogen yield (>10 wt.% for stoichiometric mixtures), which makes them attractive for applications. However, moderate exothermicity of the metal borohydrides hydrolysis is an impediment for combustion-based hydrogen generation.

Recently, hydrogen-generating pyrotechnic compositions were proposed to feed fuel cells for portable electronics [2]. In such solid mixtures, hydrogen is generated by combustion reactions between alkali metal borohydride (or alkaline earth metal borohydride) and oxidizing salt (e.g., ammonium perchlorate, alkali metal perchlorate, alkaline earth metal perchlorate). The reactions are highly exothermic, easily initiated, and do not require any catalyst, which makes them cost effective and attractive for portable electronics applications. However, stoichiometric mixtures of the proposed reactants exhibit low hydrogen yield while the mixtures with high content of metal borohydride do not burn.

An alternative approach uses combustion of nanoscale aluminum with gelled water for hydrogen generation [3]. Here, water acts as an oxidizer for Al and simultaneously as the sole source of hydrogen. The adiabatic combustion temperature of $\text{Al}/\text{H}_2\text{O}$ stoichiometric mixture is close to 3000 K (at pressure 1 atm), which indicates that the heat release is quite sufficient for self-sustained combustion. However, the use of nanoscale Al powder and gelling of water (for example, by adding polyacrylamide) are the necessary conditions for combustion of $\text{Al}/\text{H}_2\text{O}$ mixture. The use of nanopowder decreases the ignition temperature of Al, while gelling leads to significant superheating of water during combustion. Hence, the mixture ignites easily and burns in inert atmosphere, producing hydrogen:



Unfortunately, low hydrogen yield of the $\text{Al}/\text{H}_2\text{O}$ system (theoretical limit 5.6 wt.% for the stoichiometric mixture) is a drawback of this method.

To reach high hydrogen yield and combustion efficiency, we use metal borohydride/aluminum/water mixtures, in which water acts as an oxidizer for both aluminum and metal borohydride and simultaneously as a source of hydrogen, metal borohydride is an additional hydrogen source, and aluminum enhances reaction exothermicity. Nanoscale aluminum powders are used to ensure high combustion efficiency. Along with the three reactants, the mixtures include, in quantities about 1 wt.% each, a gelling agent (e.g., polyacrylamide) and a stabilizer (e.g., NaOH) to prevent hydrolysis of borohydride at room temperature.

Thermodynamic calculations were conducted for $\text{NaBH}_4/\text{Al}/\text{H}_2\text{O}$ system using THERMO software [4]. Figure 1 shows adiabatic combustion temperature and H_2 yield as a function of $\text{Al}/(\text{NaBH}_4 + \text{Al})$ mass ratio at pressure 1 atm. The H_2O fraction was taken to obtain stoichiometric ratios for reactions (1) and (2). Thus, the values of Al mass fraction 0 and 100% in Fig. 1 correspond to the reactions (1) and (2), respectively. With addition of Al, combustion temperature increases from the melting point of NaBO_2 (1239 K) to the melting point of Al_2O_3 (2327 K), and then to ~2900 K. The temperature curve slope increases significantly when Al fraction reaches ~50%, which corresponds to the boiling point of NaBO_2 (1707 K). This implies that Al-rich mixtures (50-70%) may exhibit high combustion efficiency and yet provide relatively high hydrogen yield (7-8%).

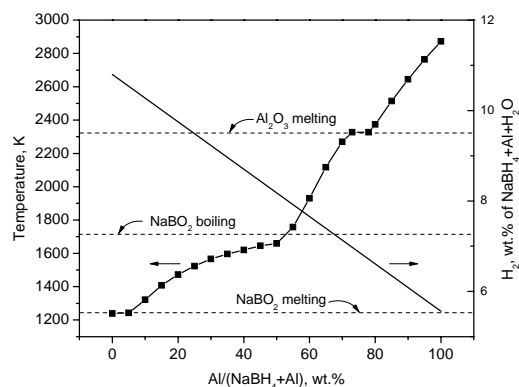


Figure 1. Adiabatic combustion temperature and hydrogen yield of $\text{NaBH}_4/\text{Al}/\text{H}_2\text{O}$ system, predicted by thermodynamic analysis ($P = 1$ atm).

Experimental

Experiments on combustion of $\text{NaBH}_4/\text{Al}/\text{H}_2\text{O}$ system were conducted in a 3 L stainless steel chamber equipped with hot-wire ignition system, pressure transducer and windows for reaction monitoring. Preparation of mixtures included addition of 2 wt.% NaOH and 3 wt.% polyacrylamide ($M_w = 5 \times 10^6$) in distilled water, and mixing the resulting gel with NaBH_4 and Al powders. Passivated Al nanopowder (average particle size 80 nm, free metallic aluminum 83%; Nanotechnologies) was used in the experiments. The obtained mixture was placed in a quartz cylinder (height 3 cm, diameter 1 cm) and ignited by Nichrome coil inside the chamber. The experiments were conducted in argon at initial pressure of 1 atm. A high-speed video camera (Phantom 5.1) was used for visualization of combustion and measurement of front velocity. The chamber pressure was monitored using a pressure transducer and the resulting gas composition was analyzed by gas chromatography.

Results

Experiments with various Al/NaBH_4 mixture ratios at stoichiometric water contents show that addition of Al significantly stimulates combustion. Reaction with no aluminum addition requires permanent heating by the igniter while Al-rich mixtures burn vigorously, similar to typical SHS processes (Fig. 2). Gas generation leads to increase in chamber pressure (Fig. 3), and analysis shows that the evolved gas is essentially hydrogen. Table 1 compares measured hydrogen yield in different mixtures with the theoretical values.

In summary, the used sodium borohydride/aluminum/water mixtures are combustible and exhibit higher hydrogen yield than

theoretically possible for reaction (2). Additional improvements are being investigated by using different borohydrides and by tuning the reaction conditions.

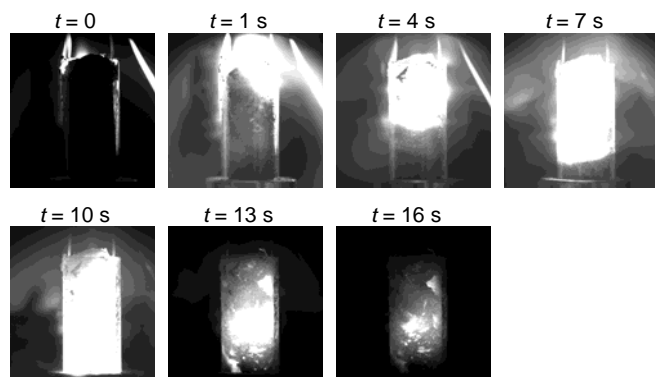


Figure 2. Images of combustion front propagation in mixture $\text{NaBH}_4\text{:Al:H}_2\text{O} = 1\text{:}2\text{:}3$ (mass ratio).

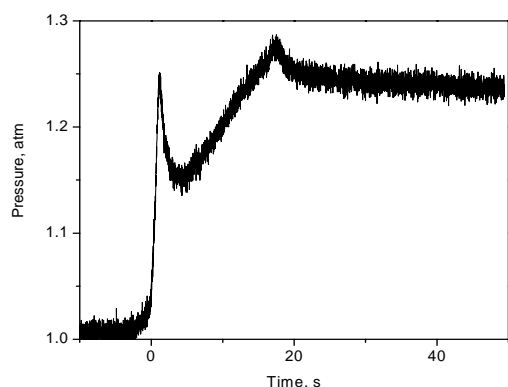


Figure 3. Chamber pressure variation during combustion of mixture $\text{NaBH}_4\text{:Al:H}_2\text{O} = 1\text{:}2\text{:}3$ (mass ratio).

Table 1. Theoretical and Experimental Hydrogen Yield for $\text{NaBH}_4\text{/Al/H}_2\text{O}$ Combustion.

Al : NaBH_4 mass ratio	Al : (Al+ NaBH_4) wt. %	H ₂ yield wt. %		Efficiency %
		theoretical	measured	
0 : 1	0	10.8	8.3*	77*
1 : 3	25	9.5	6.5	68
1 : 2	33	9.1	6.0	66
1 : 1.5	40	8.7	6.7	77
1 : 1	50	8.2	6.3	77
1.5 : 1	60	7.7	5.5	71
2 : 1	67	7.3	5.4	74
3 : 1	75	6.9	5.1	74
1 : 0	100	5.6	2.8	50**

*Obtained with continuous external heating.

**Compares well with literature data [3].

References

- (1) Schlesinger, H.I.; Brown, H.C.; Finholt, A.E.; Gilbreath, J.R.; Hoekstra, H.R.; Hyde E.K. *J. Am. Chem. Soc.*, **1953**, 75, 215.
- (2) Desgardin, N.; Perut, C.; Renouard, J. *U.S. Patent Application* 20040065865, *European Patent* 1405824, **2004**.
- (3) Ivanov, V.G.; Leonov, S.N.; Savinov, G.L.; Gavriluk, O.V.; Glazkov, O.V. *Combust. Explos. Shock Waves*, **1994**, 30, 569.
- (4) Shiryayev, A.A. *International J. Self-Propagating High-Temperature Synthesis*, **1995**, 4, 351.

ORGANOMETALLIC COMPLEXES FOR HYDROGEN STORAGE

Yufeng Zhao, A.C. Dillon, Y.-H. Kim, M.J. Heben, and S.B. Zhang

National Renewable Energy Laboratory, Golden, Colorado 80401

Introduction

Hydrogen is a renewable energy source that could replace petroleum to fuel cars, with a concomitant improvement in air quality.¹ However, without a suitable matrix, it's not safe to compress this highly flammable gas at the extremely high pressures required for feasible on-board vehicular storage. For decades, researchers have been struggling with metal-hydrides, chemical hydrides and carbon adsorbents. Although there has been some promising research,²⁻⁵ practical hydrogen storage for vehicular applications is still far from being achieved. The simple principle for rechargeable hydrogen storage at near ambient temperature and pressure has not yet been demonstrated. Thus, the technological community realizes a breakthrough is necessary. Here we predict theoretically both a novel concept and realistic nanoscale materials that fulfill this purpose.

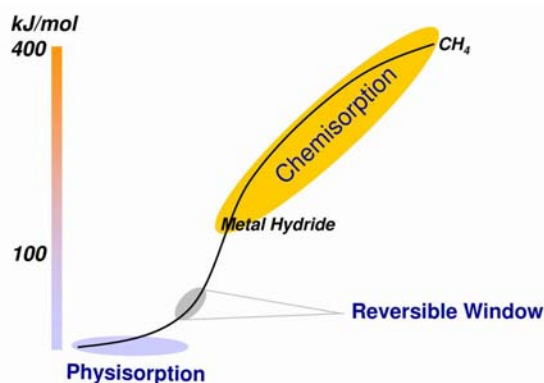


Figure 1. Schematic spectrum of hydrogen binding energies for different types of adsorbents.

There are two key parameters for hydrogen storage. The first is the binding energy relative to free H_2 molecules (not to free H atoms). The second is the capacity or weight percentage (wt%) of retrievable hydrogen gas from the material system (medium plus hydrogen). Ultimately, the weight of the container must also be included for the overall system calculation.

In nature, most hydrogen exists in chemical compounds like H_2O and CH_4 . The binding energy of hydrogen in compounds ranges from ~ 100 kJ/mol in metal-hydrides to ~ 400 kJ/mol in CH_4 , as shown in Fig. 1. Because the binding energy of hydrogen in metal-hydrides represents a minimum for in elements known to store hydrogen, light metals have been investigated as hydrogen storage media for nearly half a century. However, 100 kJ/mol is still too high for practical use as the extraction of hydrogen from metal hydrides requires elevated temperatures.⁴ Although catalysts may improve the kinetics of the releasing process⁶ by lowering the barrier, they can not reduce the binding energy.

Hydrogen storage on porous carbon materials⁷ via physisorption has also been studied at great length. Recent activity in this area was inspired by the discovery of carbon nanotubes⁸ and other nanoscale carbon materials, e.g., carbon nanohorns.^{9,10} However, physisorption (5-10 kJ/mol) on carbon materials is too weak to stabilize a sufficient

amount of hydrogen at room temperature and near ambient pressures.¹¹ Researchers have tried to enhance the van der Waals binding by increasing the surface area in contact with the H_2 molecules.¹² This, however, unavoidably decreases the hydrogen weight capacity. Induced dipole or charge transfer effects are other possibilities to enhance binding based on electrostatic interactions.¹³ However, currently there is no evidence that a moderate binding energy can be achieved with a significant hydrogen capacity.

The ideal binding energy that allows for rechargeable hydrogen storage at room temperature and near ambient pressure is ~ 20 -40 kJ/mol (Fig. 1). This binding energy is stronger than that expected for physisorption but weak compared to that of chemical or metal hydrides. Such an intermediate binding energy was demonstrated in the 1980s, by Kubas et al.¹⁴ The so-called "Kubas complex" $W(CO)_3(P^iPr_3)_2(H_2)$ represents a fundamentally new concept of coordination between a transition metal (TM) and a H_2 ligand, which does not dissociate into hydrides. However, the H-H bond is noticeably elongated with respect to the free molecule. The stability of the molecular hydrogen ligand (dihydrogen) critically depends on the properties of the TM atoms. Empty TM d -orbitals, can accept a small fraction of the H-H bond charge, resulting in an intermediate binding energy. The importance of such a binding energy for reversible hydrogen adsorption was later realized.¹⁵ Kubas complexes are generally formed with heavier transition metal atoms, e.g., W, Cr, and Mo, and the binding energy of H_2 is as large as 70-90 kJ/mol,¹⁶ which will not satisfy the requirements for vehicular hydrogen storage. As we showed recently in a systematic investigation of all of the 3- d TM atoms,¹⁷ the binding energy of the dihydrogen depends on the TM atoms to which it binds, and can range from 20 to 130 kJ/mol. Therefore, the ideal binding energy is easily achieved by choosing particular transition metals.

Still the right binding energy alone does not satisfy all of the on-board hydrogen storage requirements. Most transition metals are very heavy and adsorb small quantities of hydrogen at moderate temperatures. Recently, a few groups found that multiple dihydrogens may bind to free TM atoms.^{18,19} So far this research has not drawn significant attention because free TM atoms will not allow for reversible hydrogen storage due to subsequent cluster formation upon H_2 discharge. The question then is, can the TM atoms be anchored to a light substrate that still allows the TM atoms to bind multiple dihydrogen ligands. This idea is similar to dispersing TM clusters in porous substrates for catalysis applications.²⁰ For hydrogen storage, however, a much higher standard is required for TM dispersion. The substrate materials have to be very light, and the TM should be separated atom by atom instead of existing in clusters. If one examines the periodic table of elements, carbon is probably the best substrate choice for anchoring TM atoms in organometallic complexes. This is because carbon is the sixth lightest of all elements, and carbon rings are known to complex with transition metals.

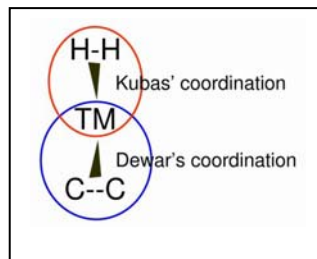


Figure 2. The concept of an organometallic complex with a carbon ligand that could be employed for hydrogen storage. In this sense carbon is used as the supporting material for TM atoms, and the hydrogen that is reversibly retrievable is represented by dihydrogen ligands.

Complexing a TM with a carbon ring may allow organometallic complexes to be the new frontier in vehicular hydrogen storage. As one of the most vigorous fields in modern chemistry, organometallic

chemistry has made vast contributions to a broad variety of technological fields including catalysis²¹, light emitters, molecular devices, and liquid crystals.²² By combining the concepts of Kubas coordination between H₂ and a TM with Dewar's coordination²³ between a carbon ring and a TM, a new class of materials has been predicted. Combining these two types of coordination in one complex (Fig. 2) provides the basis for this article. We will discuss the general principles for the design of organometallic complexes suitable for hydrogen storage and will also provide several examples.

General principle of organometallic design for hydrogen storage

In addition to the basic considerations discussed in the introduction, the organometallic complexes predicted to serve as hydrogen storage media must satisfy the following requirements:

- i) Practically, the complexes must be able to survive multiple charging and discharging cycles. Thus, one of the most critical requirements is the complex stability. That means the interaction of the TM atoms with the supporting carbon material has to be much stronger than the interaction with hydrogen. This ensures that no TM atoms will segregate or coalesce into larger clusters.
- ii) Geometrically, the TM atoms have to be well separated in the complex so that each TM atom has sufficient open space to take multiple dihydrogen ligands. Also considering the macroscopic scope, the materials must allow for efficient volumetric packing.
- iii) In the condition where the TM atoms are well separated, all of the carbon atoms must be employed for supporting the TM atoms. This is required to maximize the hydrogen weight capacity.
- iv) The maximum number of hydrogen atoms (including dihydrogen ligands and hydrides) in an organometallic complex can be estimated by the effective atomic number (EAN) rule:²⁴

$$N_H = 18N_{TM} - 2b - n_{TM}N_{TM} - n_C N_C \quad (1)$$

where $N_{TM}(N_C)$, b , n_{TM} , and n_C are, respectively, the number of TM (carbon) atoms, the number of TM-TM bonds, the number of valence electrons per TM atom, and the number of electrons contributed per carbon atom to the TM orbitals. Notice, that when the TM atoms are completely separated from each other, i.e., $b = 0$, the EAN rule degenerates into the well-known 18-electron rule.

From the EAN rule, one can see that the formation of TM clusters will render the hydrogen storage irreversible. This explains why most bulk TM metals do not have significantly high hydrogen storage capacities at moderate temperatures. Also notice that the lighter TM atoms like Sc and Ti have fewer valence electrons, and hence can accept more hydrogen ligands.

v) Because the EAN rule does not distinguish the hydrides from hydrogen ligands, the chemical properties of the metal should be considered to determine which species will form. From the viewpoint of coordination chemistry, the formation of a hydride more closely resembles a classical covalent bond, whereas, a TM-dihydrogen is a nonclassical coordination. The hydride formation requires unpaired electrons in the TM atom, but the later case occurs when there are empty d -orbitals. Thus the number of hydrides that are formed is often correlated with the number of valence electrons in the TM atom. However, the valence electrons do not necessarily lead to hydride formation. In some cases they are used as a source for back donation, i.e., charge transfer from the TM to the anti-bonding orbital of the H₂ molecule.¹⁵ The formation of a given species is determined by energy minimization that may be calculated.

Practically, TM-hydrides are difficult to extract. However, the existence of hydrides leads to stabilization of the storage medium, and results in only a small increase in weight. But according to Eq. (1), the formation of too many hydrides means that fewer dihydrogen

ligands will coordinate with the TM, and the reversible hydrogen storage capacity will decrease.

Computational method

We use spin-polarized first-principle calculations as implanted in the Vienna Ab initio Simulation Package (VASP).²⁵ Ultra-soft pseudopotential with the PW91²⁶ generalized gradient approximation (GGA) yielding practically the same results to all-electron-like projector augmented-wave (PAW) potential with PBE exchange-correlation functional²⁷. An energy cutoff of 400 eV was also employed. Two cubic unit-cell with dimensions between 16 - 25 Å were used as appropriate for the size of the organometallic molecule, to maintain a similar vacuum region.

Binding of dihydrogen ligands to different transition metal atoms

To predict the broad picture of multiply bound dihydrogens and hydrides to various TM atoms, we first studied a very simple complex based on TM interactions with cyclopentadienyl rings (Cp). Hydrogen then interacts with a single 3- d TM (from Sc to Ni) with a Cp ligand. When a TM atom binds to a Cp ring, an electron is transferred from the former to the latter to complete the last π bond of the Cp ring, giving rise to aromaticity. The charge transfer also enhances the binding through Coulomb interactions. The calculated binding energies for the CpTM systems are $E_b = 3.76, 3.87, 3.47, 2.30, 2.69, 2.97, 3.27$, and 3.02 eV, respectively for Sc, Ti, V, Cr, Mn, Fe, Co, and Ni. The number of dihydrogen ligands (N_{H_2}) and total number of H (N , including those in dihydrogen and hydrides) bound to the CpTM is listed in Table I. Notice that $n_v + N + 5 = 18$, when the 5 electrons contributed by the Cp to the TM orbitals through Dewar's coordination are considered.

Taking CpSc as an example, Sc has only two remaining valence electrons after transferring one to the Cp ring. These valence electrons result in the preferential formation of a dihydride species rather than a dihydrogen ligand. Here, the dihydride is strongly bound (1.31 eV/2H). The resulting hydride complex, Cp[ScH₂], has four empty d orbitals that can bind four additional dihydrogen ligands with a relatively constant and much lower binding energy of about 0.3 eV/H₂ as shown in Table II. For all the rest of the TM atoms, no more than three hydrides are formed. Note, there are up to 9 valence electrons (Ni) but the formation of hydrides does not initially occur. Instead the binding energy per dihydrogen ligand is much larger for Fe, Co, Ni complexes due to back donation.

Table I. Cp Ring Supported TM Atom Binding with Hydrides and Dihydrogen Ligands. The Number of Valence Electrons (n_v) in the Free TM Atoms and the Number of H Atoms (N) Reflect the 18-e Rule including 5 Electrons from the Cp Ring. The Number of Dihydrogen Ligands (N_{H_2}) and Their Average Binding Energy (B) Are also Listed.

	Sc	Ti	V	Cr	Mn	Fe	Co	Ni
n_v	3	4	5	6	7	8	9	10
N	10	9	8	7	6	5	4	3
N_{H_2}	4	3	3	2	2	2	2	1
B (kJ/mol)	30	48	61	52	54	99	112	131

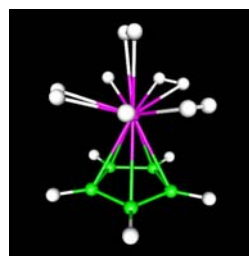


Figure 3. The optimized structure of Cp[ScH₂(H₂)₄], where the Cp ring supported Sc atom binds two hydrides and four dihydrogen ligands. The consecutive binding energy of the four H₂ ligands is shown in Table II.

The fact that the Cp-supported TM atoms can bind multiple dihydrogen ligands shows great potential for the development of a vehicular hydrogen storage system. Sc and Ti bind most strongly with the carbon Cp ring. Also as shown in Table I, these two TM atoms have the highest capacity for dihydrogen ligands, and they bind these dihydrogens with an ideal energy for reversible hydrogen storage at near ambient temperature and pressure. Notice that 6.7 wt % of dihydrogen is stored in $\text{Cp}[\text{ScH}_2(\text{H}_2)_4]$. Unfortunately, according to our calculations, the naked $\text{Cp}[\text{ScH}_2]$ molecules would form a one-dimensional ionic crystal because the TM atoms are positively charged and the Cp rings are negatively charged. Therefore we have to seek a new architecture in order to achieve reversible hydrogen adsorption.

Hydrogen storage in organometallic buckyballs

The CpTM complexes can be considered as basic building blocks for larger organometallic molecules. For example, with the removal of the five H atoms from each Cp ring, we can envision twelve CpTM units symmetrically arranged in a fullerene structure to form a 12-TM coated $\text{C}_{60}\text{TM}_{12}$, resulting in an “organometallic buckyball” (OBB). The distance between adjacent TM atoms is 6 Å, allowing for accommodation of H atoms and multiple H_2 ligands.

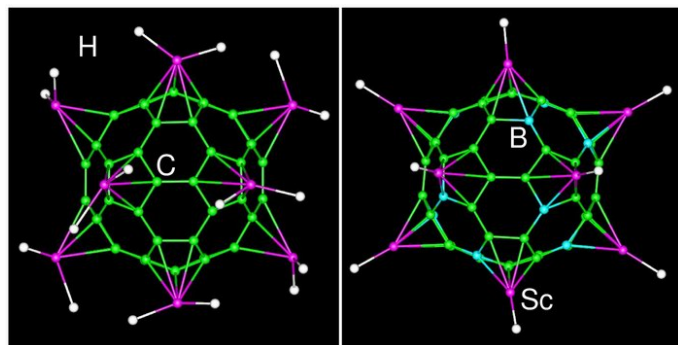


Figure 4. The optimized structure of $\text{C}_{60}[\text{ScH}_2]_{12}$ (a) and $\text{C}_{48}\text{B}_{12}[\text{ScH}]_{12}$ (b), in which multiple dihydrogen ligands are bound to each Sc atom.

The binding between the TM and pentagonal rings of the C_{60} is, however, weaker than in isolated CpTM molecules (e.g., 1.85 eV per Sc in $\text{C}_{60}\text{Sc}_{12}$ versus 3.76 eV per Sc in CpSc). This is because the quasisaromatic nature of the C_{60} molecule must be somewhat rearranged to achieve aromaticity that is centered on the TM-coordinated pentagonal rings. Similar to the Cp system each Sc on the C_{60} also binds with two H atoms to form an OBB hydride $\text{C}_{60}[\text{ScH}_2]_{12}$ (Fig. 4a). Also, similarly to the isolated $\text{Cp}[\text{ScH}_2]$, the $\text{C}_{60}[\text{ScH}_2]_{12}$ can bind four additional molecular H_2 ligands to form $\text{C}_{60}[\text{ScH}_2(\text{H}_2)_4]_{12}$. The four H_2 ligands charge and discharge reversibly at room temperature, with a storage density of 7.0 wt%. In sharp contrast to an isolated $\text{Cp}[\text{ScH}_2]$, however, the $\text{Cp}[\text{ScH}_2]$ units locked in the OBBs will not polymerize spontaneously. The local dipoles of the $\text{Cp}[\text{ScH}_2]$ units are spherically oriented, leaving a net positive charge on the exterior. Coulomb forces will cause the molecules to repel one another, prohibit polymerization, and insure reversible hydrogen storage. Thus, the OBBs offer a novel organization of the CpTM species in space that could greatly impact the field of hydrogen storage.

One can further enhance the stability of the complex by substitutionally doping with boron. Boron-doped buckyballs have been experimentally observed²⁸ and, according to Ref. 29, one can

substitute up to 12 boron atoms in C_{60} to form $\text{C}_{48}\text{B}_{12}$. If OBBs are doped with boron, the B dopants pull more charge from the TM to the buckyball and enhance the TM binding energy. For Sc-coordinated $\text{C}_{48}\text{B}_{12}\text{Sc}_{12}$, the binding energy is increased to 2.7 eV/Sc. Furthermore, this charge transfer leaves each Sc in the hydrogen-bare $\text{C}_{48}\text{B}_{12}\text{Sc}_{12}$ with only one valence electron. Hence, each Sc in $\text{C}_{48}\text{B}_{12}\text{Sc}_{12}$ can bind only a single monohydride to form $\text{C}_{48}\text{B}_{12}[\text{ScH}]_{12}$ (Fig. 4b). The binding energy is then further increased to 3.6 eV/Sc. Then and perhaps most importantly, the B-doped variant permits the binding of five H_2 ligands per Sc, giving rise to the formation of $\text{C}_{48}\text{B}_{12}[\text{ScH}(\text{H}_2)_5]_{12}$. In this case, the amount of H_2 retrievable at room temperature is 8.77 wt%. The binding energies of the 5 H_2 ligands remain approximately the same, 30 kJ/mol (Table II).

To test the thermal stability of the OBB complex as shown in Fig. 4, we have performed high-temperature molecular-dynamics simulations. While the Sc-hydrides in $\text{C}_{60}[\text{ScH}_2]_{12}$ start to form clusters above 600 K, the $\text{C}_{48}\text{B}_{12}[\text{ScH}]_{12}$ remain unchanged at 1000 K for more than 10 picoseconds, indicating the high stability of the latter at room temperature. In this simulation, an H_2 ligand bound to the storage media would desorb within 0.1 picoseconds at 400 K.

Table II. Calculated consecutive binding energies of H_2 molecules (in kJ/mol). In the case of buckyballs, twelve H_2 were added per calculation. A similar trend with the Cp ring case is observed.

	1 st H_2	2 nd H_2	3 rd H_2	4 th H_2	5 th H_2
$\text{Cp}[\text{ScH}_2]$	28.0	27.0	44.4	22.3	
$\text{C}_{60}[\text{ScH}_2]_{12}$	28.9	33.8	40.5	25.1	
$\text{C}_{48}\text{B}_{12}[\text{ScH}]_{12}$	29.9	33.8	28.9	31.8	23.2

TM-coordination of carbon molecules

We now discuss the energetics of different TM interactions with both buckyballs and carbon nanotubes. Changing the geometries of the various structures has variable effects on the hydrogen storage properties.

Basically, the energy of the TM-coated C_{60} becomes lower as the number of TMs interacting with the fullerene increases. That means the TM-coated OBBs are meta-stable structures. Also increasing the number of TM atoms dramatically will ultimately completely destroy the hydrogen storage capacity according to Eq. (1). The key point is whether the meta-stable structure is stable enough at the operational conditions, approximately room temperature and at near ambient pressures.

On C_{60} , a TM atom could possibly coordinate with three different sites: a) on top of a hexagon (η^6 -bonding), b) on top of a pentagon (η^5 -bonding), and c) on a double bond (η^2 -bonding). For a single Sc atom, the binding energy on these three sites are, respectively, 1.75, 1.56, and 1.49 eV, with the η^6 -bonding being most stable. When more Sc atoms are added, however, the situation changes. In the condition that Sc atoms are well separated (meaning no Sc-Sc bonds are formed), the binding energy of η^6 -, η^2 -bonding remains the same, but the binding energy of the η^5 -bonding increases to 1.85 eV/Sc if all 12 pentagons simultaneously complex with Sc atoms. The stability of this configuration is attributed to an elegant rearrangement of the quasisaromatic nature of C_{60} . Now the aromatic nature appears to be shifted to each pentagon of the C_{60} . Specifically, after 1-e is transferred from each Sc to each of the pentagons in C_{60} aromatic five-membered rings are created. Such an effect was first observed in $\text{C}_{60}\text{Li}_{12}$,³⁰ and later was termed as a hexagon isolation rule.³¹ Our OBB complex $\text{C}_{60}[\text{ScH}_2]_{12}$ is similar to $\text{C}_{60}\text{Li}_{12}$ in that the

Sc atom, like the Li atom, transfers one electron to the C_{60} . Unlike $C_{60}Li_{12}$, which is a ground state, the $C_{60}Sc_{12}$ is meta-stable. This is because the Li-Li bond is much weaker than the Sc-Sc bond; therefore, the Sc atoms prefer to form clusters or closely packed islands on C_{60} at elevated temperatures. Notice that Sc metal has the second smallest cohesive energy among the 3-*d* TM metals³² but the second strongest binding with the Cp ring. Therefore, Sc may be the most promising candidate for complexation with C_{60} .

In $C_{48}B_{12}[ScH]_{12}$, two electrons are transferred to the doped buckyball. The enhanced binding of Sc atoms to the B-doped buckyball further stabilizes the OBB against clustering of Sc atoms as indicated by MD simulations described in the previous section. Again isolation of the Sc atoms on the hexagons makes the B-doped buckyball unique as metal cluster formation is unlikely. In contrast, carbon nanotubes (CNTs) do not have pentagons, and TM atoms would form clusters more easily on its highly conjugated surface.

To complete the study, it is necessary to consider an increase in the number of TMs coordinating with C_{60} . For example, if all of the 20 hexagons on C_{60} coordinate with Sc to form $C_{60}Sc_{20}$ (Fig. 5), the binding energy per Sc will be 2.25 eV due to the subsequent formation of 30 Sc-Sc bonds. The length of these Sc-Sc bonds are ~ 3.5 - 3.8 Å compared to 3.3 Å in the bulk metal. This is because the Sc atoms interact more strongly with C_{60} than with each other. According to Eq. (1), the maximum number of hydrogen atoms that a $C_{60}Sc_{20}$ could take is $18 \times 20 - 2 \times 30 - 60 \times 1 - 20 \times 3 = 180$. In our simulation, when hydrogen is added, the longer Sc-Sc bonds tend to break and the shorter ones become even shorter. This results in making more space for hydrogen interactions. However, due to steric repulsion, the total uptake is less than 180 hydrogen atoms but still as many as 150, with 50 of them are hydrides and a reversible hydrogen storage capacity of only 5.7 wt% is achieved.

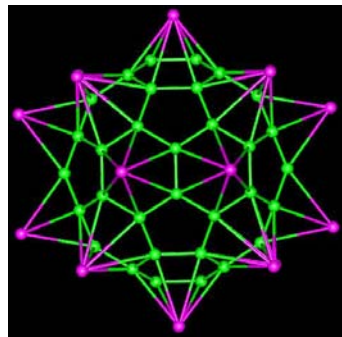


Figure 5. The optimized structure of $C_{60}Sc_{20}$. The twenty Sc atoms (pink) forms η^6 -bonds on top of the hexagons of the C_{60} (green cage). For clarity, the stretched Sc-Sc bonds are not shown.

Additionally, we have found that, Ti atoms do not coordinate with C_{60} in the same manner as Sc, because the Ti-Ti interaction is stronger. Some Ti-C coordination is broken, and shorter Ti-Ti bonds are formed. This means $C_{60}Ti_{20}$ is even more prone to the formation of metal clusters.

Hydrogen storage in clusters of transition metal carbides

Well-controlled coordination of buckyballs with TM atoms may not be easy experimentally because the OBBs are meta-stable structures. Alternatively, we can examine already-existing transition metal carbides for hydrogen storage. These clusters have been well known since the metallocarbohedrene (MetCar), Ti_8C_{12} was discovered.³³ We have also examined here the nanocrystal, $Ti_{14}C_{13}$, as it is also a stable structure.³⁴ In both cases, Ti atoms are dispersed in the carbon cages and coordination between the Ti atoms and H_2 ligands may occur (Fig. 6).

To estimate the hydrogen capacity in these molecules following Eq. (1), one has to pay attention to the different carbon atoms in the two clusters. In Ti_8C_{12} , the carbon atoms occur as dicarbon units, and

the two electrons belonging to each C-C σ -bond do not coordinate with the Ti atom. Therefore, each dicarbon contributes six valence electrons to the Ti orbitals. Then considering of the 18 Ti-Ti bonds, the hydrogen capacity is $N_H = 18 \times 8 - 2 \times 18 - 4 \times 8 - 6 \times 6 = 40$ in Ti_8C_{12} corresponding to a hydrogen capacity of 7.1 wt%. In $Ti_{14}C_{13}$, each C atom contributes 4 valence electrons to the Ti orbitals and there are 36 Ti-Ti bonds. Now we have $N_H = 18 \times 14 - 2 \times 36 - 4 \times 14 - 4 \times 13 = 72$ corresponding to a hydrogen capacity of 8.0 wt%.

Actual simulations give capacities of 34 and 68 H atoms (6.1% and 7.6%), respectively, for Ti_8C_{12} and $Ti_{14}C_{13}$. The lower calculated capacity might be attributed to steric repulsion. The details of these results will be discussed elsewhere.

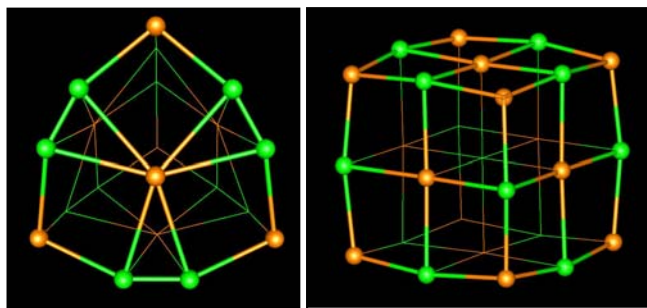


Figure 6. The optimized structure of Ti_8C_{12} (left) and $Ti_{14}C_{13}$ (right). The Ti and C atoms are shown, respectively, in orange and green. For clarity, the front sides are presented in ball-and-stick, the back sides are in wireframes, and no Ti-Ti bonds are shown.

Conclusion

We have theoretically demonstrated hydrogen storage with an optimal binding energy in novel organometallic systems. The most promising result is the high reversible hydrogen capacity at near ambient temperature and pressure. While we have shown a great potential of various nanoclusters including OBBs and MetCars, there is no reason to believe that other systems cannot be constructed based on these same principles. Efficient volumetric packing of these nanoscale structures could offer practical hydrogen storage for vehicular use in the near future. Our theoretical results are supported by our previous experiments, where defective carbon nanotubes with TM clusters adsorb dihydrogen.^{2,35} Also, in other recent experiments it was found that when transition metals are milled in the presence of 10 wt% graphite, the hydrogenation properties are improved considerably.³⁶ This may be due to dihydrogen adsorption on TM atoms that are coordinated with carbon rings.

Acknowledgement. Support for this project comes from the Office of Science, Basic Energy Sciences, Division of Materials Science and the Office of Energy Efficiency and Renewable Energy Hydrogen, Fuel Cell, and Infrastructure Technologies Program of the Department of Energy under Grant No. DE-AC36-99GO10337. Y.Z. and S.B.Z. acknowledge DOE's NERSC for MPP supercomputing time.

References

- (1) Crabtree, G.W.; Dresselhaus, M.S.; and Buchanan, M.V. *Physics Today* **2004**, 57, 39.
- (2) Dillon, A. C., *et al.*, *Nature* (London) **1997**, 386, 377.
- (3) Liu, C., *et al.*, *Science* **1999**, 286, 1127.
- (4) P. Chen, Z. Xiong, J. Luo, J. Lin, and K.L. Tan, *Nature* (London), **2002**, 420, 302.
- (5) Lee, H. *et al.*, *Nature* **2005**, 434, 743.

- (6) Haiduc, A. G.; Stil, H. A.; Schwarz, M. A.; Paulus, P.; Geerlings, J. J. C. *J. Alloys Compd.* **2005**, **393**, 252; Jensen, C. M. and Gross K. J. *Appl. Phys. A* **2001**, **72**, 213.
- (7) Carpetis, C.; Peschka, W. *Int. J. Hydrogen Energy* **1980**, **5**, 539; Rzepka, M.; Lamp, P.; de la Casa-Lillo, M. A. *J. Phys. Chem. B* **1998**, **102**, 10894.
- (8) Iijima, S. *Nature* (London) **1991**, **354**, 56.
- (9) Ajima, K.; Yudasaka, M.; Suenaga, K.; Kasuya, D.; Azami, T.; and Iijima, S. *Advanced Materials* **2004**, **16**, 397.
- (10) Bandow, S., et al. *Chem. Phys. Lett.* **2000**, **321**, 514.
- (11) Ye, Y., et al. *Appl. Phys. Lett.* **1999**, **74**, 2307.
- (12) Okamoto, Y.; Miyamoto, Y.; *J. Phys. Chem. B* **2001**, **105**, 3470.
- (13) Jhi, S.-H. and Y.-Kyun Kwon, *Phys. Rev. B* **2005**, **71**, 035408; Murata, K.; Hashimoto, A.; Yudasaka, M.; Kasuya, D.; Kaneko, K.; and Iijima, S. *Advanced Materials* **2004**, **16**, 1520.
- (14) Kubas, G. L.; Ryan, R. R.; Swanson, B. I.; Vergamini, P. J.; Wasserman, H. J. *J. Am. Chem. Soc.* **1984**, **106**, 451.
- (15) Kubas, G.J. *J. Organometallic Chem.* **2001**, **635**, 37.
- (16) Mediat, M.; Tachibana, G. N.; and Jensen, C. M. *Inorg. Chem.* **1992**, **31**, 1827.
- (17) Y. Zhao, Y.-H. Kim, A.C. Dillon, M.J. Heben, and S.B. Zhang, *Phys. Rev. Lett.* **2005**, **94**, 155504.
- (18) Niu, J.; Rao, B.K.; and Jena, P. *Phys. Rev. Lett.* **1992**, **68**, 2277.
- (19) Gagliardi, L. and Pyykkö, P. *J. Am. Chem. Soc.* **2004**, **126**, 15014.
- (20) Gates, B.C. *Chem. Rev.* **1995**, **95**, 511.
- (21) Gladysz, J. A., et al. *J. Am. Chem. Soc.* **1986**, **108**, 7863.
- (22) Hudson, R. D. A. *J. Organometallic Chem.* **2001**, **637–639**, 47.
- (23) Michael, D. and Mingos, P. *J. Organometallic Chem.* **2001**, **635**, 1.
- (24) Crabtree, R.H. *The Organometallic Chemistry of the Transition Metals*; John Wiley & Sons Inc., 1988.
- (25) G. Kresse et al., <http://cms.mpi.univie.ac.at/VASP>
- (26) Perdew J.P. et al. *Phys. Rev. B* **1992**, **46**, 6671.
- (27) Perdew, J.P.; Burke, K.; Ernzerhof, M. *Phys. Rev. Lett.* **1996**, **77**, 3865.
- (28) T. Guo, C.M. Jin, and R.E. Smalley, *J. Phys. Chem.* **95**, 4948 (1991).
- (29) R.-H. Xie et al., *Phys. Rev. Lett.* **90**, 206602 (2003).
- (30) Kohanoff, J.; Andreoni, W.; Parrinelo, M. *Chem. Phys. Lett.* **1992**, **198**, 472.
- (31) Jemmis, E.D.; Manoharan, M.; and Sharma, P. K. *Organometallics* **2000**, **19**, 1879.
- (32) C. Kittel, *Introduction to solid state physics*, 7th ed. (Wiley, New York, 1960).
- (33) Guo, B.C.; Kerns, K.P.; Castleman, A.W., Jr. *Science* **1992**, **255**, 1411-1413.
- (34) Pilgrim, J. S.; Duncan, M. A. *J. Am. Chem. Soc.* **1993**, **115**, 9724.
- (35) A.C. Dillon et al., *Mat. Res. Soc. Proc.* **801**, 167 (2003).
- (36) Bouaricha, S.; Dodelet, J.-P.; Guay, D.; Schutz, R. *J. Alloys Compd.* **1999**, **285**, 119.

EXFOLIATED GRAPHITE NANOFIBERS FOR HYDROGEN STORAGE

Angela D. Lueking, Ling Pan, Deepa Narayanan,
Caroline E.B. Clifford

The Pennsylvania State University
University Park, PA 16802

Abstract

Exfoliation of graphite nanofibers (GNF) expands the interplanar spacing of the GNF which leads to increased hydrogen storage. The exfoliation technique plays a large role in the resulting GNF microstructure, surface area, and hydrogen storage properties. Variations in preparation conditions expand the GNF lattice from 3.4 Å to over 500 Å. The BET surface area of the exfoliated GNF increases as much as 10-fold to 555 m²/g. Increased surface area correlates with low temperature physisorption of hydrogen at 77K with an observed uptake of 1.2% at 77K and 20 bar. Conversely, observed dislocations in the graphitic structure correlate with a fourteen-fold increased ambient temperature adsorption at 20 bar. These results suggest that selective exfoliation of a nanocarbon is a means by which to control the relative binding energy of the hydrogen interaction with the carbon structure and thus vary the operative adsorption temperature.

Introduction

Despite early hydrogen storage claims in carbon materials that were largely irreproducible, reports continue to emerge showing hydrogen uptake ranging from 3-17%. An explanation emerging from these reports is that post-synthesis treatments modify the carbon structure and enhance hydrogen adsorption. Nuclear diffraction has shown that hydrogen may become chemically bound to graphitic carbon during certain preparations [1], terminal carbons have been suggested to act as catalytic entities to dissociate hydrogen [2], and electron micrographs have suggested that simple exposure to hydrogen may expand the graphite lattice of certain carbon nanostructures [3].

In an effort to test the emerging hypothesis that defects, dislocations, and/or terminal carbons lead to increased hydrogen storage via hydrogen intercalation into the graphite lattice, we have worked to develop methods that expand the graphite lattice a priori in nano-carbonaceous materials. Unlike exfoliation of single-wall nanotubes, intended to separate bundles into individual tubes, our exfoliation method targets intra-particle spacings. Our method is derived from well-established techniques to exfoliate graphite, in which intercalation of graphite is followed by a thermal shock to expand the graphitic layers.

Herringbone GNF provide an interesting candidate for carbon exfoliation, with their slit-pore geometry, nano-scale dimensions, high aspect ratio, and graphitic layers that terminate along the fiber axis. Herringbone graphite nanofibers (GNF) provide an interesting candidate for carbon exfoliation, with their slit-pore geometry, nano-scale dimensions, high aspect ratio, and graphitic layers that terminate along the fiber axis. It was previously thought that the high aspect ratio and nanoscale dimensions of the GNF would preclude exfoliation. However, our preliminary data shows that we have successfully exfoliated herringbone GNF, with a resulting nanoscale structure that is previously unreported.

Experimental

Highly ordered, herring-bone graphite nanofibers were purchased from Catalytic Materials, Ltd; with a metal content of less than 1% as reported by the manufacturer; these GNF had a low

baseline hydrogen uptake and were not activated prior to us. Based on preliminary studies with graphite exfoliation, the primary exfoliation method used in this study was a 50/50 mixture of nitric and sulfuric acids followed by thermal shocking at 700 °C (EGNF-700). A portion of this sample was subjected to an additional high temperature treatment by heating the sample under flowing Argon at 1000 °C for 36 hours (EGNF-1000).

Characterization. Materials were characterized using standard BET methods with nitrogen at 77K (Quantachrome Autosorb I) and helium densitometry measurements (Hiden IGA-003). Scanning electron microscopy (SEM) (Philips XL20) and TEM (JEOL 2010 and JEOL 2010F) were used to characterize the microstructure of the material. Total ash content was determined by temperature programmed oxidation on a low-pressure Perkin Elmer Thermogravimetric analyzer 7 (TGA).

Hydrogen Uptake. A high-pressure thermo-gravimetric analyzer (Hiden Isochema IGA-003) was used to evaluate hydrogen uptake at pressures up to 20 bar. The IGA provided a highly sensitive (+1 µg) measurement with precise temperature and pressure control for automated measurements of adsorption and desorption isotherms. All samples were subjected to an in situ degas at 150 °C, unless otherwise stated. Hydrogen uptake measurements were normalized to sample mass after pretreatment, with buoyancy corrections determined from density measurements with helium. With a typical sample size of 50 mg, the error in the hydrogen due to instrumental limitations is +0.02 wt% absolute. Select samples were chosen for quality checks to ensure the reproducibility of the measurements.

Results and Discussion

The exfoliated GNF retains the overall nanosized dimensions of the original GNF, with the exfoliation temperature determining the degree of induced defects, lattice expansion, and resulting microstructure. Transmission electron microscopy (TEM) confirmed the herringbone structure of the lattice spacing and a 3.4 Å lattice spacing (Figure 1). The EGNF-700 fibers had dislocations in the graphitic structure and a 4% increase in graphitic lattice spacing to 3.5 Å (Figure 2). The EGNF-1000 fibers were significantly expanded along the fiber axis, with regular intervals of graphitic and amorphous regions ranging from 0.5 to >50 nm in width (Figure 3). The surface area of the starting material was increased from 47 m²/g to 67 m²/g for EGNF-700 and to 555 m²/g for the EGNF-1000 (Table 1).

Table 1. Characterization of GNF before and after Exfoliation

	GNF	EGNF-700	EGNF-1000
Treatment	None	Acid intercalation; 700 °C 2 minutes	+ 1000 °C for 36 hours in Argon
BET Surface Area (m ² /g)	47	67	555
Helium Density (g/cm ³)	1.38	1.04	1.36
H ₂ Uptake (77K, 20 bar)	0.34%	0.39%	0.39%
H ₂ Uptake (300K, 20 bar)	0.02%	0.29%	0.03%
Ash Content (wt%)	1.5%	*	1.1%

*in progress

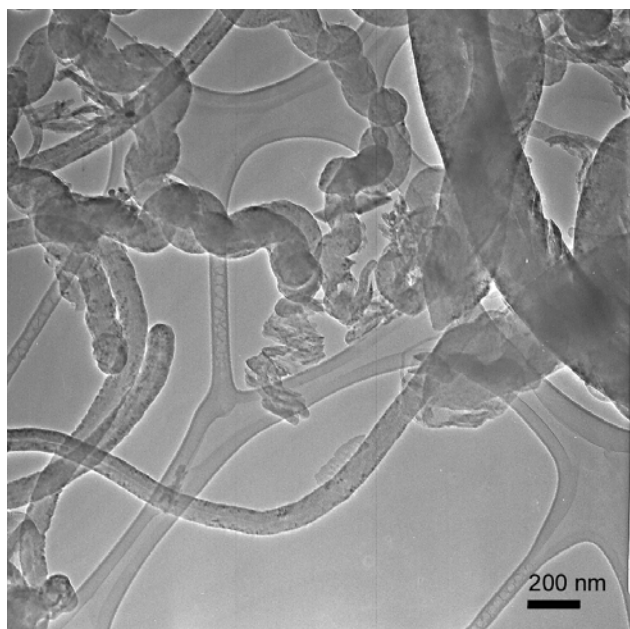


Figure 1. Transmission electron micrographs of untreated GNF.

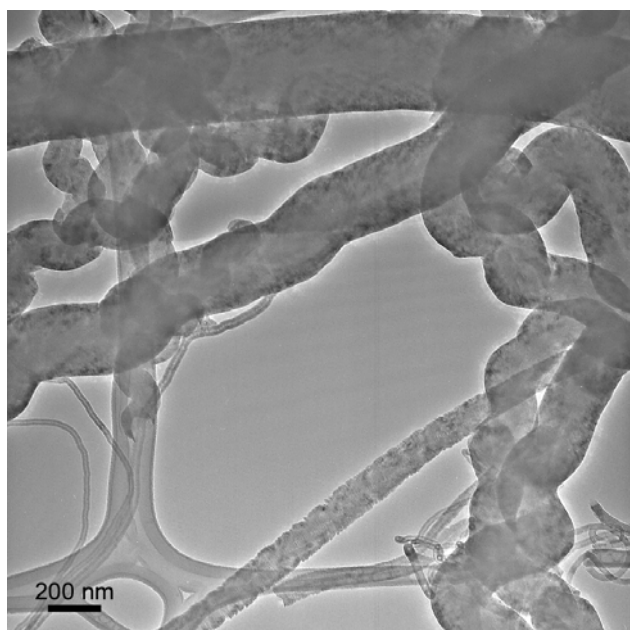


Figure 2. Transmission electron micrographs of exfoliated GNF after a 700 °C thermal treatment (EGNF-700)

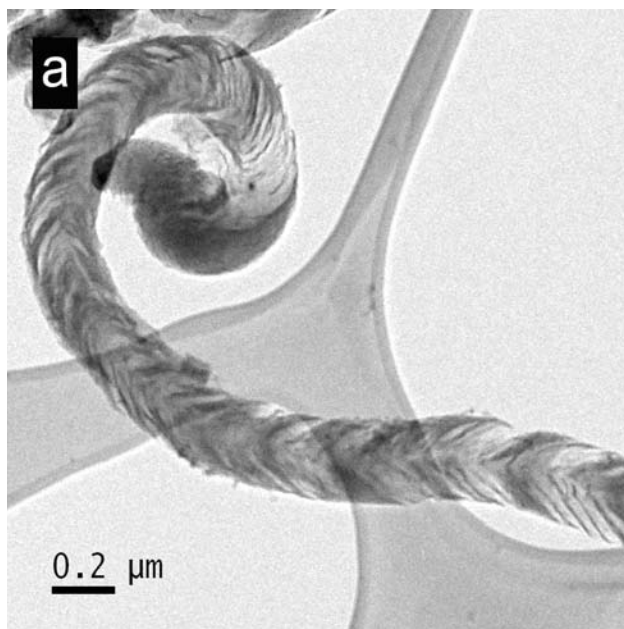


Figure 3. Transmission electron micrographs of exfoliated GNF after an extended 1000 ° thermal treatment.

Hydrogen uptake measurements at 20 bar indicate that the overall hydrogen uptake and operative adsorption temperature are sensitive to the structural variations and graphitic spacing. The increased surface area of the ENGF-1000 led to a 1.2% hydrogen uptake at 77K and 20 bar, a three-fold increase in hydrogen physisorption of the starting material (Figure 4). The uptake of the 700 °C treated material had a 0.29% uptake at 300K and 20 bar (figure 5); although low, this was a fourteen-fold uptake over the starting material and higher than other commonly used pretreatment methods. These results suggest that selective exfoliation of a nanofiber is a means by which to control the relative binding energy of the hydrogen interaction with the carbon structure and thus vary the operative adsorption temperature.

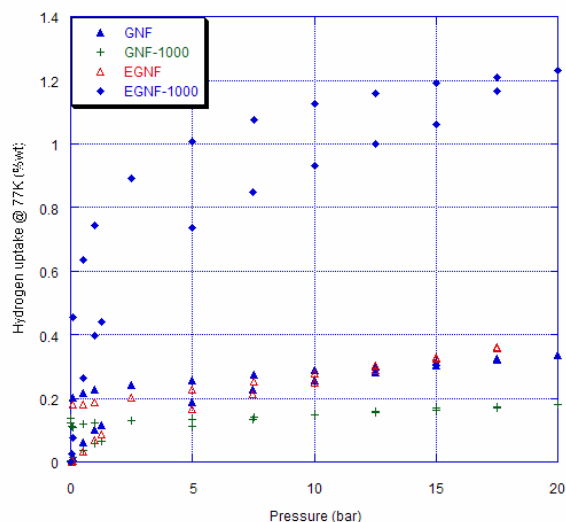


Figure 4. Hydrogen Isotherms for various fibers at 77K.

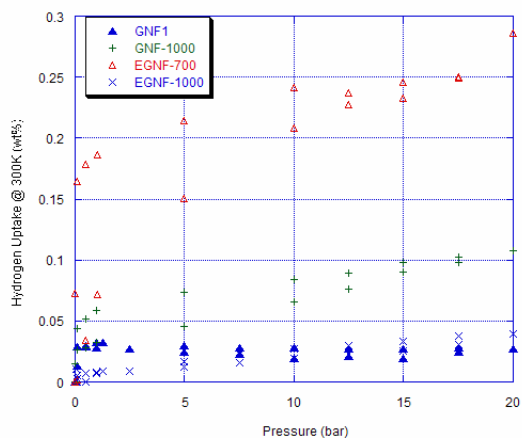


Figure 5. Hydrogen Isotherms for various fibers at 300K.

The overall hydrogen uptake for the EGNF-700 and EGNF-1000 is not close to the DOE hydrogen storage targets. We are, however, encouraged by the data that suggests that exfoliation is a means by which to control the carbon-hydrogen binding energy. At 77K, the hydrogen uptake for EGNF-1000 is comparable to recent reports of 2.7 wt% uptake in a spherical nanoporous carbon with surface areas between 946 and 1646 m²/g at 77K and 50 bar[4] and 2 wt% for commercially available activated carbon fibers at 77K and 20 bar.[5]

Conclusions

A new exfoliated carbon fiber with nanodimensions was synthesized by graphite exfoliation followed by high temperature treatment. The exfoliated carbon nanofiber had a unique microstructure, with repeating units of high-density graphitic regions separated by low density regions that were amorphous in nature. An expansion along the fiber axis was accompanied by a ten-fold increase in BET surface area. At the other end of the preparation spectrum, GNF were prepared with mild dislocations within the graphitic structure and a 4% increased latticed spacing. Overall hydrogen uptake and operative adsorption temperature was drastically different for these two exfoliated materials, suggesting a means by which to control the carbon-hydrogen binding energy through variation of exfoliation conditions. Future work will include systematic variations on exfoliation conditions in an attempt to synthesize materials with an array of slit pore dimensions, and include subsequent chemical treatments to control the resulting surface chemistry on the exfoliated carbon structures.

Acknowledgement. The authors would like to thank E. Dickey for her feedback on the TEM presented in this work. This work was funded through start-up funds proved by PSU's Institute for the Environment, The Energy Institute, and the College of Earth & Mineral Sciences. Funding for exfoliation of carbon for hydrogen storage was provided, in part, by the H2E Center at Penn State University.

References

- (1) Fukunaga, T., K. Itoh, S. Orimo, M. Aoki, and H. Fujii. *Journal of Alloys and Compounds*, **2001**, 327, 224.
- (2) Browning, D.J., M.L. Gerrard, J.B. Lakeman, I.M. Mellor, R.J. Mortimer, and M.C. Turpin. *Nano Letters*, **2002**, 2, 201.
- (3) Gupta, B.K. and O.N. Srivastava. *International Journal of Hydrogen Energy*, **2001**, 26, 857.

- (4) Terres, E.; Panella, B.; Hayashi, T.; Kim, Y. A.; Endo, M.; Dominguez, J. M.; Hirscher, M.; Terrones, H.; Terrones, M. *Chem Phys Lett* **2005**, 403, 363.
- (5) Kadono, K.; Kajiura, H.; Shiraishi, M. *Appl Phys Lett* **2003**, 83, 3392.

INELASTIC NEUTRON SCATTERING OF H₂ ADSORBED ON ACTIVATED CARBON

D.G. Narehood^a, H. Goto^b, P.E. Sokol^c, and P.C. Eklund^a

^a Department of Physics and Materials Research Institute Penn State University, University Park, PA 16802 USA

^b Honda Fundamental Research Laboratories, Tokyo, Japan

^c Indiana University Cyclotron Facility
Indiana University
Bloomington IN 47408, USA

Introduction

The properties of H₂ adsorbed in porous media and on surfaces are of interest for both applied and fundamental reasons. With the strong interest in moving from Petroleum to a Hydrogen economy, a determination of an adequate fuel storage device is essential. The microscopic properties of the adsorbed H₂ will undoubtedly play a role in this determination. On the fundamental side, adsorption of H₂ on surfaces is of interest due to the unique properties of the molecules. For instance, the overall symmetry requirements of H₂ restrict even rotational states to have a combined nuclear spin of 0 (para-H₂) while odd rotational states are restricted to have a combined nuclear spin of 1 (ortho-H₂). In addition, due to the light mass of the molecule, its zero-point motion dominates the molecules momentum distribution.

Properties of the molecule such as the rotational behavior, ortho-to-para conversion, and momentum distribution are sensitive to the molecule's local environment. We have used inelastic neutron scattering (INS) to investigate these properties for H₂ adsorbed on an Activated Carbon (AC) for various fillings.

Experimental

AC Sample. In these studies, 2 g of a commercially available AC sample was utilized. The surface area of the sample was determined to be 1600 m²/g from an N₂ adsorption isotherm taken at 77K. Prior to utilization of the sample in the INS measurements, the sample was baked at a temperature of 1000K under vacuum ($P \leq 10^{-6}$ torr) for ~24 hrs. This process was performed to remove strongly physisorbed impurities such as H₂O and CO₂ from the AC sample. After this treatment, the sample was stored in an inert helium atmosphere.

INS Measurements. The inelastic neutron scattering measurements were performed on the MARI time-of-flight (TOF) chopper spectrometer at the ISIS spallation source at the Rutherford Appleton Laboratory (Didcot, UK). Due to the low-resolution requirements and the desire to optimize intensity, the spectrometer was equipped with their "sloppy" chopper. This chopper was phased to select incident neutron energies of 50 meV, for the rotational and conversion studies, and 750 meV, for the deep inelastic neutron scattering measurements (DINS). TOF data were collected by neutron detectors covering a scattering angle of 3 to 135° as well as by the monitors, located in front of and behind the sample cell. Analysis of the monitor data allows a determination of the incident neutron energy and the time at which the neutrons are scattered from the sample.

For the INS measurements, the AC sample was placed in a sample cell with an annular geometry. This cell was then attached to the cold finger of closed cycle refrigerator and cooled to 20K where the sample was filled with n-H₂ (75% ortho-H₂, 25% para-H₂). A standard gas handling system allowed precise control of the amount

of H₂ introduced to the sample. Both rotational and DINS spectra were collected for fillings ranging from ~0.38 filling to a full pore filling with the temperature held fixed at 20K. Temperatures were measured with a commercial Silicon diode thermometer placed at the top of the cell.

In addition to the INS spectra collected with the AC sample loaded with H₂, spectra were also collected with the just the sample cell and AC sample. These background spectra were subtracted from spectra collected with H₂, with an attenuation correction factor applied, to provide spectra consisting of scattering solely from H₂.

Results and Discussion

The INS spectra collected from neutrons with an incident energy of 50 meV have been utilized to probe the effect of the interaction of H₂ with the AC surface on the rotational states of the adsorbed molecules. The rotational energy levels for a free rotor are given by $E_{rot} = J(J+1)B$, where J is the rotational quantum number and B is the rotational constant, which for molecular hydrogen is 7.35 meV¹. Each of these levels possesses a degeneracy of $2J+1$. An energy level diagram with the rotational ground state and the first excited state is shown on the left in **Figure 1**. Indicated in the diagram are the neutron induced rotational transitions that can be observed in an INS spectrum. The transition between the $J=0$ and $J=1$ states requires both a change in rotational quantum number as well as a change in the combined nuclear spin of the molecule as a result of the overall symmetry requirements of the molecules wave-function. Introduction of an orientationally dependent potential in the Hamiltonian of H₂ can result in a splitting of the degenerate rotational states and a corresponding change in the energies of these states. Such behavior has been observed for H₂ adsorbed on the pore walls in both xerogel² and zeolite³.

A background subtracted INS spectrum with the rotational energy level transitions for H₂ on AC for the full pore filling is shown on the right in **Figure 1**. Clearly present in the spectrum collected after initial H₂ loading is an elastic peak, a peak at -14.7 meV, and a peak at 14.7 meV. The elastic peak is attributed to transitions between sublevels of the $J=1$ state, while the peaks at -14.7 meV and 14.7 meV are attributed to the $J=1 \rightarrow 0$ and $J=0 \rightarrow 1$ transitions, respectively, as indicated in the diagram. These transitions occur at their free-rotor values, allowing use to conclude that the rotational states are not altered and consequently, that the H₂-AC interaction does not possess an orientational dependence. At all fillings studied, the same rotational behavior is exhibited. This indicates, as expected, that the H₂-H₂ interactions does not produce an effect on the molecules rotational behavior.

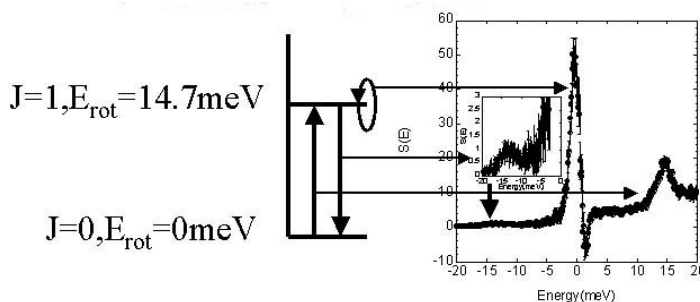


Figure 1. Rotational energy level diagram for H₂ (left) acting as a free rotor and a rotational spectrum collected from a full pore of H₂ adsorbed on AC shortly after H₂ loading (right).

After ~6 h after H₂ loading, only the peak at 14.7 meV remains in the spectra, which is a clear indication that all molecules in the

ortho-state have converted to the para-state. Because the intensity of the peak at 14.7 meV is directly proportional to the concentration of para-molecules in the system, the details of this ortho-to-para conversion process have been studied by following the time-dependence of the peak at 14.7 meV as shown in **Figure 3** for a full pore H_2 filling.

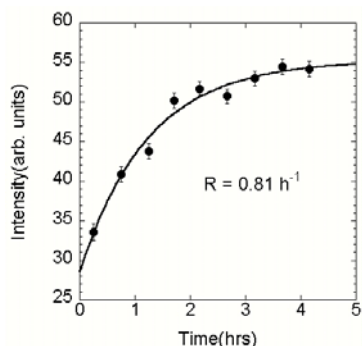


Figure 2. Time-dependent intensity of the peak at 14.7 meV for the rotational spectra collected from a full pore filling of H_2 on AC.

We have found that the data in **Figure 2** is best fit with an exponential of the form

$$c_{\text{para}}(t) = 1 - c_{\text{ortho}}(0)e^{-Rt}$$

where $c_{\text{para}}(t)$ is the time-dependent para concentration, $c_{\text{ortho}}(0)$ is the initial ortho-concentration, and R is the rate constant. For the conversion data shown in **Figure 2** $R = 0.81 \pm 0.11 \text{ h}^{-1}$. The exponential form of the conversion, as well as the conversion rate, are independent of H_2 filling. The exponential conversion of the molecules as well as the independence of the conversion rate on H_2 filling indicate that the conversion is caused predominately by the interaction of the adsorbed molecules with the AC. This is in contrast to the bi-molecular conversion process observed for the bulk solid H_2 ¹ and H_2 adsorbed in the pores of zeolite³. The bi-molecular nature of the conversion process in these instances, indicates that it is the interaction of the H_2 molecules with each other that is responsible for the conversion.

The conversion we observe for H_2 adsorbed on AC is very much faster than observed in the previously mentioned systems. While it is difficult to make a direct comparison due to the different nature of the conversion processes, we can compare the times at which the original ortho-concentration is reduced by a factor of 2. The half-lives in the bulk solid H_2 ($K = 1.8\%/h$, K = rate constant) and H_2 adsorbed on the pore wall of zeolite ($K = 8.5\%/h$) are ~ 70 h and ~ 19 h, respectively, in comparison to the half-life of ~ 1 hr for H_2 adsorbed on AC. Conversion of the molecules adsorbed on the AC sample is greatly enhanced over the bulk and H_2 adsorbed in the pore wall of zeolite.

The DINS spectra collected from neutrons with incident energies of 750 meV have been used to study the momentum distribution of H_2 adsorbed on AC. Using the impulse approximation⁵, mean kinetic energies ($\langle KE \rangle$) have been extracted for the adsorbed molecules for each filling from the widths of scattering peaks appearing in DINS spectra such as the one shown in **Figure 3a**. The extracted $\langle KE \rangle$ for each filling are shown in **Figure 3b**. Included for comparison in the plot of $\langle KE \rangle$ vs. filling are values extracted for the $\langle KE \rangle$ of H_2 adsorbed on graphite in both the commensurate phase (solid line) and incommensurate phase (long dashes) as well as the estimate for contribution of the H_2 -C interaction to the molecules $\langle KE \rangle$ (short dashes)³. Although we do not have $\langle KE \rangle$'s for fillings lower than ~ 0.38 due to the correspondingly low scattering intensity, we expect the contribution of the H_2 -C interaction to $\langle KE \rangle$ (~ 55 -57 K) to provide a lower limit

for $\langle KE \rangle$ in our system as the filling approaches zero. It is probable that the $\langle KE \rangle$ in the low filling regime is greater than this estimate due to the curvature of the AC surface which will enhance the localization of the adsorbed molecules with respect to the case of H_2 on planar graphite.

Obvious in **Figure 3b** is the strong dependence of the $\langle KE \rangle$ on filling. The observed increase in $\langle KE \rangle$ to a filling of ~ 0.75 results from the strong contribution the molecules zero-point motion has on the mean kinetic energies. As the filling is increased, the localization of the molecules is increased, which results in a corresponding increase in $\langle KE \rangle$. The $\langle KE \rangle$ of the H_2 on AC at this filling is comparable to that of H_2 on planar graphite in the commensurate phase, indicating that the localization of the molecules in each case is comparable. At full pore filling, the $\langle KE \rangle$ does not approach the value extracted for the incommensurate phase of H_2 on planar graphite. Instead the $\langle KE \rangle$ is within error of the measured $\langle KE \rangle$ at the 0.75 filling. This lack of increase in $\langle KE \rangle$ is understood by the H_2 entering the micropores of the AC sample and not contributing to the compression of molecules adsorbed on the AC surface.

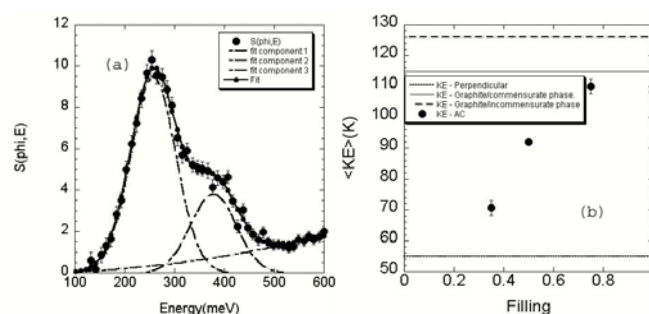


Figure 3. (a) A DINS spectrum collected from the full pore filling of H_2 on AC. (b) $\langle KE \rangle$ as a function of H_2 filling. Also shown for comparison are the $\langle KE \rangle$ for H_2 on graphite in the commensurate (solid line) and incommensurate phase (dashed line) as well as the contribution to the $\langle KE \rangle$ for H_2 on graphite from the H_2 -C interaction.

Conclusions

We have studied the microscopic properties of H_2 adsorbed on AC as a function of H_2 filling. The adsorbed molecules exhibit free-rotor behavior at all fillings, indicating that a lack of orientational dependence in the H_2 -AC interaction. The ortho-to-para conversion of the adsorbed molecules is also independent of filling and is well described by an exponential model. This conversion is much faster than exhibited in the bulk solid as well as for H_2 adsorbed in other porous media such as zeolite. The $\langle KE \rangle$ exhibits a strong dependence on filling, increasing as the filling is increased, except at the full pore filling. This lack of increase in $\langle KE \rangle$ results from H_2 entering the pores of the sample and not causing further localization of molecules adsorbed on the surface.

Acknowledgement. This work was supported by the Department of Energy under Grant DE-FC36-05GO15077 and by Honda Research and Development.

References

- (1) Silvera, I.F.; *Rev. Mod. Phys.* **1980**, 52, 393.
- (2) Narehood, D.G.; Grube, N.; Dimeo, R.M.; Brown, D.W.; Sokol, P.E.; *J. Low Temp. Phys.* **2003**, 132, 223.
- (3) Brown, D.W.; Sokol, P.E.; Fitzgerald, S.A.; *Phys. Rev. B.* **1999**, 59, 13258.
- (4) Kellog, G.J.; Sokol, P.E.; Sinha, S.K.; Price, D.L.; *Phys. Rev. B.* **1990**, 42, 7725.
- (5) Hohenberg, P.C.; Platzman, P.M.; *Phys. Rev.* **1966**, 152, 198.

LOW TEMPERATURE CARBON DIOXIDE ACTIVATION OF MULTI-WALLED CARBON NANOTUBES FOR HYDROGEN STORAGE

John M. Andresen¹, James M. Blackman¹, Colin E. Snape¹, John W. Patrick¹ and Colin Jennis-McGroarty²

¹ School of Chemical, Environmental and Mining Engineering,
University of Nottingham, University Park, NG7 2RD, UK

²The Energy Institute, The Pennsylvania State University, University
Park, PA 16802, USA

Introduction

A major issue for the use of hydrogen as a transportation fuel is its safe storage on-board vehicles. Carbon materials, such as carbon nanotubes, have been touted as a candidate for hydrogen storage at ambient temperatures and modest pressures, although some scattered results have been obtained (1-3). One promising candidate has been single-walled carbon nanotubes (SWNTs) where bundles of SWNT have been reported to adsorb 5-10 wt% of H₂ probably due to the interaction of hydrogen molecules with ropes of single-walled carbon nanotubes rather than storage of hydrogen within the tubes (4, 5). A less expensive alternative to SWNTs are multi-walled carbon nanotubes (MWNTs) and some studies have indicated that MWNT can be used for hydrogen storage (6, 7). One of the main issues is the accessibility of the hydrogen to the graphite like structures of the MWNTs due to the outer layer preventing the gas from entering the system. Making pathways available for the H₂ to pass through the structure, e.g. by activation of the MWNTs, could significantly enhance the hydrogen storage capacity of MWNTs and thus form a low cost alternative to SWNTs. This study focuses on low temperature carbon dioxide activation of multi-walled carbon nanotubes for hydrogen storage.

Experimental

The multi-walled nanotube sample was obtained from Nanostructured & Amorphous Materials, Inc. The activation was conducted at 550°C under a flow of carbon dioxide up to 32 hours. The hydrogen adsorption measurements were made on a custom built volumetric differential pressure apparatus (8)

Results and Discussion

Changes of surface area of multi-walled carbon nanotubes activated in carbon dioxide at 550°C has been reported earlier (9). Typically, the surface area will start increasing after a couple of hours of activation, peak after a certain time and then decrease. In this study a MWNT sample activated for 4 hours was tested for its hydrogen storage capacity at different pressures and the uptake curves are shown in Figure 1. The uptake increases from 0.3 wt% at 20 bar to over 1.6 wt% at 100 bar. All the uptake curves have an initial rapid uptake of about 0.1 wt% similar to the behavior of activated carbons and correlate well with the relative low surface area. The main hydrogen uptake takes place over the next 3-4 hours indicating a very slow diffusion of the hydrogen into the carbon structures. This process suggests that the activation process has made the interior structure of the MWNT accessible for the hydrogen. Scheme 1 shows a schematic of representation of low temperature carbon dioxide activation of MWNT. It is postulated that the CO₂ will start reacting with the MWNT walls and transfer the ordered carbon into gaseous species or amorphous carbon. As the activation time is increased the interior structure of the MWNT may become exposed and this could explain the increase in the hydrogen storage capacity of the activated sample.

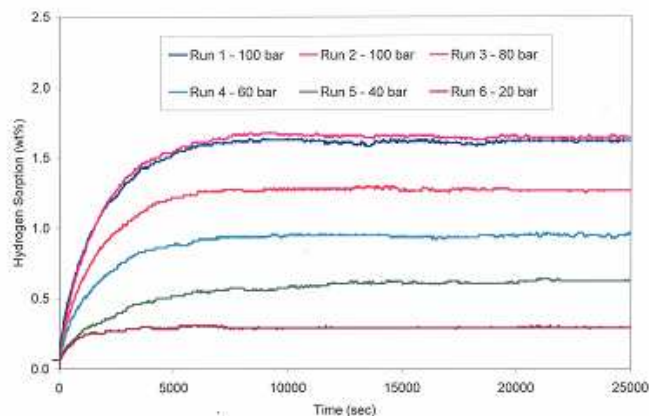
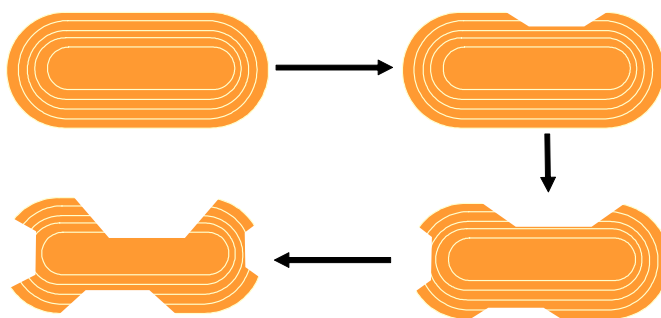


Figure 1. Hydrogen storage capacity at room temperature under different pressures for a MWNT activated at 550°C for 4 hours in carbon dioxide.



Scheme 1. Schematic of representation of low temperature carbon dioxide activation of MWNT.

Conclusions

It was found that the hydrogen storage capacity of the multi-walled nanotubes (MWNT) at room temperature was greatly enhanced by low temperature activation in carbon dioxide at 550°C. Hydrogen storage of the degassed samples showed an uptake of up to 1.6 wt% for the activated nanotube at 100 bar compared to 0.9 wt% for the non-activated sample.

References

- (1) Dillon, A.C., Heben, M.J., *Applied Physics A-Materials Science & Processing*, 72 (2), 133-142, 2001
- (2) Rodriguez-Reinoso, F., Linares-Solano, A., *Chemistry and Physics of Carbon*, Ed. Thrower, P.A., Marcel Dekker, Inc., New York, Vol. 22, 1, 1989.
- (3) Hirscher, M., Becher, M., Haluska, M., Quintel, A., Skakalova, V., Choi, Y.M., Dettlaff-Weglikowska, U., Roth, S., Stepanek, I., Bernier, P., Leonhardt, A., Fink, J., *J. Alloys and Compounds*, 330, 654-658, 2002.
- (4) Pradhan, B.K., Sumanasekera, G.U., Adu, K.W., Romero, H.E., Williams, K.A., Eklund, P.C., *Physica B-Condensed Matter*, 323 (1-4), 115-121, 2002
- (5) Gennett, T., Dillon, A.C., Alleman, J.L., Jones, K.M., Hasoon, F.S., Heben, M.J., *Chemistry of Materials*, 12 (3), 599, 2000
- (6) Chambers, A., Park, C., Baker, R.T.K., Rodriguez, N.M., *J. Physical Chemistry B*, 102 (22), 4253-4256, 1998
- (7) Lueking, A., Yang, R.T., *AIChE*, 49 (6), 1556-1568, 2003
- (8) Blackman J.M., Patrick, J.W., Snape, C.E., *Prepr. Pap.-Am. Chem. Soc., Div. Fuel Chem.* 2004, 49 (1), 207-209
- (9) Andresen, J.M., Chastain, E.K., *Prepr. Pap.-Am. Chem. Soc., Div. Fuel Chem.* 2004, 49(2), 688-689

NEW ELECTROLYTIC SYNTHESIS OF BOROHYDRIDE ANIONS FROM BORON OXIDE IN A MOLTEN SALT MELT

Michael T. Kelly, Jeffrey V. Ortega, Todd J. Randall, and Ying Wu

Millennium Cell Inc.
1 Industrial Way West
Eatontown, NJ 07724

Introduction

Efficient storage of hydrogen remains a primary problem to be solved before the gas can be considered for any mass commercial applications. Traditional methods for storage are to compress or to liquefy the gas, or to employ a solid-state medium that absorbs hydrogen. The difficulties here are well understood and not easily addressed: Compressed methods are not volumetrically efficient, and solid-state methods are not gravimetrically efficient.

An area of growing interest in the field is the use of chemical hydrides. Chemical hydrides based on boron occupy an energy density middle ground, being more volumetrically appealing than compressed methods and more gravimetrically acceptable than solid-state storage. For this reason, boron based hydrogen storage has a greater likelihood of being adequate on both counts.

The main barrier to using chemical hydrides for hydrogen storage is an economic one. Synthesized by current methods they are too expensive to be considered a primary power source. There is a need, therefore, to identify new synthesis methods for boron hydrides. Herein we examine an electrolytic reduction leading to the formation of borohydride, starting from boron oxide and hydrogen gas.

Experimental

All chemicals were obtained from Aldrich Chemicals and used as received without further purification. The alkali bromide melt composition is 56.1 mol % lithium bromide, 18.9 mol-% potassium bromide and 25.0 mol % cesium bromide¹. This eutectic melts at 226 °C. Electrochemistry was carried out at 300 °C in the melt, with hydrogen gas bubbling through the melt. A nitrogen gas jacket was maintained over the catholyte portion of the melt. The anolyte was open to atmosphere, with flowing N₂.

Electrochemistry was carried out with a Parr Instruments VMP model 4-channel potentiostat, in a two-electrode configuration. Typical cell potentials were 5 V. The cathode was a nickel frit (5 µm average pore size) obtained from Mott Corporation, with H₂ bubbling through it. The anode was a piece of Pt gauze. The electrolytic cell had two compartments separated by a glass frit of porosity "C" (25-50 µm).

The titrations for quantifying borohydride used the iodate method². Briefly, a solution containing an unknown amount of borohydride is treated with an excess of potassium iodate (KIO₃). After adding potassium iodide (KI), the remaining iodate solution is acidified with sulfuric acid, and forms the triiodide anion (I₃⁻). The triiodide is titrated with sodium thiosulfate (Na₂S₂O₃). This titration is self-indicating, as the deeply colored triiodide is converted to colorless iodide (I⁻). The difference between the amount of iodate titrated and the measured amount added to the borohydride solution allows calculation of the amount of borohydride in the original solution. The titration appears to be unaffected by the presence of metaborate anions (BO₂⁻), boric acid (B(OH)₃), or high concentrations of alkali bromides.

The presence of borohydride in solution was also verified by ¹¹B-NMR spectroscopy. Borohydride anions give a characteristic quintet, due to the boron signal being split four times by equivalent

protons. The chemical shift for borohydride is 38.7 ppm, with a spin-spin splitting of 0.82 ppm³. The chemical shift for triborohydride is 28.4 ppm, with a spin-spin splitting of 0.32 ppm³.

Results

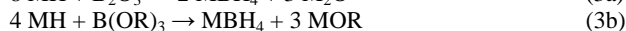
The approach taken to making borohydride anions is based on a series of thermodynamically favorable reactions. Alkali metals are synthesized electrolytically, as in the cathodic equation (1).



Further, it is known that alkali metal will react with hydrogen gas to make the alkali metal hydride, according to equation (2).



Next, alkali metal hydrides are known to react with boron oxide (B₂O₃) or trialkyl borate (B(OR)₃) to yield borohydrides⁴, as shown in equations (3a) and (3b).



Given these three reactions, it follows that borohydride generation may occur through an electrochemical-chemical-chemical (ECC) mechanism.

Supplying voltage to an electrochemical cell containing molten lithium-potassium-cesium bromide eutectic will result in electrochemical synthesis of lithium metal and bromine gas. Potassium and cesium are also potential products but both of the heavier alkali metals are expected by thermodynamics to react with lithium bromide to yield lithium metal and the relevant bromide. For simplicity, lithium will be considered the sole product of electrolysis. If hydrogen is present in the cell the metal will react further to yield lithium hydride, which in turn generates borohydride from B₂O₃.

The initial experiment was designed to test whether molten salts were in fact adequate reaction media for equation (3a). Stoichiometric amounts of lithium hydride and B₂O₃ were added to an alkali bromide melt with stirring. After 15 minutes, the melt was allowed to cool to room temperature. The solid, in its entirety, was dissolved in aqueous 0.5 M NaOH solution. A portion of the solution was submitted to quantitative titration to determine the amount of borohydride present. Reaction yield was 66%, based on the amount of LiH added to the melt. The conclusion is that LiH reacts quickly with B₂O₃ in good yield, and the electrochemical experimentation should proceed.

The idea of the electrochemistry is to generate the LiH *in situ*, and allow the known borohydride generation reaction to proceed as demonstrated. The cathode for the electrochemical process was a nickel frit, with hydrogen gas passing through it. Passing the hydrogen through the cathode is done to promote the reaction between the lithium metal being generated at the cathode and the gas to make the hydride. The anode is platinum mesh. Conveniently, the anode product bromine is highly colored and the gas readily visible above the anode compartment. Bromine is not observed in or above the cathode compartment, suggesting that the cell separator is sufficient to prevent back reaction even though it is not selective.

Figure 1 shows a typical electrolysis at constant voltage, allowed to run overnight (16-24 hours). Cell potential is -5 V vs. the anode. A reasonably high current is achieved throughout the experiment, which was allowed to run overnight. After electrolysis voltage is stopped, the anode and cathode are removed from the cell. The entirety of the melt in the cathode compartment was dissolved in aqueous 0.5 M NaOH. A portion of the solution was submitted for

titration to quantify the presence of borohydride and an aliquot of solution was analyzed by ^{11}B -NMR to verify the presence of borohydride anions. A typical ^{11}B -NMR spectrum of the borohydride in aqueous solution generated by the methods described here is shown in figure 2. The presence of borohydride ions is unmistakable. Both the positioning of the quintet (the boron center split 4 times, once by each equivalent proton) and the splitting are in excellent agreement with both literature values and standards prepared in house.

The best electrolytic conversion measured is 8.3 %, determined by the maximum amount of borohydride that could be made considering the number of electrons that passed through the electrolytic cell, and how much borohydride was actually measured by titration. The latter amount was divided by the former to give yield. Typical experiments gave 4-5 % borohydride.

Close inspection of figure 2 shows that some amount of triborohydride B_3H_8^- was also generated during the experiment. At present, it is postulated that B_3H_8^- is generated when BH_4^- crosses through the separator. When molten lithium borohydride salts are electrolyzed, the oxidation product is diborane B_2H_6 . B_2H_6 will react with BH_4^- to make B_3H_8^- . B_3H_8^- has good aqueous stability and is not destroyed during the dissolution of the melt. The relative concentration of triborohydride to borohydride appeared higher in the ^{11}B -NMR spectrum when the separator cracked during the experiment or was otherwise flawed. The titration methods are not sufficient to determine the relative amounts of triborohydride vs. borohydride. Titration will underestimate the amount of borohydride generated if there is a substantial amount of triborohydride, so yield may be higher than reported.

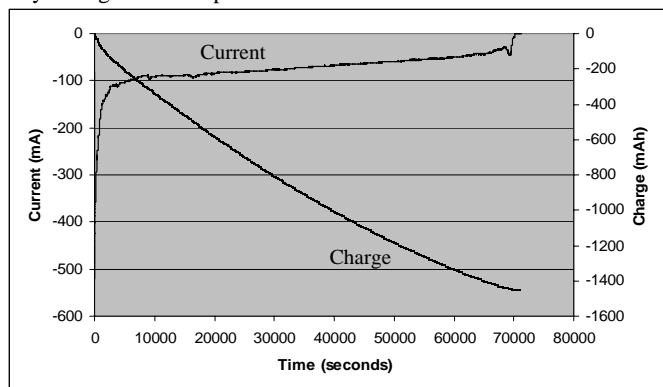


Figure 1. Constant potential electrolysis of alkali bromide an melt containing B_2O_3 to make BH_4^- anions. Cell potential was 5 V

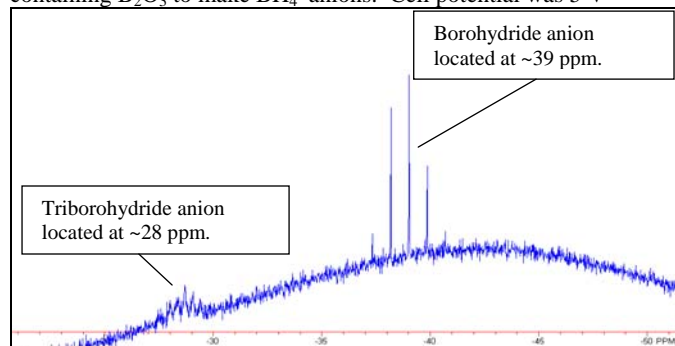


Figure 2. ^{11}B NMR confirming the presence of borohydride anions in solution. Also observed is the B_3H_8^- anion.

Discussion

A practical synthesis must exhibit conversion better than the 8.3 % yield achieved to date. A number of observations indicate, however, that the difficulty is with the first chemical step. The reaction of lithium metal with hydrogen gas to make lithium hydride appears to proceed slowly. Experimentation with added lithium hydride showed that reaction with boron oxide is fast compared with the timescale of the experiment. The prior step, electrochemical generation of the metal takes place at a rate proportional to the current. When the melt is cooled to room temperature but before it is dissolved in aqueous solution, lithium metal appears in the melt and on the cathode. Solid, unreacted boron oxide can also be collected on filtering the aqueous solution. Since the products of the first step and the relevant reagents for the third step are readily found post electrolysis, it is reasonable to conclude that it is the middle step that is the kinetic bottleneck.

Solubility of hydrogen gas is also an issue for the second step. At the operating temperature of 300 °C, the amount of hydrogen dissolved in the melt is low, and therefore may not readily react with lithium. The lithium ends up in large pieces, which will not easily react to form the hydride.

A few other problems affect the reaction. The reaction takes place in a ternary eutectic. The melting point of such a melt is very sensitive to composition. Addition of B_2O_3 makes the melt viscous even 75 °C above the stated melting point. The electrolysis in effect withdraws lithium from the melt, further altering the composition and the melt of ten solidifies near the cathode. The formation of solid often blocks the pores in the cathode through which hydrogen enters the cell. Once blockage occurs, the formation of borohydride stops due to the loss of hydrogen to react with lithium, even if the electrolysis continues.

Fortunately, it appears that these problems are amenable to several solutions. It is unlikely that the methodology for making borohydride is limited to this specific melt. The melt requirements appear to be no more complicated than having anions and cations that are not reduced by strong hydrides. The number of solvent and ionic systems fitting this description is vast, and a change in composition and/or temperature is expected to solve a number of the problems discussed herein, and lead to substantially higher yield. Implementing efficient stirring and different hydrogen entry may also have notable impact.

Conclusion

A new method of making borohydride via electrolysis is described. The transformation employs hydrogen, boron oxide, and electrolytic potential as reagents and takes place in one pot, with no intermediate additions or separations required. The potential for evolving this electrolytic method into a lower cost route to borohydride is high.

Future work must focus on improving the electrolytic yield. Promising pathways involving the similar methods in different solvents or melt systems appear likely to succeed.

Acknowledgement. The gratefully acknowledge support from the Department of Energy, through Cooperative Agreement contract number DE-FC36-04GO14008.

References

- (1) Kasajima, T.; Nishikiori, T.; Nohira, T.; Ito, Y. *Electrochem. and Solid State Lett.*, **2003**, 6 (5), E5.
- (2) Lyttle, D. A.; Jensen, E. H.; and Struck, W. A. *Anal. Chem.*, **1952**, 24 (11), 1843.
- (3) Boron, Metallo-Boron Compounds and Boranes; Adams, R. M., Ed.; John Wiley & Sons: New York, 1964.
- (4) Schlesinger, H. I.; Brown, H. C.; and Finholt, A. E. *J. Am. Chem. Soc.*, **1953**, 75, 205.

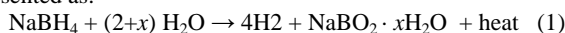
STEAM HYDROLYSIS OF CHEMICAL HYDRIDES: MEETING THE CHALLENGE OF HYDROGEN STORAGE

Michael, A. Matthews, Thomas A. Davis, Josh Gray and Eyma Y.
Marrero-Alfonso

University of South Carolina
Department of Chemical Engineering
301 Main, Swearingen Engineering center
Columbia, SC 29208

Introduction

This paper investigates the steam hydrolysis of chemical hydrides in order to evaluate this technology rigorously for its potential as a means of delivering hydrogen for fuel cells and internal combustion engines. Simple chemical hydrides (e.g. LiH, CaH₂), as well as complex hydrides (NaBH₄, LiBH₄, and others), react with liquid water to produce H₂. For example, NaBH₄ hydrolysis can be represented as:



In equation 1, x is the “excess hydration factor”, representing the fact that the solid byproduct can exist in varying degrees of hydration. In the liquid phase [2] an acid catalyst is required to liberate 100% of the hydrogen, because dissolved NaBH₄ is stabilized by the basic solution formed by the byproducts of the reaction (sodium borate and similar compounds). In reaction (1), the ideal case is where $x = 0$, in which case the mass yield is 10.7 kg H₂ per 100 kg of reactants. In practice, excess water is required so that the NaBH₄ and byproducts remain completely dissolved. Excess water rapidly reduces the mass efficiency of the system.

A recent discovery [1] shows that vaporizing water prior to contact with the hydride can produce hydrogen yields in excess of 90% without the need for a catalyst. Thermodynamic considerations show that, in principle, the heat liberated by the reaction is sufficient to vaporize the stoichiometric water required for the steam. Thus, it may be possible to develop a hydrogen reactor/delivery system that is autothermal at steady state, that produces pure hydrogen in 100% yield, that requires no catalyst, that does not involve strongly caustic solutions, and that uses a minimum amount of water. Furthermore, the solid reaction products should be nearly free of water, which in the long term will facilitate recycling and regeneration to the hydride.

The Department of Energy (DOE) designed the FreedomCAR Technical Targets for hydrogen storage in automobiles; selected targets are given in Table 1. [3] New technologies should meet these targets, such as the gravimetric efficiency (kg H₂/kg reactants) and specific energy (kWh/kg system).

Table 1. FreedomCAR Targets for Specific Energy [3]

Usable specific energy from Hydrogen			
Year	2005	2010	2015
Target (kWh/kg system)	1.5	2	3
Target (kg H ₂ /kg system)	0.045	0.060	0.090

Technologies based on simple and complex chemical hydrides have the potential to meet the targets when ideal hydrolysis is assumed and system considerations are ignored. (Figure 1) One of the challenges is to obtain a gravimetrically efficient system with an acceptable rate of hydrogen delivery and controllable startup dynamics. Efficient water utilization and high rates of reaction are key factors to achieve these targets.

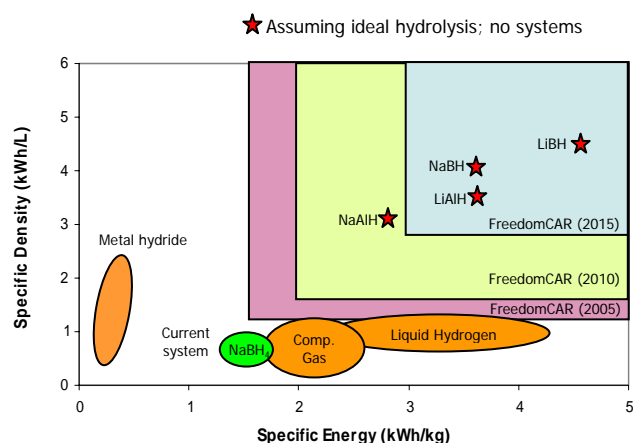


Figure 1. Potential of technologies to meet the FreedomCar targets

Experimental

The NaBH₄ steam hydrolysis reactor system consists of a cylindrical quartz reactor tube placed inside a Thermolyne Model 21100 tube furnace to maintain a constant temperature. One thermocouple placed in the center of the reactor vessel monitors the reaction temperature.

The reaction temperature is affected by the temperature of the incoming steam, which is controlled by a three-stage heater. The first stage of the heater system preheats the steam to approximately 100°C. This preheated liquid/vapor mixture then enters the second and third stages, which superheat the water vapor to the desired reaction temperature. A KD Scientific Model 200 Programmable Syringe Pump is used to pump the desired water flow to the evaporator. The experiments were performed with a water flow rate of 0.1 mL/min (0.0055 mol/min). The volumetric flow rate and cumulative volume of hydrogen are measured as the volume of water displaced from the Erlenmeyer flasks to the graduated cylinder. Condensed water is removed in a cold trap, leaving a stream of hydrogen with a trace amount of water.

The hydride is contained in the fixed bed reactor inside the furnace. All experiments are conducted with one gram of NaBH₄, which is mixed with glass beads or coated on glass beads and then loaded into the reactor between glass-wool plugs. After loading and prior to hydrolysis, the reactor is purged with nitrogen to remove oxygen and moisture and ensure that the reactants are continuously under a blanket of inert gas until the hydrolysis begins. The system is designed so hydrogen can also be co-fed with water at a controlled rate in order to control the partial pressure of steam.

Thermogravimetric analysis (TGA) and differential scanning calorimetry (DSC) are used for analysis of the solid reaction products. PerkinElmer TGA 7 Thermogravimetric Analyzer and DSC 7 Differential Scanning Calorimeter models are used. The temperature program is controlled via a Pyris software program. The temperature program from both the TGA and DSC scans from 25°C to 400°C at a rate of 10°C per minute.

Results and Discussion

Experimental results such as the maximum H₂ generation rate (mol H₂/kgNaBH₄*min) and the % of hydrogen yield are summarized in Table 2. Experiments were performed using NaBH₄ in two different physical forms, either powder or recrystallized as a thin film on glass beads. As shown in Table 2, additives were also used in a few experiments. Temperatures tested were 110°C and 140°C.

Stoichiometric rates for different excess of hydration values (x) are also presented for comparison.

The maximum apparent rate of the reaction, expressed as moles of H_2 produced per minute per kilogram of $NaBH_4$, was determined for each experiment by calculating the maximum slope of the collected hydrogen with respect to time (Table 2). The data show good reproducibility and is in agreement with previous work [1], which yielded a greater rate than the new experiments, but a similar H_2 yield. Hydrogen yields from 82% to 94% of the maximum were obtained without the need of an additive. The use of volatile additives, such as methanol and acetic acid, did not increase the reaction rate, and raising the temperature to $140^\circ C$ decreased the reaction rate and yield. Experimental results from the past work [1] showed that for the different hydrides used, higher yields of hydrogen were obtained at the lowest temperature ($110^\circ C$). An improvement in the rate of reaction is observed when the physical form of $NaBH_4$ is changed from powder to thin films coated on glass beads.

Calculations of the rate of reaction were also performed for idealized situations for $x=0, 4$ and 6 . For example, if no excess water is added ($x=0$) when the water flow rate is 0.1 mL/min (0.0055 mol/min) and the reaction is instantaneous, the theoretical rate of hydrogen production is $11.1 \text{ mol/kg}_{NaBH_4} \cdot \text{min}$, as shown in Table 2.

Table 2. Rates and Yields from Steam Hydrolysis

Exp#	Description	T ($^\circ C$)	Max Slope ($\text{mol/kg}_{NaBH_4} \cdot \text{min}$)	% of Theo. H_2 Yield
1	$NaBH_4$ Powder	110	0.812	88.2
2	$NaBH_4$ Powder	110	0.717	82.7
3	1% acetic acid	110	0.582	101.4
4	1% methanol	110	0.715	92.7
5	$NaBH_4$ Powder	110	0.717	94.0
6	$NaBH_4$ Powder	140	0.349	67.1
7	$NaBH_4$ Powder	140	0.269	40.8
8	6.5% methanol	110	0.545	68.5
9	15% methanol	110	0.589	82.0
Sharp data	$NaBH_4$	110	1.10	87.4
10	$NaBH_4$ Thin films	110	4.01	19.7
11	$NaBH_4$ Thin films	110	4.35	22.9
Theoretical Rates		($x=0$)	11.1	100
		($x=4$)	3.70	100
		($x=6$)	2.78	100

All the experimental rates are lower than the theoretical rates partially because the excess water required to complete the reaction moves the slope to the right, decreasing the reaction rate. Both the initial rates and the yields were lower at $140^\circ C$ than at $110^\circ C$. The lower rates and yields at higher temperatures are counterintuitive, but this is tentatively attributed to mass transfer limitations associated with the particle. Examination of the reactor contents after the experiments revealed that the solid particles were agglomerated. The agglomerated material was soft and wet after the $110^\circ C$ experiment and hard and dry after the $140^\circ C$ experiment. Presumably, the $NaBH_4$ on the surface of the particle reacts first and forms a layer of sodium borate ($NaBO_2$), which grows in thickness as the reaction proceeds. This layer retards steam diffusion through the $NaBH_4$ particle, decreasing the production of hydrogen. The lower reaction rates at higher temperatures would be explained if the dry form of $NaBO_2$ is less permeable to water vapor, which is yet to be proven.

Experiments conducted with thin films show that the reaction rate improved and is approximately the theoretical rate for an excess

hydration factor of 3 ($x=3$). The hydrogen yield decreased with use of coated beads to approximately 20%. This smaller yield could be caused by channeling in the reactor. This theory is supported by the observation that when the reacted beads were contacted with 15 mol % acetic acid, they continue reacting, indicating that not all $NaBH_4$ was contacted with steam.

Separate aqueous solutions of 1 mol%, 6.5 mol% and 15 mol% of methanol and 1mol% of acetic acid were investigated. The initial rate of the reaction was about the same regardless of the type or concentration of the additive, but different yields were obtained. Yields of 68% to 93% of the maximum were obtained with methanol. The best yield with methanol is no higher than yields with pure steam (82% to 94%) as shown in Table 1. The use of acetic acid gave a yield of 100%.

During thermogravimetric analysis the solid byproducts lost approximately 17% mass (free water and water of hydration), but no mass loss occurred above approximately $275^\circ C$. Differential scanning calorimetry analysis produced two peaks around $100^\circ C$ and $150^\circ C$, which tentatively are ascribed to structural transformations from changes in the degree of hydration of the borate. In this range of temperatures the TGA indicates that the sample is still losing water.

Conclusions

The data show that more than an 80% yield of H_2 can be obtained when $NaBH_4$ powder reacts with pure water vapor. Sodium borohydride powder gave high yields with slow rates and excessive use of water. Higher rates were obtained with thin films of $NaBH_4$ recrystallized on glass beads, while yields were low, potentially due to channeling in the reactor. The rates and yields are sensitive to operating temperature, the amount of water and physical form of $NaBH_4$.

The intrinsic reaction kinetics may be obscured because of impermeable byproducts. The TGA and DSC analysis showed the presence of free water in the solid byproduct, which affects the gravimetric efficiency of the system. Further understanding of the by-product properties and refinement in the reactor configuration will help to increase the rate and yield of the reaction and reduce the amount of excess water. These improvements may give insight to improve the mass efficiency of the system and will make this technology viable as a medium for hydrogen storage.

Acknowledgement. This work was carried out under Agreement No. DAAB07-03-3-K416 with the US Army Communications-Electronics Command (CECOM) for Hybrid Advanced Power Sources with guidance from the RDECOM / CERDEC Fuel Cell Technology Team at Fort Belvoir, VA and the Agreement No. DE-FC36-04GO14232 with the Department of Energy.

References

- [1] Aiello R.; Sharp J.; Matthews M. *International Journal of Hydrogen Energy*; **1999**, 1123-1130.
- [2] Amendola et al., J. *Hydrogen Energy*, 25, 969, 2000; U.S. Patent 6,534,033
- [3] www.eere.energy.gov/hydrogenandfuelcells/pdfs/freedomcar_targets_explanations.pdf

SYSTEM PERFORMANCE OF A SODIUM BOROHYDRIDE HYDROGEN GENERATOR FOR PORTABLE APPLICATIONS

Richard M. Mohring, Kevin W. McNamara, Mark Boehler, Ying Wu

Millennium Cell Inc.

1 Industrial Way West, Eatontown, NJ 07724

Introduction

Successful implementation of PEM fuel cells for portable applications has been limited due to the lack of a suitable hydrogen source that is energy dense, safe and easy to use. For example, conventional hydrogen storage solutions such as compressed gas and solid-state metal hydrides are unable to deliver the run time in the size and weight specification of the application and require hydrogen recharging.

We report here recent advances in employing chemical hydride based fuel cartridges to provide hydrogen for portable fuel applications at the 20-50 W power output level. System designs and performance data will be discussed.

The power system (dubbed the "P1") consists of a sodium borohydride (NaBH_4) based hydrogen fuel cartridge module developed by Millennium Cell and a 30 W PEM fuel cell power module developed by Protonex Technology Corp., as shown schematically (simplified) in Figure 1. The left portion of the figure represents the hydrogen fuel cartridge, and the right portion represents the fuel cell power module. The fuel cartridge is an implementation of Millennium Cell's Hydrogen on Demand® technology which generates hydrogen based on catalyzed hydrolysis reaction of sodium borohydride^{1,2}. It is envisioned that the fuel cartridge can be disposed of after use.

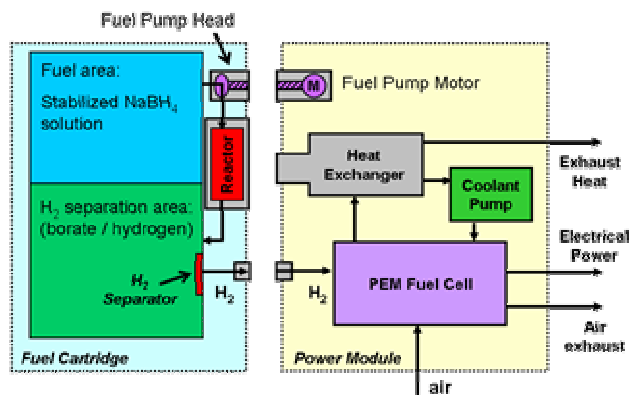


Figure 1. Schematic representation of the Protonex-Millennium Cell P1 power system.

In operation of the system, the fuel solution is moved from the fuel area via a peristaltic pump head mounted on the cartridge. The fuel passes through a thermally managed catalytic reactor and is converted into hydrogen, sodium metaborate, and water vapor. The products enter a separation area, and hydrogen is allowed to escape to an outlet tube through a hydrophobic membrane, where it is then passed to the fuel cell for consumption.

In order to operate the system, the two halves are mechanically coupled together. Two notable design features are the coupling of the fuel pump and heat exchanger. Although the peristaltic pump head is located on-board the fuel cartridge, the motor drive for the pump is actually located within the power module. This offers a

number of advantages: there is no liquid-liquid interconnect, and as a result the potential for fuel leakage is minimized. Furthermore, it allows the motor to be reused for multiple cartridges, whereas the relatively inexpensive pump head can be disposed of with each cartridge as it is consumed.

Similarly, an inexpensive metal reactor is fitted with a thermally conductive fin which comes into intimate physical contact with a fixed heat exchanger (normally used for thermal management of the fuel cell) onboard the power module when the system halves are joined. In this way, the thermal conditions of the reaction can be accurately controlled.

Experimental

For purposes of detailed experimentation on the fuel cartridges, Millennium Cell developed a so-called "power module simulator" that in essence replaces the fuel cell system with instrumentation. As shown in Figure 2, the fuel cell itself is replaced by a thermal mass flow meter, so that the flow of hydrogen can be accurately measured and/or set at a particular level. The heat exchanger remains, but is controlled off a separate control loop based on the reactor temperature.

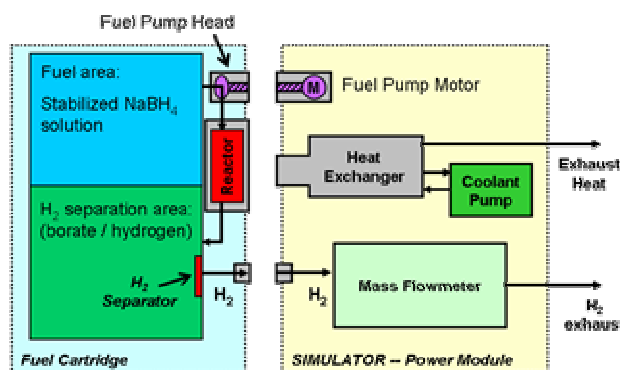


Figure 2. Schematic representation of the Millennium Cell fuel cartridge in relation to the power module simulator.

The performance of the fuel cartridge was evaluated under various conditions and results are reported below. The fuel used in performance evaluation was an aqueous solution of NaBH_4 in the 15-25 wt% concentration range, with 3 wt% NaOH as stabilizer. Most experimentation was done at room temperature, though limited tests were conducted at $\sim 5^\circ\text{C}$ and $\sim 35^\circ\text{C}$.

The hydrogen stream was passed through a drying column before the flow rates were measured using a mass flow meter. A number of thermocouples were attached to selected locations on the fuel cartridge and simulator to record reactor temperature, hydrogen stream temperature, and skin temperature of the fuel module. In experiments where real-time conversion efficiencies were measured, the fuel reservoir was placed on a scale so that the fuel consumption was recorded by the weight loss of the fuel reservoir.

Results and Discussion

The conversion efficiency of sodium borohydride fuel was first evaluated. Although the system was designed to operate at an average of 425 sccm of hydrogen output (corresponding to approximately 30 W net electrical output), it was desirable that the conversion from sodium borohydride to hydrogen was as close to quantitative as possible over a much wider hydrogen flow output window. To this effect, the hydrogen yield was measured at a number of drastically different flow rates of the borohydride

solutions. As the data in Figure 3 show, highly efficient conversions were achieved over two orders of magnitude of hydrogen flow rate, from 10 sccm to 1000 sccm.

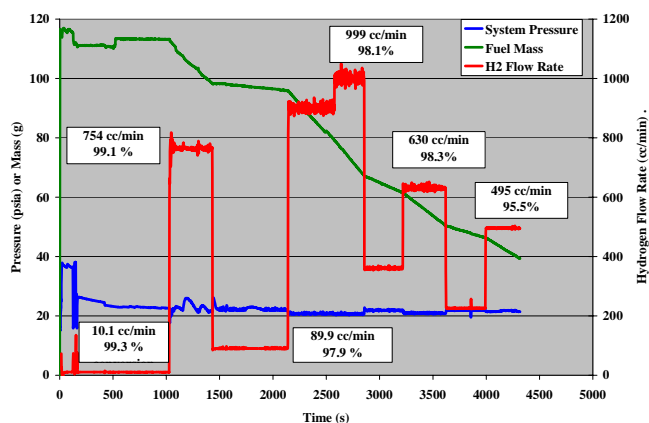


Figure 3. Hydrogen flow rates and corresponding borohydride conversion measured at various output levels.

In initial development, the fuel module was sized to achieve 12 hours of run time using 16 wt% borohydride solution. Figure 4 shows the test results of a typical full run evaluation at that concentration. The mass flow control was set to allow a constant hydrogen flow rate of 425 sccm, which corresponds to the final desired electrical power output. In these experiments, run time ranged between 11.0 and 12.2 hours, with borohydride conversion efficiency in the 93 – 100% range.

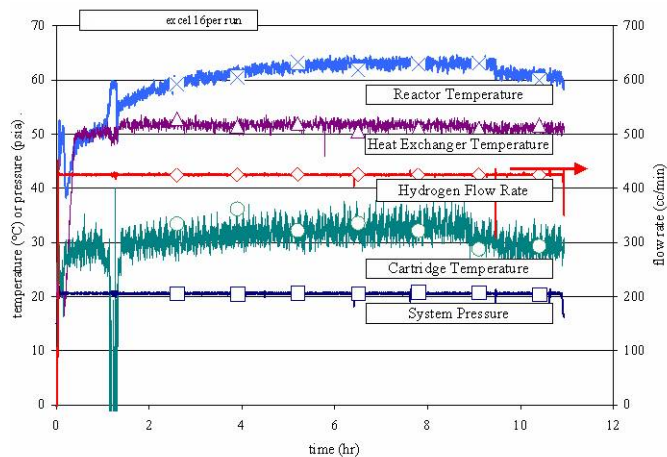


Figure 4. Cartridge data for full run on 16 wt% borohydride fuel. Hydrogen output was fixed at 425 sccm, and system pressure was controlled to maintain ~20 psia within the cartridge.

In further development, an integrated heat management technology was implemented to allow for use of higher concentration borohydride solutions. In the absence of thermal management, the conversion efficiency of the fuel drops as fuel concentration is increased³. Qualitatively, as the fuel concentration is increased, the reduction of availability of water as both a solvent and as a reagent negatively impacts the ability to complete the hydrolysis reaction. By keeping the temperature within a certain narrow window via thermal management, the vaporization of water can be kept to a minimum while not significantly decreasing the kinetics of the hydrolysis reaction.

Figure 5 shows the result of an experiment running on 20 wt% borohydride fuel. For this run, the cartridge was operated for 7 hours, stopped overnight, and operated for the remaining 9 hours of fuel stored within the cartridge on the second day. The experiment showed approximately 16 hours of operation, which greatly exceeded the design specification of 12 hour run time. With these improvements, the system was able to achieve a projected gravimetric energy density of 340-395 Wh/kg (depending on power output) based on total loaded system weight for a 72 hour mission, verified by independent testing⁴.

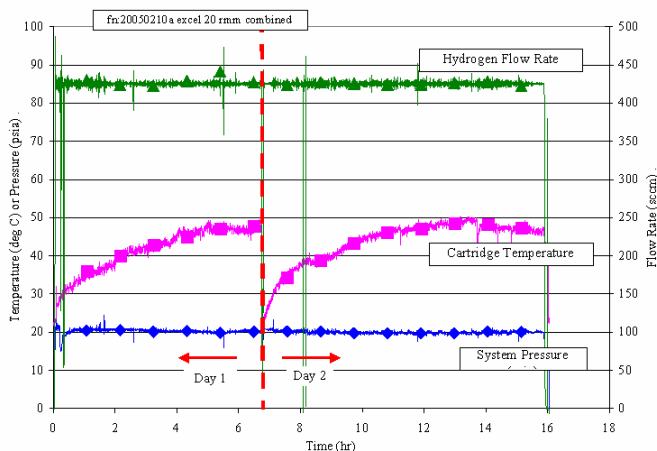


Figure 5. Data for full run on 20wt% NaBH_4 fuel, incorporating thermal management to maintain reactor temperature at an optimal set point (not shown). Hydrogen output was fixed at 425 sccm, and system pressure was controlled at ~20 psia within the cartridge.

Future work on this program (“P2”) is directed at increasing the effective gravimetric energy density of the system above 425 Wh/kg for the 72 hour mission, while advancing the readiness level of the technology to be implemented into a field-testable device.

Conclusions

Millennium Cell has implemented its Hydrogen on Demand® technology for hydrogen generation from sodium borohydride into a working prototype 30 W power source. Concentrations of up to 20 wt% sodium borohydride have been consistently operated in the cartridge through a thermal management scheme. Future work will further optimize the thermal management to increase the sodium borohydride concentration that can be reliably processed in the reactor.

Acknowledgement

The authors wish to acknowledge Dr. Thom Reitz and the financial support of the Air Force Dual Use Science and Technology Program, under Technology Investment Agreement, FA8650-04-3-2411. We also want to thank Protonex Technology Corp. for a productive collaboration and many stimulating discussions.

References

- (1) U.S. Patent 6,534,033. **2003**.
- (2) Mohring, R. M.; Wu, Y. *The First International Workshop on Hydrogen in Materials & Vacuum Systems*. Jefferson Lab, Newport News, Virginia, **2002**.
- (3) Hovland, V.; Pesaran, A.; Mohring, R. M.; Eason, I. A.; Smith, G. G.; Tran, D.; Schaller, R.; Smith, R. *Proceedings of Future Transportation Technology Conference*, **2003**.
- (4) Burt, K. *Joint Services Power Expo*, **2005**.

THE NATIONAL HYDROGEN STORAGE PROJECT

Sunita Satyapal¹, Carole Read¹, Grace Ordaz¹, John Petrovic²

- (1) Office of Hydrogen, Fuel Cells and Infrastructure Technologies,
U.S. Department of Energy, 1000 Independence Ave. SW,
Washington, DC 20585
- (2) Los Alamos National Laboratory (on assignment to DOE)

Introduction

U.S. petroleum dependence is driven by transportation, which accounts for two-thirds of the 20 million barrels of oil our nation uses each day. The U.S. imports 55% of its oil, and this is expected to grow to 68% by the year 2025 under a status quo scenario. Nearly all of our vehicles currently run on either gasoline or diesel fuel.

This situation requires that alternative energy carriers be developed to promote future national energy security. Hydrogen has the potential to be a very attractive alternative energy carrier. It can be clean, efficient, and derived from diverse domestic resources, such as fossil (oil, coal, natural gas), nuclear, and renewable (biomass, hydro, wind, solar, geothermal) energy resources. Hydrogen can then be employed in high-efficiency power generation systems, including internal combustion engines or fuel cells for both vehicular transportation and distributed electricity generation.

The potential energy security and diversity benefits of hydrogen are the basis of the Hydrogen Fuel Initiative launched by President Bush in January 2003. The Hydrogen Fuel Initiative commits government funding for accelerated research, development, and demonstration programs that will enable an industry decision on commercialization of hydrogen by the year 2015. Should industry decide to proceed, a full transition to a U.S. hydrogen economy would require decades. Although the implementation of a hydrogen economy would clearly take time, the key point is that research and development to address the viability of hydrogen needs to occur now.

At the present time, there are three primary technology barriers that must be overcome to enable an industry commercialization decision on hydrogen fuel cell vehicles. First, the cost of safe and efficient hydrogen production and delivery must be lowered to be competitive with gasoline without adverse environmental impacts. Second, fuel cell system costs must be lowered while meeting performance and durability requirements. Finally, on-board hydrogen storage systems must be developed that allow a vehicle range of greater than 300 miles while meeting packaging, cost, and performance requirements.

The barriers associated with hydrogen production, delivery and fuel cells are essentially cost-driven. However, with regard to the on-board hydrogen storage barrier, no approach currently exists that can meet the technical requirements of a greater than 300-mile range, irrespective of the present cost. Therefore, the focus of hydrogen storage research is on performance. New materials and approaches are needed. To accelerate and focus R&D in hydrogen storage, the DOE has initiated the implementation of a National Hydrogen Storage Project.

Storage Issues for Hydrogen-Powered Vehicles

Storing enough hydrogen on vehicles to achieve greater than 300-mile driving range is clearly a significant challenge. On a weight basis, hydrogen has nearly three times the energy content of gasoline (120 MJ/kg for hydrogen versus 44 MJ/kg for gasoline). However, on a volume basis the situation is reversed (8 MJ/liter for liquid hydrogen versus 32 MJ/liter for gasoline). On-board hydrogen storage in the range of 5-13 kg is required to encompass the full platform of light duty vehicles. The average fleet on-board storage requirement is approximately 8 kg.

System-Driven Storage Targets

On-board hydrogen storage system targets have been developed through the FreedomCAR Partnership between DOE and the US Council for Automotive Research (USCAR)¹. These targets are *system-driven*, based on achieving similar performance and cost levels as current gasoline fuel storage systems. The storage system includes the tank, valves, regulators, piping, mounting brackets, insulation, added cooling capacity, and any other balance-of-plant components in addition to the first charge of hydrogen and any material such as solid sorbent or liquid used to store the hydrogen. Some of the key targets for the years 2010, and 2015 are shown in Table 1.

Table 1. Hydrogen Storage System Targets

Storage Parameter	Units	2007	2010	2015
Gravimetric energy capacity	kWh/kg (wt. %)	1.5 (4.5)	2.0 (6.0)	3.0 (9.0)
Volumetric energy capacity	kWh/liter (gm H ₂ /liter)	1.2 (36)	1.5 (45)	2.7 (81)
Storage system cost	\$/kWh (\$/kg H ₂ stored)	6 (200)	4 (133)	2 (66)
Cycle life (1/4 tank to full)	cycles	500	1000	1500
Minimum full-flow rate	(g/sec)/kW	0.02	0.02	0.02
Min/Max delivery temp from tank	C	-20/85	-30/85	-40/85
System fill time for 5-kg hydrogen system	min	10	3	2.5
Loss of usable H ₂	(g/hr)/kg H ₂ stored	1	0.1	0.05

Also shown is an example of near-term targets, such as those outlined for the year 2007. High pressure hydrogen tanks and liquid hydrogen meet some, though clearly not all, of the near term (2007) targets. These 2007 targets are therefore primarily for materials-based systems such as solid-state (e.g. metal hydride) or liquid (e.g. chemical hydride) systems. The focus of the DOE National Hydrogen Storage Project is on materials-based technologies to meet 2010 targets and with potential to eventually meet 2015 targets. Targets in interim years such as those shown in 2007 are meant to help guide research efforts, monitor and compare results, and provide feedback to DOE on technical progress to help refocus research and development as required. Currently, research priorities are on achieving the gravimetric and volumetric capacity targets in Table 1. It is important to note that to achieve *system-level* capacities of 2 kWh/kg (6 wt.% hydrogen) and 1.5 kWh/L (0.045 kg hydrogen/L) in 2010, the gravimetric and volumetric capacities of the material alone must clearly be higher than the system-level targets.

Vehicular Hydrogen Storage Approaches

Current on-board hydrogen storage approaches involve compressed hydrogen gas tanks, liquid hydrogen tanks, metal hydrides, carbon-based materials, high surface area sorbents, and chemical hydrogen storage^{2,3}. Tanks, metal hydrides, high surface area sorbents, and carbon-based materials constitute "reversible" on-board hydrogen storage systems, since 'refilling' with hydrogen can take place on-board the vehicle. For chemical hydrogen storage approaches, replenishing the spent hydrogen is not easily

accomplished on-board the vehicle and thus these systems must be regenerated off-board.

The current status of vehicular hydrogen storage systems is shown in Table 2. These values are estimates provided by developers and are continuously updated as progress is made.

Table 2. Current Status of On-Board Hydrogen Storage Systems

Storage Approach	Gravimetric Energy Density (kWh/kg)	Volumetric Energy Density (kWh/liter)	Storage System Cost (\$/kWh)
5000-psi gas tanks	1.9	0.5	\$15
10,000-psi gas tanks	1.6	0.8	\$18
Liquid H ₂ tanks	1.7	1.2	\$6
Metal hydrides*	0.8	0.6	\$16
Chemical hydrides	1.4	1.0	\$8
2010 System Target	2.0	1.5	\$4
2015 System Target	3.0	2.7	\$2

*Projection

As will be noted, none of the current systems meets the combined gravimetric, volumetric, and cost targets for either 2010 or 2015. Each of the current approaches will now be discussed in more detail.

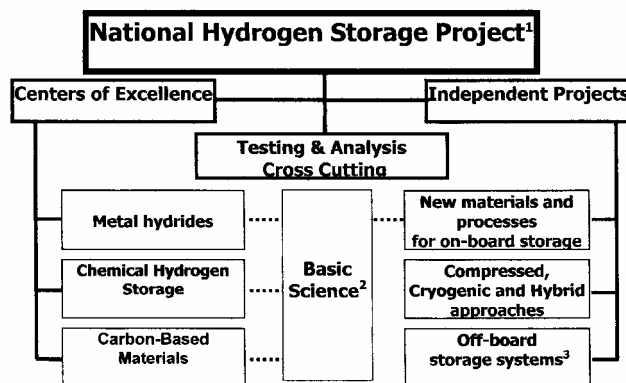
The National Hydrogen Storage Project

The Department of Energy has conducted a number of workshops to identify R&D priorities and strategies for on-board hydrogen storage. These include a Hydrogen Storage Materials Workshop held in August 2002, a Compressed/Liquid Hydrogen Storage Workshop held in October 2002, a Hydrogen Storage "Think Tank" Meeting held in March 2003, and a Basic Energy Sciences Workshop held in May 2003. The proceedings of these workshops are available on DOE websites⁴.

Based on inputs from the workshops, the DOE issued a "Grand Challenge" to the global scientific community for research in hydrogen storage in July 2003. This Grand Challenge called for the establishment of hydrogen storage Centers of Excellence on Metal Hydrides, Chemical Hydrogen Storage, and Carbon-Based Materials, with multiple university, industry, and federal laboratory partners. In addition, independent projects were solicited on new materials and concepts, off-board hydrogen storage systems, and analyses of life cycle cost, performance and environmental impact. Complementing the Grand Challenge, the DOE Office of Science issued a solicitation in 2004 for basic research to help overcome key hurdles in hydrogen production, storage, and conversion.

The new Centers of Excellence and independent projects, together with existing DOE hydrogen storage efforts, constitute the framework of the National Hydrogen Storage Project in the United States. The structure of the National Hydrogen Storage Project is shown in Figure 1. The Secretary of Energy announced the selections for the Hydrogen Storage Grand Challenge on 27 April 2004. These activities support the President's Hydrogen Fuel Initiative, announced in 2003, which pledged \$1.2 billion over five years (FY 2004 to 2008) to accelerate hydrogen research. The DOE plans to provide funding at a level of \$150 million over a five year period (subject to congressional appropriations) for the National Hydrogen Storage Project. The result of this R&D effort will be the development of hydrogen storage systems capable of meeting the long-term DOE targets.

The Metal Hydride Center includes Sandia National Laboratories in Livermore, California and multiple university and industrial partners. The Metal Hydride Center focuses on the development of advanced metal hydride materials including light-weight advanced complex hydrides, destabilized binary hydrides, intermetallic hydrides, modified lithium amides, and other on-board reversible hydrides. The Center involves 7 universities, 3 industrial partners, and 5 federal laboratories.



1. Coordinated by DOE Energy Efficiency and Renewable Energy, Office of Hydrogen, Fuel Cells and Infrastructure Technologies
2. Basic science for hydrogen storage conducted through DOE Office of Science, Basic Energy Sciences
3. Coordinated with Delivery program element

Figure 1. Structure of The National Hydrogen Storage Project.

The Chemical Hydrogen Storage Center includes the Los Alamos National Laboratory in Los Alamos, New Mexico and the Pacific Northwest National Laboratory in Richland, Washington. The Chemical Hydrogen Center focuses on three "tiers" of R&D for chemical hydrogen storage: borohydride-water, novel boron chemistry, and innovation beyond boron. The Center involves 6 universities, 3 industrial partners, and 2 federal laboratories.

The Carbon-Based Materials Center includes the National Renewable Energy Laboratory in Golden, Colorado. The Carbon-Based Materials Center focuses on breakthrough concepts for storing hydrogen in high surface area sorbents such as hybrid carbon nanotubes, aerogels, and nanofibers, as well as metal-organic frameworks and conducting polymers. The Center involves 7 universities, 1 industrial partner, and 4 federal laboratories.

The National Hydrogen Storage Project also involves independent projects on new hydrogen storage materials and concepts, materials and system testing, analyses, and off-board hydrogen storage needed for a hydrogen delivery infrastructure. Some of the new materials and concepts being studied are nanostructured materials, amine borane complexes, metal perhydrides, clathrates, lithium nitride, and irradiation activation of materials. As materials are developed, reliable test data is critical and therefore, to validate hydrogen storage capacities, an independent facility was established at Southwest Research Institute in San Antonio, Texas. This will help ensure unbiased, standardized testing of hydrogen storage materials and systems. Independent analyses is also critical, to help comparatively evaluate approaches and make down-selections. Current analyses activities, primarily by TIAX LLC and Argonne National Laboratory, include storage systems analyses to help optimize weight, volume and cost, as well as life-cycle cost, energy efficiency, and environmental impact analyses. Hydrogen storage analysis is integrated within a broader Systems Analyses and Integration effort within the Hydrogen Program. Thus hydrogen storage will be evaluated in terms of higher level systems

analyses of hydrogen pathways and transition scenarios to assess energy, environmental and economic impacts of hydrogen and fuel cell technologies. Subject to congressional appropriations, early results from the National Hydrogen Project will be reported within the next one to two years. All projects will be reviewed annually at DOE's public meeting (Hydrogen Program- Annual Program Review). Reports are available at <http://www.hydrogen.energy.gov>.

Recent Hydrogen Storage Developments

A new complex hydride system based on lithium amide has been recently discovered⁵. For this system, the following reversible displacive reaction takes place at 285°C and 1 atm: $\text{Li}_2\text{NH} + \text{H}_2 = \text{LiNH}_2 + \text{LiH}$. In this reaction, 6.5 wt.% hydrogen can be reversibly stored. However, the temperature is outside of the vehicular operating window. It has been demonstrated⁶ that magnesium substitution can enhance the dehydriding reaction of LiNH_2 by lowering the dehydriding temperature to 220°C, as shown in Figure 2.

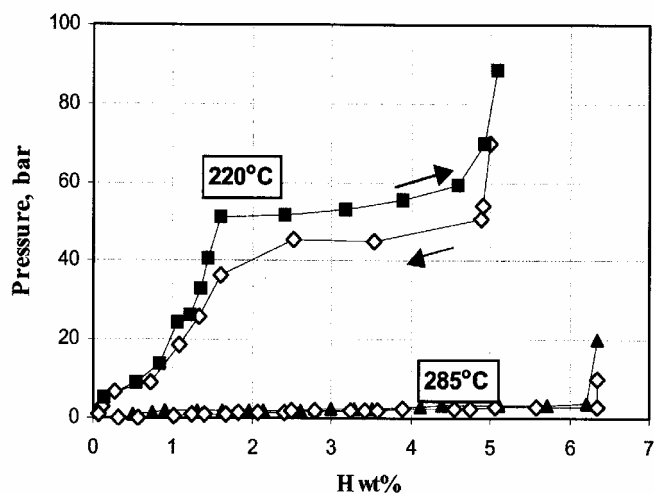


Figure 2. Hydrogen storage characteristics for lithium amide systems.

Single-walled carbon nanotubes (SWNTs), among several other carbon-based materials, are being studied for hydrogen storage.. A recent DOE-sponsored external peer review of hydrogen storage in single-walled carbon nanotubes has shown that experimental techniques used to measure hydrogen storage in carbon nanotubes were reproducible.⁷ Based on experiments observed by the peer review, there was essentially no hydrogen stored in pure SWNTs at room temperature. However, as shown in Figure 3, approximately 2.5 wt.% was observed in metal-doped SWNTs at room temperature. DOE-sponsored work in this area will be expanded to include hydrogen storage in doped carbon nanostructured materials, other than SWNTs, both at room temperature and low temperatures (e.g. 77 K).

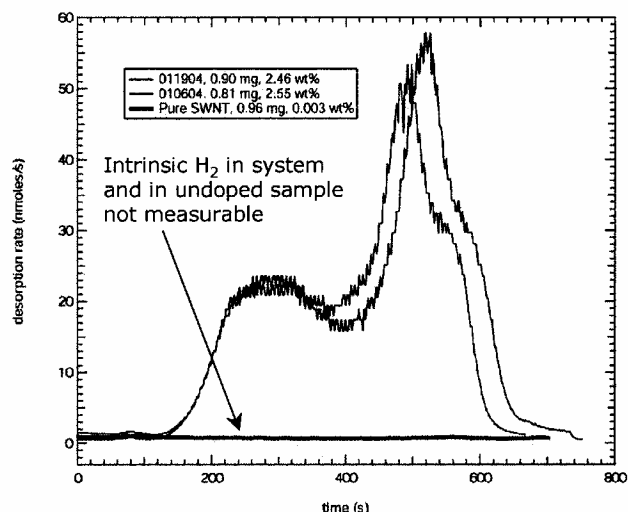


Figure 3. TPD desorption thermogram obtained for pure and metal-doped single-wall carbon nanotubes at room temperature.

Recently, a new type of liquid phase hydrogen storage material has been developed⁸. This liquid, based on N-ethylcarbazole, has been shown to possess a 5-7 wt.% gravimetric hydrogen storage capacity and a greater than 0.050 kg/L hydrogen volumetric capacity. Figure 4 shows the hydrogen evolution from N-ethylcarbazole with cycling at 197°C.

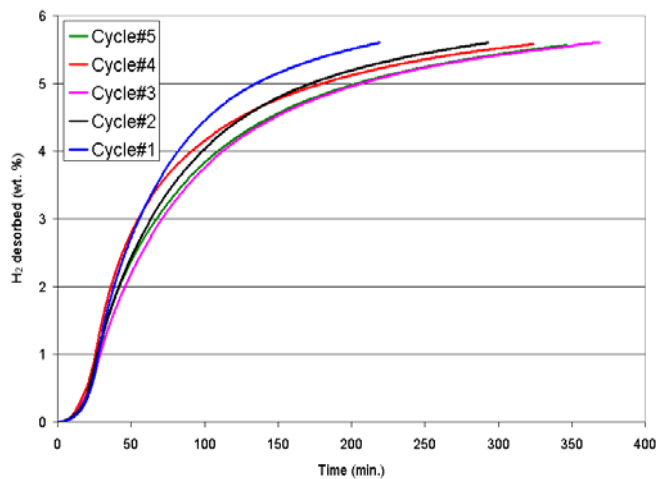


Figure 4. Cyclic desorption of hydrogen from N-ethylcarbazole at 197°C and 1 atm pressure.

Summary

The U.S. Department of Energy has established The National Hydrogen Storage Project to address the technologically-difficult issue of storing enough on-board hydrogen to allow a greater than 300-mile range for hydrogen-powered vehicles, which is a critical element required for the success of the Hydrogen Economy. The National Hydrogen Storage Project encompasses Centers of Excellence in Metal Hydrides, Chemical Hydrogen Storage, and Carbon-Based Materials, as well as Independent Projects and Basic Science projects. A large number of universities, industrial organizations, and federal laboratories are engaged in this research which is targeted at hydrogen storage in materials. Significant improvements in the capacities of on-board vehicular hydrogen

storage systems are expected to result from this DOE-sponsored Project. In addition to U.S. activities, the DOE is supporting the mission of the International Partnership for the Hydrogen Economy (IPHE), formed in November, 2003, to advance the transition to a global hydrogen economy. Along with Italy, Russia and the European Commission, the DOE is leading the first IPHE conference on hydrogen storage to effectively identify, evaluate and coordinate multinational research, development programs in the key area of hydrogen storage.⁹ Results of these efforts will be available through www.iphe.net and www.hydrogen.gov.

References

1. Hydrogen, Fuel Cells & Infrastructure Technologies Program Multi-Year Research, Development and Demonstration Plan, www.eere.energy.gov/hydrogenandfuelcells/mypp.
2. FY2004 Annual Progress Report for Hydrogen, Fuel Cells and Infrastructure Technologies Program, DOE Office of Hydrogen, Fuel Cells and Infrastructure Technologies, October 2004.
3. Schlappbach, L.; Zuttel, A. *Nature*, **2001**, 414, 353.
4. www.eere.energy.gov/hydrogenandfuelcells, www.sc.doe.gov/bes.bes.html.
5. Chen, P.; Xiong, Z.; Luo, J.; Lin, J.; Tan, K.L. *Nature*, **2002**, 420, 302.
6. Luo, W. *Journal of Alloys and Compounds*, **2004**, 381, 284.
7. M.A. Miller and R. Gorte, Carbon Nanotube Sorption Science: External Peer Review of NREL Activities, Southwest Research Institute Special Report prepared for the U.S. Department of Energy, Office of Hydrogen, Fuel Cells and Infrastructure Technologies, 1 March 2004; NREL Project Report, FY2004 Annual Progress Report for Hydrogen, Fuel Cells and Infrastructure Technologies Program, DOE Office of Hydrogen, Fuel Cells and Infrastructure Technologies, October 2004.
8. Air Products and Chemicals Project Report, FY2004 Annual Progress Report for Hydrogen, Fuel Cells and Infrastructure Technologies Program, DOE Office of Hydrogen, Fuel Cells and Infrastructure Technologies, October 2004.
9. www.iphe.net and references therein.

RELATIVE STABILITY OF $(\text{NH}_3\text{BH}_3)_2$, $[\text{NH}_3\text{-BH}_2\text{-NH}_3]^+ \text{BH}_4^-$, AND $[\text{BH}_3\text{-NH}_2\text{-BH}_3]^- \text{NH}_4^+$

Maciej Gutowski, Rafal Bachorz, Tom Autrey, John Linehan

Chemical Sciences Division, Fundamental Science Directorate,
Pacific Northwest National Laboratory, Richland, WA 99352

Introduction

Hydrogen economy might provide a long-term solution for a secure and environmentally clean energy based on renewable resources.¹ On-board hydrogen storage was identified as a grand challenge for successful deployment of fuel cell technologies.² New materials that store both high gravimetric (≥ 90 gm H_2 / kg) and high volumetric (≥ 82 gm H_2 / liter) densities of hydrogen with operational temperatures between -20 and 85°C are to be identified by the year 2015. In consequence of weak intermolecular interactions between H_2 molecules the volumetric requirements are difficult to meet for pressurized or liquefied hydrogen systems. Storage of H_2 through physisorption is also questionable in view of the anticipated temperature range of operation. Chemical binding of hydrogen in metals or non-metallic systems is being aggressively explored.³

The suitability of the solid NH_xBH_x ($x=1-4$) compounds for hydrogen storage has recently been evaluated using experimental^{4,5,6} and theoretical methods.⁷ The amine boranes have excellent weight percent storage for H_2 with BH_3NH_3 having 19% if 3 molecules of H_2 are produced and the salt $(\text{NH}_4)(\text{BH}_4)$ having 24% if 4 molecules of H_2 are produced. In both cases, the final product would be BN. Thus, the NH_xBH_x series of compounds ($x = 1-4$) are attractive targets for chemical H_2 storage materials. Since the BN unit is isoelectronic with the CC unit, these materials can be viewed as inorganic analogs of hydrocarbons. However, the NH_xBH_x compounds are solids rather than gases at ambient temperatures, due to the greater polarity and the stronger intermolecular interactions as compared to the C_2 organic analogs which are gases. The inherent polarity is dictated by the different electronegativities of the B and N atoms, 2.0 and 3.0, respectively.⁸

The computational results, obtained at the density functional level of theory, for the solids NH_4BH_4 , NH_3BH_3 , and BN and polymers NH_2BH_2 and NHBH , indicate that the NH_xBH_x compounds also display favorable thermodynamics: all four subsequent steps of hydrogen release from NH_xBH_x for x ranging from 4 to 1 are thermoneutral to within 10 kcal/mol.⁷ The close thermoneutrality of hydrogen release from the NH_xBH_x compounds is in significant contrast to hydrolysis pathways of boron based hydrogen storage materials.⁹

The experimental studies have been focused primarily on ammonia borane (AB), NH_3BH_3 , which is a molecular solid with melting temperature of 114°C .^{4,5,6} The release of H_2 from AB can be accomplished at temperatures below 100°C with formation of a complex polyaminoborane $-(\text{NH}_2\text{BH}_2)_n-$. The next step of decomposition develops above 150°C and yields another H_2 , a polyiminoborane material, $-(\text{NHBH})_n-$, and a variable amount of borazine $c\text{-(NHBH)}_3$. The advantageous gravimetric and volumetric properties, as well as thermal decomposition characteristics, make AB a promising material for hydrogen storage.

An ideal material for hydrogen storage would have one additional important property: it would be on-board reversible, i.e., loading of the spent material with gaseous hydrogen should be possible at moderate pressures and with fast kinetics. Unfortunately, the first step of hydrogen release, i.e., $\text{AB} \rightarrow -(\text{NH}_2\text{BH}_2)_n- + \text{H}_2$, is exothermic by 5 kcal/mol for bulk AB⁶ and the entropy term also favors hydrogen release on the account of a translational contribution from the gaseous molecular hydrogen: TAS is typically 9 kcal/mol

for hydrogen release at room temperature. As a result, an on-board rehydrogenation of spent material has not been demonstrated yet for AB.

There are, however, ways to improve the thermodynamics of hydrogen release from AB. First, one can control the chemical nature of products of the dehydrogenation step. For instance, we have demonstrated that the products of dehydrogenation are different for (i) AB confined in nanoporous templates and (ii) bulk AB.⁶ In consequence, the first dehydrogenation step becomes practically thermoneutral for AB confined in a nanoporous template, which is a significant improvement in comparison with $\Delta\text{H}=-5$ kcal/mol for bulk AB.

The second way to improve the thermodynamics of hydrogen release is to modify the reactant. Ammonia borane is not the only compound with the empirical formula NBH_6 . It was demonstrated in a series of experiments that there is another compound, diammoniate of diborane (DADB), $[\text{NH}_3\text{-BH}_2\text{-NH}_3]^+ \text{BH}_4^-$; see an excellent summary by Parry on the synthesis and characterization of DADB.¹⁰ AB and DADB may be viewed as the products of symmetrical and unsymmetrical cleavage, respectively, of B_2H_6 . The synthesis of AB and DADB is currently well controlled, but very little is known about the physicochemical properties of DADB. The different properties of AB and DADB might be critical for hydrogen storage in the NBH materials. In particular, the thermodynamic stabilities of DADB and AB might be different. It is critical to characterize the structural and thermodynamic properties of DADB.

If $[\text{NH}_3\text{-BH}_2\text{-NH}_3]^+ \text{BH}_4^-$ is a viable material, it might be instructive to characterize also its “umpolung” counterpart,¹¹ i.e., $[\text{BH}_3\text{-NH}_2\text{-BH}_3]^- \text{NH}_4^+$. Per analogy with DADB and the umpolung relation, the latter will be named here “DBDA”, see Fig. 1.

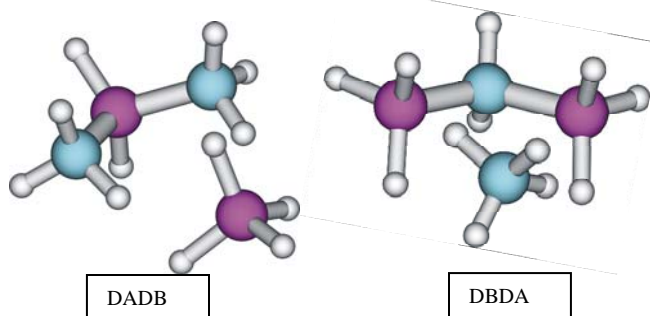


Figure 1. The boron atoms are colored in magenta, nitrogens in blue. Left, an ionic pair $[\text{NH}_3\text{-BH}_2\text{-NH}_3]^+ \text{BH}_4^-$, which is the simplest fragment of DADB. Right, an ionic pair $[\text{BH}_3\text{-NH}_2\text{-BH}_3]^- \text{NH}_4^+$, which is the simplest fragment of DBDA.

The properties of molecular complexes $(\text{AB})_2$, DADB, DBDA will be characterized in this report based on the results of electronic structure calculations.

Methods

Optimal geometries of NH_3BH_3 , NH_4^+ , BH_4^- , and complexes $(\text{NH}_3\text{BH}_3)_2$, $[\text{NH}_3\text{-BH}_2\text{-NH}_3]^+ \text{BH}_4^-$, and $[\text{BH}_3\text{-NH}_2\text{-BH}_3]^- \text{NH}_4^+$ were determined at the second-order Moller-Plesset (MP2) level of theory using augmented, correlation consistent, triple-zeta basis sets.¹² The MP2 Hessians (matrices of second derivatives of electronic energy with respect to geometrical degrees of freedom) were determined at stationary points. Final single-point calculations were performed at the coupled-cluster level of theory with single, double, and non-iterative triple excitations¹³ (CCSD(T)) at the optimal MP2

geometries. The relative electronic energies were first corrected for zero-point vibrations. Next, thermal corrections as well as the entropy terms were calculated for T=298 K and p=1 atm in the harmonic oscillator-rigid rotor approximation to derive the relative stability in terms of Gibbs free energy.

Let us illustrate our method of determination of intermolecular binding energy on the example of AB. The binding energy in a complex formed by the monomers A and B is split into the two-body interaction energy and a repulsive term that accounts for distortion of the monomers in the AB complex:

$$E_{bind}^{CP} = E_{int}^{CP} + \Delta E^{OB}$$

The interaction energy between monomers is corrected for basis set superposition error using the function counterpoise method of Boys and Bernardi¹⁴

$$E_{int}^{CP} = E^D(G^D, B^D) - (E^A(G^D, B^D) + E^B(G^D, B^D))$$

and the one-body term is given by

$$\Delta E^{OB} = \sum_J (E^J(G^D, B^J) - E^J(G^J, B^J))$$

where:

E^D - energy of the dimer.

E^A, E^B - energies of the monomers.

G^D, G^A, G^B - geometry of the dimer, monomer A, monomer B, respectively.

B^D, B^A, B^B - basis set of the dimer, monomer A, monomer B, respectively.

Results and Discussion

$N_2B_2H_{12}$ can be viewed as either $(AB)_2$, or DADB, or DBDA, see Fig. 2.

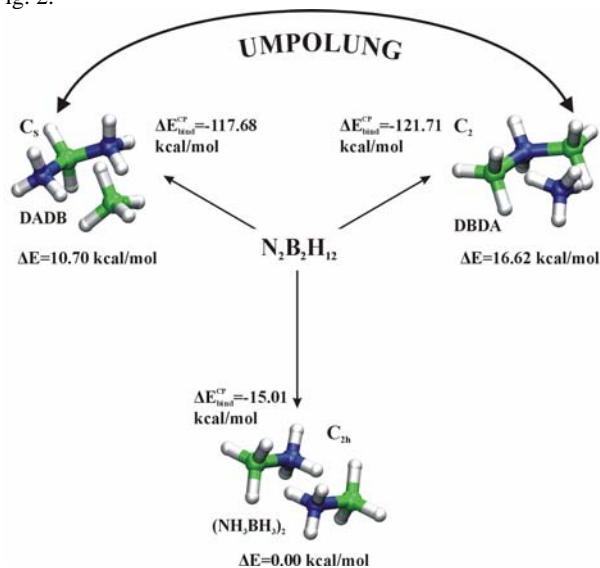


Figure 2. The relative stability of $(AB)_2$, DADB, and DBDA complexes and binding energies determined at the CCSD(T)/aug-cc-pVTZ level of theory. Boron atoms in green, nitrogens in blue.

We will start from the analysis of relative stability of noninteracting monomers, $NH_3BH_3 + NH_3BH_3$, $[NH_3-BH_2-NH_3]^+ + BH_4^-$, and $[BH_3-NH_2-BH_3]^- + NH_4^+$, see Table 1.

Table 1. The relative stability of noninteracting monomers (in kcal/mol) in terms of electronic energy, ΔE_e , electronic energy corrected for zero-point vibrations, $\Delta(E_e + E_o^{vib})$, and Gibbs free energy, ΔG , determined in the harmonic oscillator-rigid rotor approximation for T=298 K and p=1.

Noninteracting Monomers	ΔE_e	$\Delta(E_e + E_o^{vib})$	ΔG
$NH_3BH_3 + NH_3BH_3$	0.0	0.0	0.0
$[NH_3-BH_2-NH_3]^+ + BH_4^-$	114.3	112.9	114.0
$[BH_3-NH_2-BH_3]^- + NH_4^+$	124.0	122.6	123.8

Clearly, formation of ionic pairs $[NH_3-BH_2-NH_3]^+ + BH_4^-$ or $[BH_3-NH_2-BH_3]^- + NH_4^+$ from two NH_3BH_3 monomers is a strongly endothermic process, with the precursors to DADB being more stable than the precursors to DBDA.

The thermodynamically unfavorable step of formation of ionic pairs is compensated to a large extent by a more favorable intermolecular interaction term; see Table 2 and Fig. 2.

Table 2. The counterpoise-corrected values of E_{int}^{CP} , ΔE^{OB} , and E_{bind}^{CP} in kcal/mol.

Complex	E_{int}^{CP}	ΔE^{OB}	E_{bind}^{CP}
$(NH_3BH_3)_2$	-15.5	0.5	-15.0
$[NH_3-BH_2-NH_3]^+ + BH_4^-$	-120.8	3.1	-117.7
$[BH_3-NH_2-BH_3]^- + NH_4^+$	-124.2	2.5	-121.7

The $(NH_3BH_3)_2$ complex has C_{2h} symmetry and therefore a zero dipole moment. The B-N distances are 3.25 Å and the binding energy of -15.0 kcal/mol is a manifestation of polarity of the monomers. The $[NH_3-BH_2-NH_3]^+ + BH_4^-$ complex has C_s symmetry, the B-N distances are 3.07 Å, and the B-B distance is 3.66 Å. Its “umpolung” counterpart, $[BH_3-NH_2-BH_3]^- + NH_4^+$ has C_2 symmetry, the B-N distance is 2.96 Å and the N-N distance is 3.40 Å. Thus, the DADB and DBDA complexes differ not only in the distribution of the positive and negative electrostatic poles, but they also have different symmetries and geometries. Their dipole moments differ significantly: 6.8 and 5.6 D for DADB and DBDA, respectively, in consequence of the differences in interatomic distances. The large dipole moments reflect ionic character of DADB and DBDA. This ionicity also explains large values of binding energy.

Finally, the relative stability of complexes is displayed in Table 3.

Table 3. The relative stability (in kcal/mol) of $(NH_3BH_3)_2$, $[NH_3-BH_2-NH_3]^+ + BH_4^-$, and $[BH_3-NH_2-BH_3]^- + NH_4^+$.

Complex	E_e	$E_e + E_o^{vib}$	G
$(NH_3BH_3)_2$	0.0	0.0	0.0
$[NH_3-BH_2-NH_3]^+ + BH_4^-$	11.4	10.7	10.9
$[BH_3-NH_2-BH_3]^- + NH_4^+$	17.2	16.6	17.7

The relative stability is dominated by the electronic energy contribution with zero-point vibrations and thermal corrections playing only secondary role. The AB dimer is more stable than molecular DADB and DBDA ionic pairs by more than 10 kcal/mol. The relative stability of AB, DADB, and DBDA in solid phases will be further affected by long-range interaction. We found in our earlier DFT calculations that the cohesive energy in AB is 16.6 kcal/mol per

formula unit.⁷ The role of lattice energies in relative stabilities of AB, DADB, DBDA will be analyzed in our future study.

Acknowledgement. This work was supported by the PNNL's Laboratory Directed Research and Development program and the DOE Center of Excellence for Chemical Hydrogen Storage. Computing resources were available through a Computational Grand Challenge Application grant from the Molecular Sciences Computing Facility in the Environmental Molecular Sciences Laboratory. PNNL is operated by Battelle for the U.S. DOE under Contract DE-AC06-76RLO 1830.

References

- (1) See <http://www.eere.energy.gov/hydrogenandfuelcells/>
- (2) MRS Bulletin, vol. 27, issue 9, September 2002.
- (3) Grochala, W.; Edwards, P. P. *Chem Rev.* **2004**, *104*, 1283.
- (4) Baitalow, F.; Baumann, J.; Wolf, G.; Jaenicke-Röbblers, K.; Leitner, G. *Thermochim Acta* **2002**, *391*, 159.
- (5) Autrey, T.; Gutowska, A.; Li, L.; Linehan, J.; Gutowski, M. Prepr. Pap. - *Am. Chem. Soc., Div. Fuel Chem.* **2004**, *49*, 150.
- (6) Gutowska, A.; Li, L.; Shin, Y.; Wang, C.; Li, X-S.; Linehan, J.; Smith, R.S.; Kay, B.D.; Schmidt, B.; Shaw, M.; Gutowski, M.; Autrey, T., submitted for publication.
- (7) Gutowski, M.; Autrey, T. Prepr. Pap. - *Am. Chem. Soc., Div. Fuel Chem.*, **2004**, *49*, 275.
- (8) Pauling, L., *General Chemistry*, Dover Publications, Inc., New York, 1988, p. 182.
- (9) Amendola, S.C.; Sharp-Goldman, S. L.; Janjua, M. S.; Spencer, N. C.; Kelly, M. T.; Petillo, P. J.; Binder, Michael. *Int. J. Hydrogen Energy*, **2000**, *25*, 969.
- (10) Parry, R.W. *J. Chem. Educ.* **1997**, *74*, 512.
- (11) "umpolung" means a reversal of polarity.
- (12) Kendall, R. A.; Dunning, T. H., Jr.; Harrison, R. J. *J. Chem. Phys.* **1992**, *96*, 6796.
- (13) Watts, J. D.; Gauss, J.; Bartlett, R. J. *J. Chem. Phys.* **1993**, *98*, 8718.
- (14) Boys, S.F.; Bernardi, F. *Mol. Phys.* **1970**, *19*, 553.

NEUTRON METROLOGIES FOR HYDROGEN STORAGE

D.A. Neumann, T.J. Udovic, C.M. Brown,
T. Yildirim, M.R. Hartman, and J.J. Rush

NIST Center for Neutron Research
National Institute for Standards and Technology
Gaithersburg, MD 20899-8562

Introduction

The study of hydrogen in materials by neutron scattering, imaging, and trace-analysis techniques is a critical component of any broad-based research program into hydrogen storage systems. For the most part, this is due to the novel properties of the neutron and its interactions with matter, especially the different isotopes of hydrogen. The unusually large neutron scattering cross section for hydrogen can be routinely exploited by a range of experimental neutron methods in order to probe the amount, location, bonding states, and diffusion of hydrogen in any promising hydrogen-storage material. The thermal and cold-neutron beams at NIST and at other neutron scattering facilities combined with state-of-the-art instrumentation provide an array of neutron methods that give researchers access to a wide range of length scales, sensitivity, and dynamic range (Fig. 1).

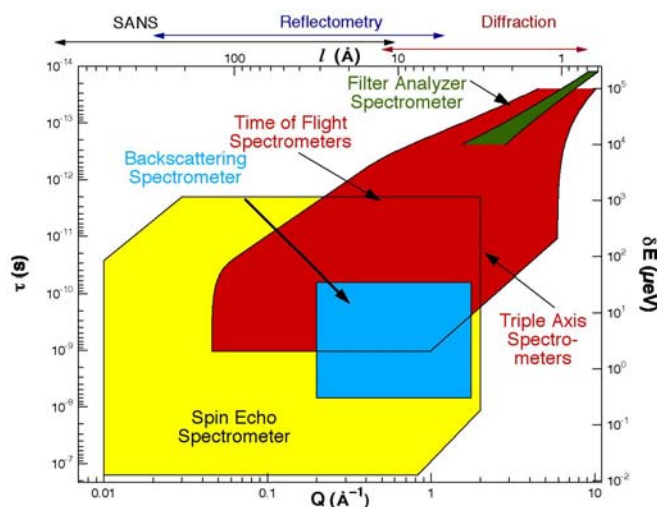


Figure 1. Neutron methods at NIST encompass an enormous range of time and length scales.

Quasielastic Neutron Scattering

Neutron spectroscopic techniques are invaluable for the study of hydrogen diffusion in these materials because of the unique ability of neutrons to simultaneously give information on both the time scale and the atomic scale geometry of the motion. Getting the hydrogen in and out of a hydrogen-storage bed is crucial to devising a functioning hydrogen-storage system. The information provided by quasielastic techniques allows one to develop the detailed understanding of this process required for the atomic scale optimization of these materials. (1)

Inelastic Neutron Scattering

Due to the large scattering cross section for hydrogen, neutron vibrational spectroscopy preferentially probes the motions of the

hydrogen atoms. Thus, while this technique is roughly equivalent to Raman spectroscopy, the information one obtains is particularly relevant for hydrogen storage. Moreover, the simplicity of the interaction between thermal neutron and matter makes it possible to calculate the observed neutron spectrum from any model of the interactions including first principles methods. Such computational results are critical to interpret and to guide experimental studies. Figure 2 shows the measured neutron spectrum compared to *ab initio* calculations that include both one and two phonon processes. (2)

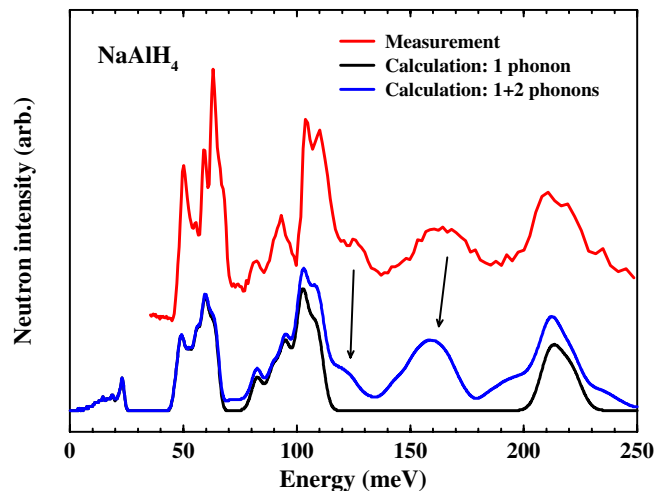


Figure 2. Neutron vibrational spectrum of NaAlH₄ compared with *ab initio* calculations that include one and two phonon processes.

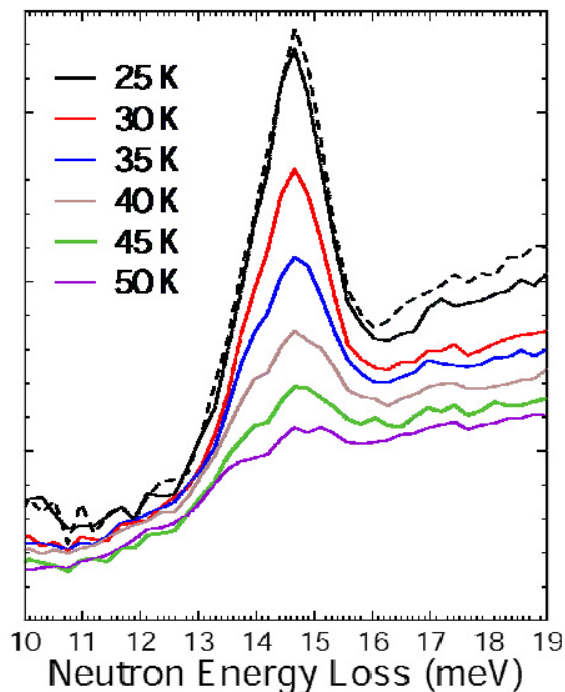


Figure 3. The temperature dependence of the rotational line of hydrogen molecules on single-wall carbon nanotubes. The decrease of intensity is due to hydrogen desorption.

Neutron spectroscopy can also be used to quantify the amount of hydrogen in a sample and can tell if the hydrogen is present as H_2 by measuring the characteristic rotational spectrum of the hydrogen molecule. This type of data also allows one to obtain information on the interactions responsible for binding the hydrogen in these materials. Figure 3 shows the temperature dependence of such a spectrum measured for hydrogen adsorbed on single-wall carbon nanotubes. (3)

Neutron Diffraction

Neutron diffraction is the preeminent technique for determining the crystallographic locations of hydrogen using standard methods including Rietveld refinement. Figure 4 shows a neutron diffraction pattern obtained at NIST for Ti-doped $NaAlD_4$. The refinement allows one to quantify several impurity phases. (4)

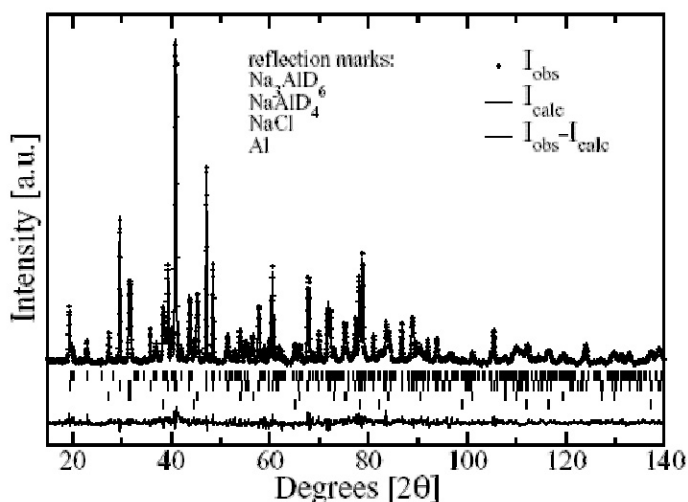


Figure 4. Neutron diffraction results for Ti-doped $NaAlD_4$

Prompt γ activation analysis

Neutrons can also be used to precisely quantify the amount of hydrogen actually present in a material. For example, neutron prompt

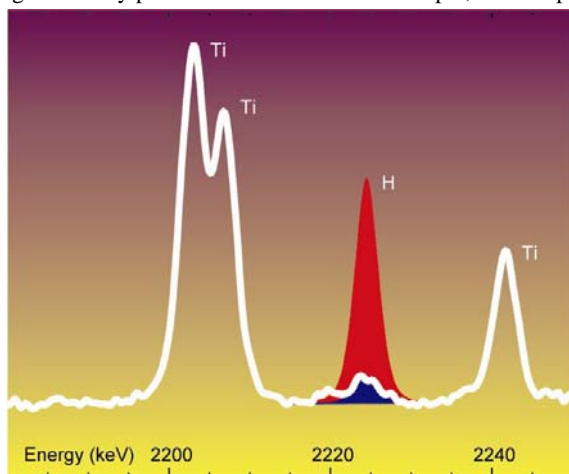


Figure 5. Prompt γ spectra of H in Ti turbine blades for two different processing methods. (5) The difference in the amount of H incorporated in the material is readily apparent. Similar measurements can be made for H in H-storage materials.

γ activation analysis (PGAA) instruments provide *in situ* quantitative analyses of the amount of hydrogen in storage materials down to the microgram level. (Fig. 5) The *in-situ* capabilities currently being developed will allow one to precisely measure the amount of hydrogen adsorbed in materials as a function of temperature and pressure.

Neutron Imaging

One can employ the sensitivity of neutrons to image hydrogen in, *e.g.*, hydrogen-storage beds. Here, current capabilities for neutron imaging and tomography allow one to image hydrogen in real time with a resolution approaching 100 μm (Fig. 6).

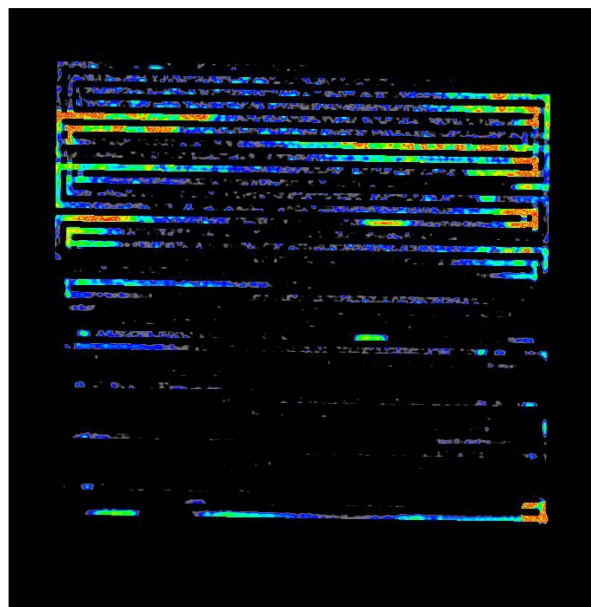


Figure 6. Neutron image of water in flow channels of a PEM fuel cell. See ref. 6.

Conclusion

Finally, it should be noted that all of these capabilities can be employed under conditions of pressure and temperature relevant to those of hydrogen-storage beds. Thus one can obtain information on how hydrogen storage materials will behave under real-world conditions.

Acknowledgements We acknowledge the valuable contributions of the many colleagues we have been fortunate to collaborate with over the years. We are particularly grateful to Muhammad Arif and David Jacobson for the neutron imaging figure and to Dick Lindstrom and Rick Paul for the prompt γ data.

References

- (1) Hempelmann, R. *Quasielastic Neutron Scattering and Solid State Diffusion*, (Oxford University Press, **2001**).
- (2) Íñiguez, J.; Yildirim, T.; Udovic, T.J.; Sulic, M.; and Jensen, C.M. *Phys. Rev. B* **2004**, 70, 060101.
- (3) Brown, C.M.; Yildirim, T.; Neumann, D.A.; Heben, M.J.; Gennett, T.; Dillon, A.C.; Alleman J.L.; and Fischer, J.E. *Chem. Phys. Lett.* **2000**, 329, 311.
- (4) Ozolins, V.; Majzoub, E.H.; and Udovic, T.J. *J. Alloys Compounds* **2004**, 375, 1.
- (5) Paul, R.L.; and Lindstrom, R.M. *J. Radioanal. Nucl. Chem.* **2000**, 243, 181.
- (6) Satija, R.; Jacobson, D.L.; Arif, M.; and Werner, S.A. *J. Power Sources* **2004**, 129, 238.

CHEMICAL REACTION OF AMIDES AND HYDRIDES

Zhitao XIONG, Jianjiang HU, Guotao WU and Ping CHEN*

Physics Department, National University of Singapore, 10 Kent Ridge Crescent, Singapore 119542

Introduction

There are strong pushes towards hydrogen economy worldwide. To overcome one of the technical barriers – onboard hydrogen storage, great efforts have been devoted to the development of solid-state materials, such as carbonaceous materials^{1,2}, alanates³⁻⁵, B-N-H complex⁶ and lithium nitride and imide⁷ etc in the past several years. More recently, two ternary imides, i.e. Li-Mg-N-H and Li-Ca-N-H, were developed in our lab, in which drastic decrease in operation temperatures and uprising hydrogen desorption pressure were achieved.⁸ Interesting results on Li-Mg-N-H system were also reported by Fujii et al.,⁹ Luo¹⁰ and Orimo et al.¹¹ However, to make Metal-N-H system practically viable, systems, especially those ambient temperature systems, are highly needed.

Previous investigations reveal that the hydrogen-rich phases of Li-N-H and Li-Mg-N-H systems comprise of metal amides and hydrides⁷⁻¹¹. It is probably the strong potential for the union of H^{δ+} in amide and H^{δ-} in hydride to H₂ that drives the two chemicals to react and give out hydrogen.¹² Assuming the hypothesis is valid and universal, a serial of new Metal-N-H systems can be developed by reacting various amides with hydrides. In the present work, 7 amide-hydride systems were prepared by mixing amides of Li and Mg with LiAlH₄, MgH₂, NaH and CaH₂, respectively (listed in Table 1). The interaction between amide and hydride was investigated by an in situ planetary ball mill, TPD, volumetric Release-Soak techniques and FTIR. To our expectation, five novel Metal-N-H systems were developed accordingly, among which three systems can release substantial amount of hydrogen (more than 4.2wt%) near ambient temperature.

Experimental

LiNH₂, LiH, NaH, MgH₂, CaH₂, LiAlH₄ are commercially available. Mg(NH₂)₂ was synthesized by reacting Mg nanoparticles with NH₃ at temperature around 300°C. 7 amide-hydride systems, including 2LiNH₂+LiAlH₄ (molar ratio of LiNH₂ to LiAlH₄ is 2/1), Mg(NH₂)₂+LiAlH₄, Mg(NH₂)₂+1.5NaH (1/1.5), Mg(NH₂)₂+CaH₂ (1/1) and 2LiNH₂+MgH₂ were milled in a planetary ball mill at 200 rpm for two days, respectively. Pure LiAlH₄(2g) was also treated under the same conditions. The milling jar is equipped with two gas inlet ports, from which pressure changes in the jar can be monitored by a pressure gauge. The volume of the jar is 194.6ml. ~85g of stainless steel balls were used. After ball milling, the pressure within the jar was measured and the gaseous product was analyzed by Mass Spectrometer and ammonia-sensitive reagent. Only pure hydrogen is the detectable gaseous product. Details are summarized in Table 1. The as-prepared samples were then transferred to a micro-reactor for Temperature-Programmed-Desorption (TPD) testing. The details of TPD testing system and procedure have been described elsewhere.⁷ Quantitative measurements of the hydrogen desorption from the post-milled samples were measured by a gas reaction controller provided by Advanced Materials Corporation. ~ 500 mg samples were tested each time. Results were also summarized in Table 1 and present in Figure 3. X-ray Diffractometer (Bruker D8-advance) and FTIR (PerkinElmer System 2000) have been applied

to detect the structural and bonding changes before and after treatment. As most of the samples are sensitive to moisture, all the sample loadings and transferring were handled in a glovebox provided by MBRAUN.

Results and Discussion

LiAlH₄ only releases 5 psi of hydrogen after two days' ball milling (see Table 1), indicating the local heating due to the collision of balls is unpronounced. Striking high hydrogen pressure was accumulated in the milling jar filled of 2LiNH₂+LiAlH₄ (151 psi), Mg(NH₂)₂+LiAlH₄ (168 psi) and Mg(NH₂)₂+MgH₂ (80 psi) samples, which account for 4.5wt%, 4.2 wt% and 2.4wt% of the starting compounds, respectively. The substantial amount of hydrogen released under the mild ball milling conditions reveals the thermodynamically favored interaction between the above amide and hydride systems. Other amide-hydride systems, i. e., Mg(NH₂)₂+1.5NaH (1/1.5), Mg(NH₂)₂+CaH₂ (1/1), and 2LiNH₂+MgH₂ (2/1), did not release much detectable hydrogen after ball milling (Table 1).

Table 1. Summary of the interaction between variety amides and hydrides

Amide-hydride molecules	Pres H ₂ in BM jar (psi)	No. H released after BM	No. H released after TPD
LiAlH ₄	5	--	--
2LiNH ₂ +LiAlH ₄	151	3.8 (4.5wt%)	3.8 (4.6%)
2LiNH ₂ +MgH ₂	0	0	3.8 (5.3wt%)
Mg(NH ₂) ₂ +LiAlH ₄	168	4.0 (4.2wt%)	1.3* (1.4wt%)
2LiNH ₂ +MgH ₂	0	0	3.8 (5.3wt%)
Mg(NH ₂) ₂ +1.5NaH	0	0	1.9* (2.0wt%)
Mg(NH ₂) ₂ +CaH ₂	9	0.1	2.0 (2.0wt%)
Mg(NH ₂) ₂ +MgH ₂	80	2.0 (2.4wt%)	1.6 (1.9wt%)

* Ammonia appears at temperature above 200°C.

All the post-milled samples were subjected to TPD and volumetric Release testing. Results were presented in Fig. 1 and Table 1. It can be seen that upon heating hydrogen signal appears in the post-milled LiNH₂+LiAlH₄ and Mg(NH₂)₂+LiAlH₄ samples (Fig. 1). ~3.0wt% and 1.4wt% of hydrogen were desorbed at temperatures below 300°C (Table 1), respectively. The general TPD features exhibit remarkable differences from the characteristic decomposition of pure LiAlH₄, LiNH₂ and Mg(NH₂)₂, further evidencing the occurrence of chemical reactions during the ball milling. Little amount of ammonia was detected at temperatures above 200°C.

Heating the post-milled Mg(NH₂)₂+MgH₂ sample comes with hydrogen signals at temperatures above 70°C, remarkably lower than those for the decomposition of individual MgH₂ and Mg(NH₂)₂ (Fig. 1). Additional 1.9wt% of hydrogen was desorbed at temperatures below 300°C. The sharp peak at ~ 400°C is the mixed signals of NH₃, H₂ and N₂, which is probably due to the decomposition of a Mg-N-H compound, such as MgNH.

Desorption of hydrogen from 2LiNH₂+MgH₂ sample starts at temperatures near 100°C and peaks at ~ 170°C (Fig. 1). The temperature range is far below those for the decomposition of pure MgH₂ (above 280°C) and LiNH₂ (above 300°C). The amount of hydrogen desorbed is ~ 5.3 wt% of the solid sorbent (Table 1). Identical TPD features were also observed in Mg(NH₂)₂+2LiH sample.

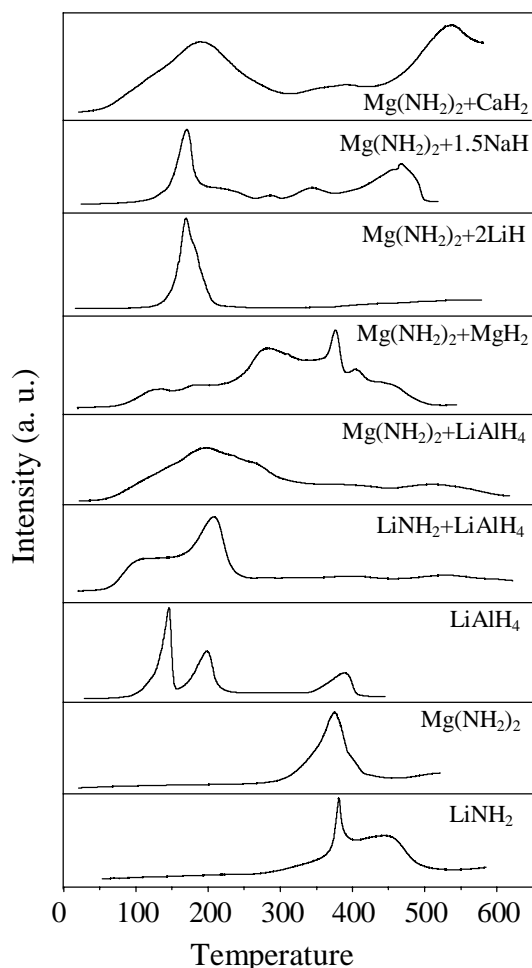


Figure 1. TPD profiles of post-milled samples except LiNH₂ and Mg(NH₂)₂

Post-milled Mg(NH₂)₂+NaH (1/1.5) and Mg(NH₂)₂+CaH₂ (1/1) samples exhibit the majority of hydrogen desorption at temperatures above 50°C with ~ 2.2wt% and 2.0wt% desorption capacity, respectively (Fig. 1 and Table 1). Structural decomposition occurs at temperatures above 350°C.

FTIR was applied to detect changes in N-H bonding before and after hydrogen desorption in Mg(NH₂)₂-based systems. Pristine Mg(NH₂)₂ has the symmetric and asymmetric N-H stretching at 3274 cm⁻¹ and 3328 cm⁻¹, respectively (Fig. 2). After ball milling with LiAlH₄, those stretching vibrations disappear. However, features of imide N-H stretching do not manifest (Fig. 2), indicating the rearrangement of N and H atoms within the sample. The post-milled Mg(NH₂)₂+MgH₂ (1/1) sample also exhibits much depressed -NH₂ characteristics, a broad band in 3100 - 3250 cm⁻¹ was developed instead, which has the characteristics of imide¹². Strong imide-like features were developed in the post-desorbed Mg(NH₂)₂+2LiH sample. Clearly, part of H atoms previously bonded to N was released or transferred during its interaction with hydrides.

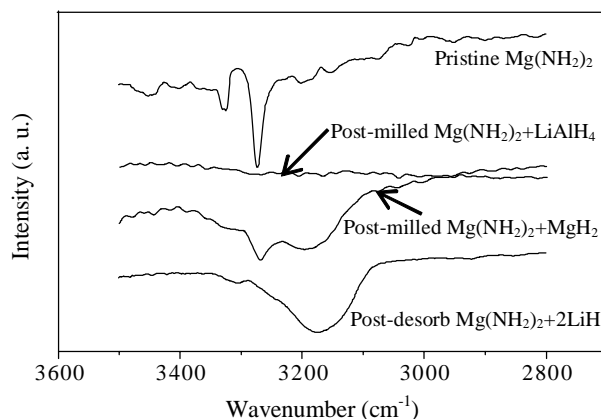
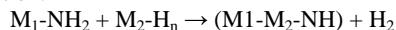


Figure 2. FTIR spectra of Mg(NH₂)₂-based samples

Conclusions

In summary, substantial amount of hydrogen can be released from various amide-hydride systems, demonstrating the universality of the interaction between amides and hydrides. Temperatures for hydrogen desorption are normally far below those for the decomposition of pure constituent compounds, revealing the thermodynamic favor for the interaction. Five new Metal-N-H systems were developed successfully (Table 1), which are worth of further development. As the H-deficient phase of Metal-N-H is somewhat with imide-like behavior, the following equation may account for the general features of the amide-hydride reaction:



M₁ and M₂ represent alkali and/or alkali earth metals. Structural changes before and after interaction appear to be rather important. However, the poor crystallinity of the ball milled samples brings difficulties for the X-ray characterization. The challenges posed to the Metal-N-H system for hydrogen storage purpose are the reversibility (especially for those ambient temperature systems), capacity, and the chemical stability, which are subject to further investigations and optimizations.

Acknowledgement. This work is partially financially supported by Agency of Science, Technology and Research (A*STAR, Singapore).

References

- (1) Rosi, N. L.; Eckert, J.; Eddaoudi, M.; Vodak, D. T.; Kim, J.; O'Keeffe, M.; Yaghi, O. M.; Science, **2003**, 300, 1127.
- (2) Dillon, C.; Jones, K. M.; Bekkedahl, T. A.; Kiang, C. H.; Bethune, D. S.; Heben, M. J. Nature, **1997**, 386, 377.
- (3) Bogdanovic, R. A. Brand, A. Marjanovic, M. Schwickardi, J. Tolle, J. Alloy Comp. **2000**, 302, 36.
- (4) Sun, L.; Srinivasan, S. S.; Kiyobayashi, T.; Kuriyama, N.; Jensen, C. M. J. Phys. Chem. B **2003**, 107, 10176.
- (5) Gross, K. J.; Majzoub, E. H.; Spangler, S. W. J. Alloy Comp. **2003**, 356, 423.
- (6) Baitalow, F.; Baumann, J.; Wolf, G.; Jaenicke-Rossler, K.; Leitner, G. Thermo. Acta, **2002**, 391, 159.
- (7) Chen, P.; Xiong, Z. T.; Luo, J. Z.; Lin, J. Y.; Tan, K. L. Nature, **2002**, 420, 302.
- (8) Xiong, Z. T.; Wu, G. T.; Hu, J. J.; Chen, P. Adv. Mater., 2004,
- (9) Leng, H. Y.; Ichikawa, T.; Hino, S.; Hanada, N.; Isobe, S.; Fujii, H. J. Phys. Chem.B **2004**, 108, 8763.
- (10) W. F. Luo, J. Alloy. Compd **2004**, 381, 284.
- (11) Nakamori, Y.; Orimo, S. J. Alloy. Compd., **2004**, 370, 271.
- (12) Chen, P.; Xiong, Z. T.; Luo, J. Z.; Lin, J. Y.; Tan, K. L. J. Phys. Chem. B, **2003**, 107, 10967.

DOPED SODIUM ALUMINUM HYDRIDE: FUNDAMENTAL STUDIES OF A PROMISING NEW HYDROGEN STORAGE MATERIAL

Craig M. Jensen¹, Sessa S. Srinivasan¹, Rosario Cantelli², Oriele Palumbo², Annalisa Paolone^{2,3}, Carmen M. Andrei⁴, Randi Holmstad⁴, J.C. Walmsley⁵, Bjørn C. Hauback⁶, Hendrik W. Brinks⁶, Meredith Kuba¹, Sandra Eaton⁷, Dalin Sun¹, Keeley Murphy¹, and Ping Wang¹

- 1) Department of Chemistry University of Hawaii, Honolulu, HI 96822.
- 2) Università di Roma "La Sapienza", Dipartimento di Fisica, Piazzale A. Moro 2, I-00185 Roma, Italy.
- 3) Istituto Nazionale per la Fisica della Materia, Corso Perrone 24, I-16152 Genova, Italy.
- 4) Department of Physics, Norwegian University of Science and Technology, 7491 Trondheim, Norway.
- 5) SNTF Materials and Chemistry, 7465 Trondheim, Norway.
- 6) Institute for Energy Technology, P.O. Box 40 Kjeller, NO-2027 Norway.
- 7) Department of Chemistry and Biochemistry, University of Denver, Denver, CO 80208.

Point Defect Dynamics and Evolution of Chemical Reactions in Alanates by Anelastic Spectroscopy

We conducted the first measurements of elastic modulus and energy dissipation in Ti-doped and undoped sodium aluminium hydride. We have found that the dehydrogenation of the hydride can be monitored through its effects the elastic constants. After a well defined thermal treatment, a thermally activated relaxation process appears at 70 K in the kHz range. This denotes the existence of a new species, likely involving hydrogen, has a very high mobility. The species is estimated to "jump" at rate of $10^3/s$ at the peak temperature corresponding to a relaxation rate of about $10^{11} s^{-1}$ at room temperature. The activation energy of the process is 0.126 eV and the pre-exponential factor $7 \cdot 10^{-14} s$, which is typical of point defect relaxation. The peak is very broad with respect to a single Debye process, indicating strong interaction or/and multiple jumping type of the mobile entity. The present data suggest that the indicated point-defect dynamics and stoichiometry defects should be included models of the reversible elimination of hydrogen from the doped hydride.

Electron-microscopy Studies of NaAlH₄ with TiF₃ Additive: Hydrogen Cycling Effects

The microstructure of NaAlH₄ doped with 2 mol % TiF₃ studied under different conditions using a combination of transmission electron microscopy and scanning electron microscopy, both with energy-dispersive spectroscopic X-ray analysis. The effect of the additive on particle and grain size was examined after the initial ball-milling process and after 15 cycles. The additive has an uneven distribution in the sample after ball milling. Selected-area diffraction and high-resolution imaging confirmed the presence of TiF₃. This phase accounts for most of the Ti in the material at this stage and showed limited mixing with the alanate. The grain size within particles for TiF₃ is larger than for the alanate particles. Diffraction from the latter was dominated by metallic aluminium. After cycling, the TiF₃ has decomposed and energy-dispersive spectroscopic X-ray analysis maps showed some combination of Ti with the alanate phase. There is no significant change in the measurable grain size of the Al-containing alanate particles between the ball-milled and the

15-cycled samples, but more cycles result in agglomeration of the material.

Electron Paramagnetic Resonance Studies of Fluctuating Titanium Species During Reversible Dehydrogenation of Ti-Doped Sodium Alanate

As part of our effort to characterise the active species in Ti-doped NaAlH₄ and elucidate its mechanism of action, we have carried out electron paramagnetic resonance (EPR) spectroscopic studies. We observe a major population of a spin isolated, Ti(III) species in NaAlH₄ immediately following the doping of the hydride with 2 mol % TiF₃. The 8,000-G wide EPR spectrum is dominated by a sharp Ti(III) signal with $g = 1.976$ and $\Delta B_{pp} \sim 90$ G. After one cycle of dehydrogenation-rehydrogenation, the signal is about 70% as intense as in sample before cycling a broader, multi-spin Ti(0) signal is also present with $\Delta B_{pp} \sim 1500$ G. After 3 cycles, the broader signal is about 2.5 times as large as in the sample after 1 cycle. After 5 cycles there is no longer a signal with $\Delta B_{pp} \sim 90$ G or $\Delta B_{pp} \sim 1500$ G, but a dominant, multi-spin Ti(0) signal with $\Delta B_{pp} \sim 650$ G. There is also a signal near zero-field. After 10 cycles, the height of the signal with $\Delta B_{pp} \sim 650$ G is similar to that after 5 cycles, but the signal near zero-field has largely disappeared.

The uncycled spectrum of 2 mol % TiCl₃ doped NaAlH₄ also has a sharp Ti(III) signal with $g \sim 1.97$. Similar to the TiF₃ spectrum after 3 cycles, there is a broad signal with $\Delta B_{pp} \sim 1500$ G and a broad signal near zero-field. Analogous to the TiF₃ sample, one cycle of dehydrogenation-rehydrogenation of the TiCl₃ doped sample causes a substantial decrease in the signal with $g \sim 1.97$. After 3 cycles, the Ti(III) signal at $g = 1.97$ is essentially gone. The broader signal with $\Delta B_{pp} \sim 1500$ G continues to evolve in shape. By the time the sample has been cycled 5 times, the spectra are very similar to the TiF₃ spectra. There is now a signal with $g = 2.01$ and $\Delta B_{pp} \sim 650$ G. After 10 cycles the height of the signal with $\Delta B_{pp} \sim 650$ G is only a bit larger than after 5 cycles, as well as a slight increase in height of the signal near zero-field.

The 2 mol % Ti powder doped NaAlH₄ spectrum is remarkably similar to the spectra of TiF₃ and TiCl₃ doped samples after 5 and 10 cycles. There is appearance of the broad signal with $\Delta B_{pp} \sim 500$ G. However, the broad signal at zero-field is absent.

Despite the change in the oxidation state of the titanium, only a minor change occurs in the dehydrogenation and rehydrogenation kinetics of the hydride that is doped using TiF₃. Furthermore, although initially the relative amounts of Ti(III) and Ti(0) are radically different in Ti-doped NaAlH₄, depending on whether the hydride is doped using TiF₃ or TiCl₃ as dopant precursor, virtually identical kinetics are observed for the first 3 cycles of dehydrogenation-rehydrogenation regardless of which dopant precursor is employed. These findings suggest that the enhanced hydrogen cycling kinetics are due to a Ti species that is present in only a relatively minor amount. The slight kinetic improvement that is observed beyond the third cycle is similar to that observed when the hydride is ball milled without dopant. The finding that a significant amount of the Al-Ti alloy arises after the third cycle then suggests that the alloy is responsible for only this minor kinetic enhancement.

Synchrotron X-ray and Neutron Diffraction Studies of NaAlH₄ Containing Ti Additives

NaAlH₄, Na₃AlH₆ and NaH samples with Ti additives have been investigated by synchrotron X-ray diffraction and neutron diffraction. Directly after the ball milling there are no signs of any Ti-containing phases, and based on unit-cell dimensions of NaAlH₄, Na₃AlH₆ and Al there are no indication of any solid solutions. Combined

refinements of X-ray and neutron diffraction of $\text{Na}_{1-3x}\text{Ti}_x\text{AlD}_4$ and $\text{NaAl}_{1-x}\text{Ti}_x\text{D}_4$ do not give evidence of such solid solutions either. Hence it is concluded that Ti directly after ball milling is in an amorphous state. However, after cycling a shoulder on the high-angle side of the Al reflections appears that is interpreted as a fcc solid solution $\text{Al}_{1-x}\text{Ti}_x$ with $x \approx 0.07$. Furthermore, addition of TiF_3 by ball milling results in different phases compared to $\text{TiCl}_3/\text{TiCl}_4$. The latter gives NaCl, whereas no NaF is formed by the former additive. It has not yet been possible to determine by X-ray diffraction where the fluorine is in the sample.

Preparation of Ti-doped Sodium Aluminum Hydride from Mechanical Milling of NaH/Al with Off-the-Shelf Ti Powder

Ti-doped NaAlH_4 can be directly prepared by mechanical milling a 1:1 mixture of NaH and Al together with a few mole percent of off-the-shelf metallic Ti powder under argon or hydrogen atmosphere. The hydrogen storage materials that are produced through this process exhibit stable hydrogen capacities through 10 cycles of hydrogenation/dehydrogenation. We have conducted a systematic investigation of this new method for the preparation of Ti-doped NaAlH_4 . Consideration of these results, together with those previously obtained for NaAlH_4 that was doped with Ti powder through milling under a hydrogen atmosphere, has provided insight into the nature of active Ti-species.

CHEMICAL CONTROL OF THE THERMAL DECOMPOSITION TEMPERATURE OF MULTINARY HYDRIDES AND COMPLEX HYDRIDES

P. P. Edwards¹, W. Grochala², S. R. Johnson¹, V. Kuznetsov¹ and M. O. Jones¹

¹Department of Chemistry, University of Oxford, South Parks Road, Oxford, OX1 3QR

²The Department of Chemistry, University of Warsaw, Pasteur 1, 02093, Warsaw, Poland

Hydrogen storage is regarded by many as *the* scientific and technological barrier inhibiting a transition to a hydrogen energy economy – certainly for the large scale utilisation of PEM fuel cells in cars¹.

The maximum hydrogen capacity of conventional (heavy) metal hydrides currently remains at around 2wt%, which is inadequate for onboard storage of hydrogen which requires a target gravimetric storage density of at least 6.5wt%. This requirement forces a natural focus on the light chemical elements of the periodic table. Simple atomic, mass-based calculations reveal that the main backbone of any efficient hydrogen storage material (HSM) must only be built from targeted chemical elements from an unforgiving and tantalizingly-short list, Li, Be, B, C, N, O, F, Na, Mg, Al, Si and P. Due to the toxicities and/or unfavourable chemical properties of hydrogen's compounds with Be, F, Si and P, the effective list of chemical cogwheels constituting a Hydrogen Storage Material might only consist of only eight elemental apostles (of course, heavier elements may enter the multi-component system but only as a low-abundant addition, for example, as a catalytic component). From these considerations any target material from our *Light Periodic Table* (Figure 1) is not an over-expansive playground for the chemist. Paradoxically, of course, this is the real intellectual and technical challenge; any revolutionary advance or breakthrough (and one is certainly needed) must derive from a deep understanding – and mastery – of the nature of the chemical and physical interactions of hydrogen with materials derived from our Light Periodic Table. In this presentation, we give a brief overview of our developing programme centred upon an understanding of the thermal decomposition/sorption processes of multinary and complex hydride materials, with a particular emphasis on the rational control and chemical tuning of the strategically important thermal decomposition temperature, T_{dec} , of compounds and materials from the Light Periodic Table.

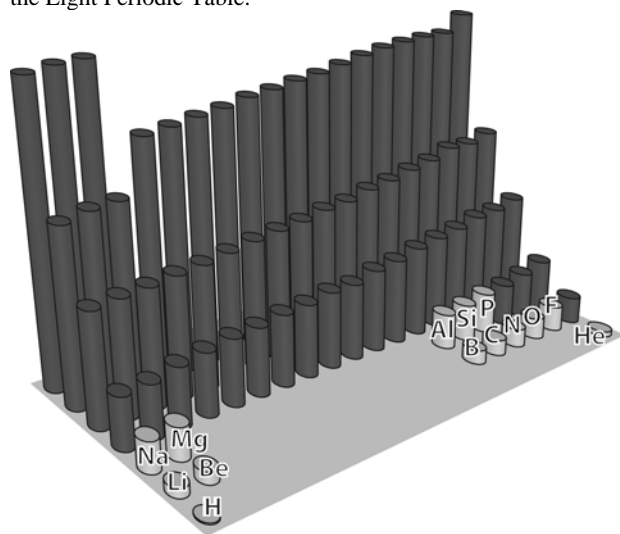
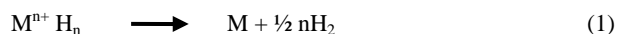
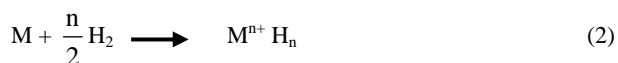


Figure 1. The Light Periodic Table.

From a chemical perspective, the reactions taking part in the decomposition, and thence the recharging of a hydrogen store, can be expressed in the following reduction / oxidation (redox) reactions;



(reductive elimination of H_2)



(oxidative addition of H_2)

where M stands for an element, a lower hydride or potentially even a complex hydride (see below).

Making this direct link with the redox process, it has recently been shown² that T_{dec} is nicely correlated with the standard redox potential for the metal cation / reduced metal electrode potential E^0 . This type of connection is illustrated in Figure 2 which is a representation of the experimental T_{dec} versus E^0 data for a wide variety of binary hydrides. This type of experimental correlation for a broad range of chemically disparate metal hydrides also establishes the beginning of a 'sorting-map' for the important chemical properties of hydrogen stores.

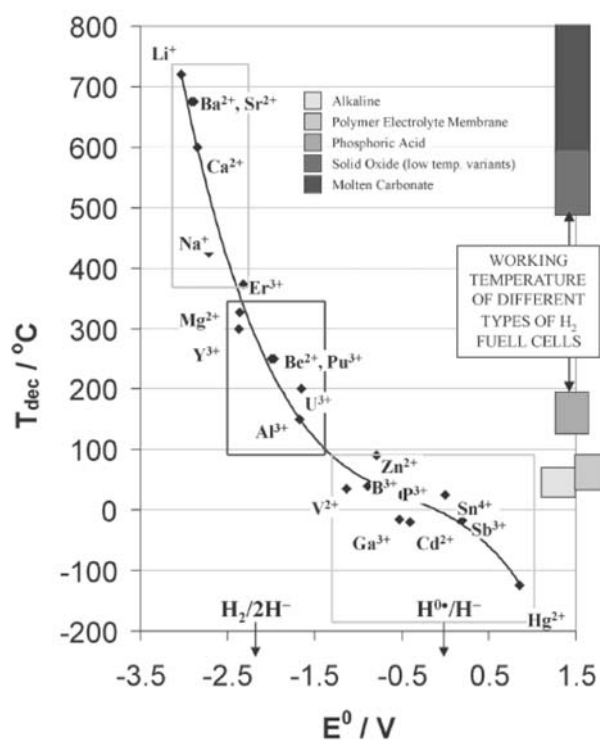


Figure 2. Correlation between temperature, T_{dec} , at which thermal decomposition of binary hydride MH_n to the constituent elements proceeds, and the corresponding redox potential of the redox pair M^{n+}/M^0 in acidic aqueous conditions. The ranges of the working temperatures for prototypical fuel cells are also shown (ref. 2).

Grochala and Edwards² (G and E) also established a rationalisation of this type of behaviour on the basis of thermodynamics and simple theoretical arguments whose origins lie in molecules.

In essence, along with an *increasing* electronegativity of the metal (and corresponding increase of the E^0 value) the energy of the valence orbital of M decreases and the orbitals become more contracted.

A substantial *decrease* of the ionicity of the M-H bonds and a decrease in the actual negative charge on the H centre result. This

type of ‘screen play’ has H^- starting to resemble H^0 more and more as the metal’s electronegativity increases, where the attendant energy barrier for H_2 evolution decreases along with the characteristic T_{dec} . G and E have also attempted³ to broaden the applicability of such an approach to ternary hydrides, and more recently to complex systems such as amido- (NH_2^-), imido- (NH_2^{2-}) and methyl anion (CH_3^-) model complexes of metal cations bound to the tetrahydroborate anion (BH_4^-). In Figure 3 we present the variation of the bridging BH bond lengths plotted against the respective E^0 value for the metal centre (*i.e.* the most typical redox pair associated with the designated oxidation state).

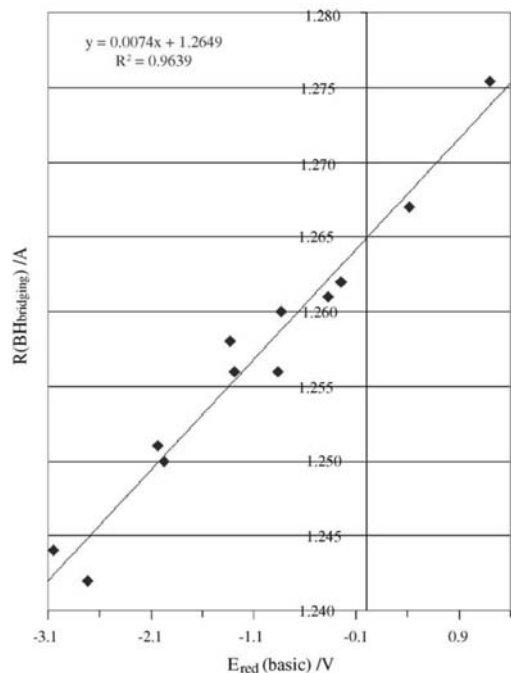
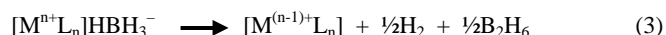


Figure 3. Correlation of bridging B-H bond distances with electrode potential (ref. 3)

In simple, terms, as the redox potential of the central metal centre increases, the bridging B-H bond length of attached BH_4^- anion becomes progressively longer. This important correlation supplements one’s chemical intuition of the third redox reaction associated with the liberation of elemental H_2 (see Eq. (1) and (2)), *viz.*



since the value of the bridging BH bond length signifies the potential early stage of the BH bond rupture reaction yielding nascent H_2 and B_2H_6 .

Here again, as the metal centre becomes a better electron acceptor (enhanced electronegativity), the charge density is transferred from the BH_4^- anion onto $[M^{n+}L_n]$, and the bridging BH bond which participates in the three centre $M \cdots H \cdots B$ bonding becomes weaker and more ionic.

Interestingly, E^0 appears as a valuable predictor of the bond length of the bridging BH bond for a large family of systems, notwithstanding the wide variety of transition metal borohydride chemistries. We thus anticipate that the most potent oxidizing centres should release H_2 (and B_2H_6 via Eqn (3)) most easily... although (unfortunately) most probably irreversibly, in agreement with the earlier analysis of G and E.

In a parallel experimental study⁴, we have highlighted the case of $LiBH_4$ as a highly effective chemical-activation agent, initially for MgH_2 . The hydrogen desorption and absorption kinetics (Figures 4 and 5, respectively) show that the reaction of MgH_2 with quite

modest amounts of $LiBH_4$ results in a spectacular increase in the kinetics of hydrogen desorption/absorption. Importantly, the rate of hydrogen desorption/absorption increased with each successive cycle for the first 4–5 cycles before stabilizing. Both the heat treatment and the initial cycling were necessary to activate the material: cycling a simple mixture of MgH_2 and $LiBH_4$ did not result in such ‘active’ material with fast kinetics

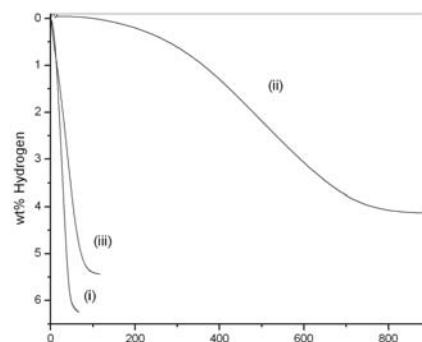


Figure 4. Hydrogen desorption kinetics at 300 °C under 10 mbar H_2 of i) $MgH_2/LiBH_4$, ii) as-received MgH_2 and iii) MgH_2 milled for 15 hrs; all samples measured on the sixth hydrogen desorption (ref. 4).

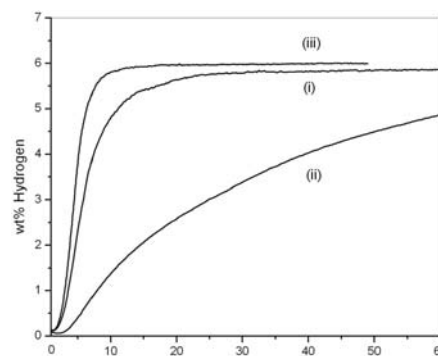


Figure 5. Hydrogen absorption kinetics at 300 °C under 10 bar H_2 of i) $MgH_2/LiBH_4$, ii) MgH_2 and iii) MgH_2 milled for 15 hrs; all samples measured on the sixth hydrogen absorption (ref. 4).

This type of ‘activation’ effectively supplements the approach outlined here. It also dovetails with the emerging route of ‘destabilising’ hydrogen stores via innovative routes⁵.

References

1. US Department of Energy, Office of Science (2004). Basic Research Needs for the Hydrogen Economy. *Report of the Basic Energy Sciences Workshop on Hydrogen Production*, [online]. Available from: <http://www.sc.doe.gov/bes/hydrogen.pdf> Accessed 14 April 2005.
2. W. Grochala and P. P. Edwards, *Chem. Rev.*, **104** (2004) 1283–1315.
3. P. P. Edwards and W. Grochala, accepted by *Journals of Alloys and Compounds*, (2005).
4. S. R. Johnson, P. A. Anderson, P. P. Edwards, I. Gameson, J. W. Prendergast, M. Al-Mamouri, D. Book, I. R. Harris, J. D. Speight and A. Walton, *Chem. Comm.*, **22** (2005) 2823.
5. J. J. Vajo, F. Mertens, C. C. Alm, R. C. Bowman, B. Fults, *J. Phys. Chem. B*, **108** (2004) 13977

Acknowledgements. We thanks thr EPSRC for their support of the UK-Sustainable Hydrogen Energy Consortium (UK-SHEC).

COORDINATION OF B-N SPECIES TO TRANSITION METAL COMPLEXES

Vincent Pons; Melanie C. Denney; Karen I. Goldberg; D. Michael Heinekey

Department of Chemistry, University of Washington, Box 351700, Seattle, WA 98195-1700

Introduction

Hydrogen rich amineborane compounds have recently drawn significant attention since they represent a realistic solution to the problem of hydrogen storage.¹ Indeed, the high weight percentages in hydrogen of ammonia borane (NH_3BH_3) and aminoborane polymer $(\text{BH}_2\text{NH}_2)_x$ both meet the 2015 Department of Energy target. However, in order to develop highly efficient catalysts for the hydrogenation/dehydrogenation of such B-N compounds, a fundamental understanding of the catalytic processes is needed. We present fundamental studies of the coordination of amineborane to unsaturated transition metal complexes as shown in Figure 1.

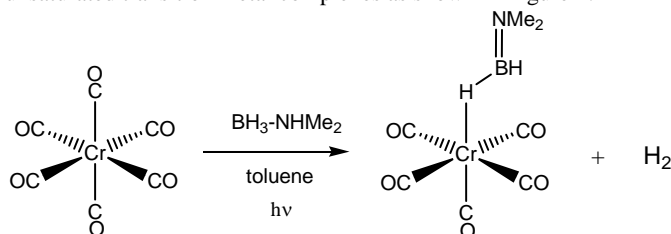


Figure 1. Photolysis of Cr(CO)_6 in toluene in presence of $\text{BH}_3\text{-NHMe}_2$.

Experimental

General Procedures. Unless stated otherwise, all manipulations were carried out under argon using Schlenk techniques. Dimethylamine borane and ammonia borane (Dr Tom Autrey, Pacific Northwest National Laboratory) were used as received. Cr(CO)_6 and W(CO)_6 were purchased and used as received from Sigma-Aldrich. NMR spectra were recorded on Bruker AV-300, AV-301, AV-500 and DRX-499 spectrometers. Proton NMR spectra were referenced to the solvent resonance with chemical shifts reported relative to TMS. The NMR studies were carried out in high-quality 5 mm NMR tubes, utilizing deuterated and protio solvents distilled from standard drying agents.

Photolysis of Cr(CO)_6 in toluene in presence of BH_3NHR_2 ($\text{R} = \text{H}, \text{CH}_3$). A J-Young NMR tube was charged with 3mg Cr(CO)_6 (0.013 mmol) and one equivalent of $\text{BH}_3\text{-NHR}_2$ (0.4 mg, $\text{R} = \text{H}$; 0.8 mg, $\text{R} = \text{Me}$). After addition via vacuum transfer of toluene (*ca* 1 mL), the resulting colorless solution was photolyzed (Hg lamp, 200 K) for 30 minutes to one hour to give a yellow solution. The coordination of borane species was monitored by ^1H and ^{11}B NMR (see discussion).

Results and Discussion

Photolysis of a toluene solution of chromium hexacarbonyl and one equivalent of Me_2NHBH_3 at 200 K leads to loss of H_2 , formation of $\text{NMe}_2\text{=BH}_2$ and the cyclic dimer $(\text{NMe}_2\text{-BH}_2)_2$. At 180 K, three peaks are observed in the hydride region of the ^1H NMR spectra at -9.34, -13.87 and -18.1 ppm (Figure 2).

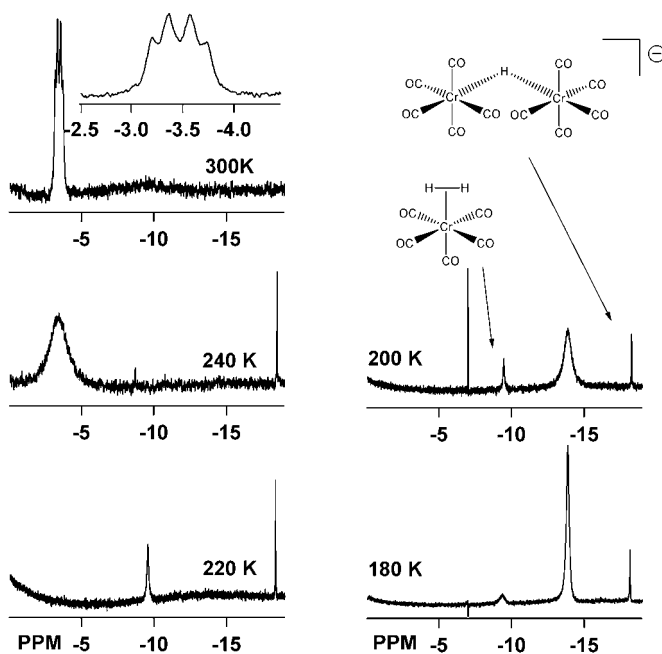


Figure 2. Variable temperature ^1H NMR spectra of $[\text{Cr(CO)}_5(\eta^1\text{-BH}_2\text{=NMe}_2)]$ (toluene- d_8 , 499 MHz).

They are assigned to $[\text{Cr(CO)}_5(\text{H}_2)]$,² $[\text{Cr(CO)}_5(\eta^1\text{-BH}_2\text{=NMe}_2)]$ and the bridging hydride dimer $[(\text{CO})_5\text{Cr}(\mu\text{-H})\text{Cr(CO)}_5]$ respectively. Due to their thermal instability, as the temperature is raised the resonances corresponding to the dihydrogen complex and the bridging hydride disappear. However, the resonance at *ca* -14 ppm broadens at 200 K to disappear at 220 K and reappear at *ca* -3.5 ppm at 240 K. This peak, assigned to $[\text{Cr(CO)}_5(\eta^1\text{-BH}_2\text{=NMe}_2)]$, sharpens at higher temperatures to give a quartet at 300 K ($J_{\text{B-H}} = 90$ Hz). At low temperature, in the slow exchange regime, the resonance observed corresponds to the one of the Cr-H-B hydride. Above 240 K, an average of bridging and free B-Hs gives a peak at -3.5 ppm. Similarly, Ogino and coworkers recently reported the synthesis and characterization of dynamic $\text{NMe}_3\text{-BH}_3$ complexes, $[\text{M(CO)}_5(\eta^1\text{-BH}_3\text{-L})]$ ($\text{M} = \text{Cr}, \text{Mo}, \text{W}$; $\text{L} = \text{NMe}_3$).³

At 290 K, the ^{11}B NMR spectrum shows three main species at 41.2 (t, $J_{\text{BH}} = 130$ Hz), 8.5 (t, $J_{\text{BH}} = 112$ Hz) and -9.5 ppm (q, $J_{\text{BH}} = 95$ Hz) (Figure 3). They correspond to bound $\text{NMe}_2\text{=BH}_2$, $(\text{NMe}_2\text{-BH}_2)_2$ and free NH_3BH_3 respectively. Within hours at -26 °C, the sample decomposes and only the dimer $(\text{NMe}_2\text{-BH}_2)_2$ remains in solution. Addition of more Cr(CO)_6 and 30 minutes of irradiation do not lead to the formation of any new species as observed by ^1H and ^{11}B NMR. These results show that $(\text{NMe}_2\text{-BH}_2)_2$ does not bind to the unsaturated complex $[\text{Cr(CO)}_5]$.

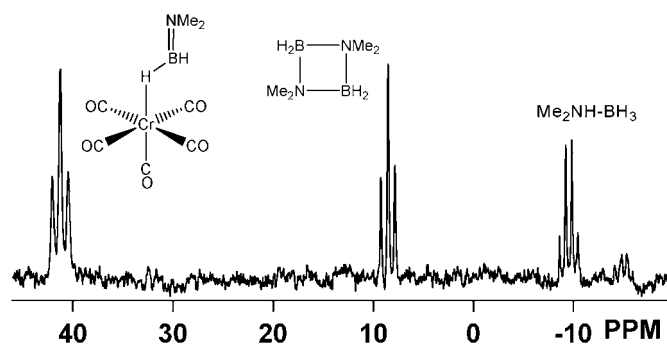


Figure 3. ^{11}B NMR spectra of $[\text{Cr}(\text{CO})_5(\eta^1\text{-BH}_2\text{=NMe}_2)]$ (toluene- d_8 , 499 MHz, 290 K).

Conclusions

We report the coordination of B-N species to group 6 pentacarbonyl transition metal complexes. Formation of the corresponding dihydrogen complex has also been observed after loss of hydrogen due to the dehydrogenation of the aminoborane adduct. Experimental data show that the cyclic dimer $(\text{NMe}_2\text{BH}_2)_2$ does not bind to $[\text{Cr}(\text{CO})_5]$ while $\text{NMe}_2\text{=BH}_2$ does.

Acknowledgement. This research was supported by the Department of Energy. We thank Dr Tom Autrey of PNNL for a generous gift of NH_3BH_3 and Me_2NHBH_3 .

References

- (1) Chen, Y.; Fulton, J.L.; Linehan, J.C.; Autrey, T. *J. Am. Chem. Soc.* **2005**, *127*, 3254-3255 and references therein.
- (2) Matthews, S.L.; Pons, V.; Heinekey, D.M. *J. Am. Chem. Soc.* **2005**, *127*, 850-851.
- (3) Shimoi, M.; Nagai, M.I.; Kawano, Y.; Katoh, K.; Uruichi, M.; Ogino, H. *J. Am. Chem. Soc.* **1999**, *121*, 11704-11712.

ROOM TEMPERATURE HYDROGEN EVOLUTION FROM AMINE-BORANES

Frances H. Stephens and R. Tom Baker

Institute for Hydrogen and Fuel Cell Research
Chemistry Division, MS J514
Los Alamos National Laboratory
Los Alamos, NM 87545

Introduction

Chemical hydrides for hydrogen storage are being explored as alternatives to high pressure tanks (gas or liquid), adsorbed hydrogen, and metal hydride fuels. Chemical hydrides have the potential to be non-pyrophoric, non-hazardous, solid or slurried fuels for automotive applications where hydrogen is generated under controlled conditions on-board, on demand, and the spent fuel is regenerated off-board.

Ammonia-borane (H_3NBH_3) epitomizes an important characteristic required for a chemical hydride used in hydrogen storage: Low molecular weight vis-à-vis the number of hydrogen atoms present. The ideal molecular hydrogen storage capacity of H_3NBH_3 is 19.6 wt% (c.f. the DOE's goal of 6 wt% system storage by 2010). Because the molecule contains both hydridic and protic hydrogen atoms, it loses H_2 at temperatures above ca. 80 °C. Thermal decomposition in solution initially affords the cyclic oligomers borazane ($\text{B}_3\text{N}_3\text{H}_{12}$) and borazine ($\text{B}_3\text{N}_3\text{H}_6$).¹ Wideman and Sneddon demonstrated that large scale preparation of borazine from H_3NBH_3 could be achieved in high yield over 3 h by simply heating a tetraglyme solution of ammonia-borane.² Sneddon et al. also demonstrated that borazine could be thermally cross-linked at temperatures as low as 70 °C with concomitant H_2 evolution.³ Ultimately H_3NBH_3 can be dehydrogenated completely, forming ceramic BN, but temperatures in excess of 500 °C are required.⁴

It is possible to obtain a large amount of hydrogen from H_3NBH_3 , but low energy (i.e. minimal heat input) methods to utilize this fuel are only just being developed. Manners et al. have recently reported room temperature liberation of H_2 from H_3NBH_3 or dimethylamine-borane (HMe_2NBH_3) by addition of late metal catalysts. For example, select Rh(I) species catalyzed the dehydrocoupling of HMe_2NBH_3 , forming H_2 and the cyclic dimer $[\text{BH}_2\text{NMe}_2]_2$ as well as linear aminoborane polymers.⁵ The active catalytic species in this reaction was recently proposed to be a soluble Rh_6 cluster by a team at Pacific Northwest National Laboratory.⁶ This research team also reported the use of mesoporous scaffolds to template the thermal H_3NBH_3 dehydrogenation. No borazine was observed during the reaction, and the authors suggested exclusive formation of linear polymers. This selectivity is important, since volatile products of dehydrogenation may negatively affect fuel cell catalysts used in series with a hydrogen storage material. Furthermore, preliminary thermodynamic calculations indicate that sequential dehydrogenations to form linear polymers $(\text{NH}_2\text{BH}_2)_x$ and $(\text{NHBH})_x$ are thermoneutral to within 40 kJ mol⁻¹.⁷

In this communication we report the evolution of hydrogen from ammonia-borane catalyzed by a series of proprietary, non-metal catalysts.

Experimental

General Considerations. Chemicals were used as received. Dimethoxyethane was distilled from CaH_2 and stored over 4 Å molecular sieves. Toluene was dried by the method of Grubbs.⁸ Ammonia-borane was prepared via literature methods. All experiments were performed in an inert atmosphere using standard glovebox or Schlenk line techniques.

Characterization Methods. ¹¹B NMR spectra were recorded on a Bruker 400 MHz spectrometer and were externally referenced to boron trifluoride etherate (0 ppm).

Dehydrogenation Reactions. In a typical reaction, 0.1 mmol amine-borane was dissolved in approximately 0.5 mL dimethoxyethane (H_3NBH_3) or toluene (HMe_2NBH_3). To this solution was added a solution of 0.1 equiv catalyst at 22 °C. The reaction mixture was placed in an NMR tube with a Teflon stopcock, and the headspace was evacuated to allow for H_2 (g) generation during the reaction. The reaction was then monitored by ¹¹B NMR spectroscopy.

Results and Discussion

For comparison purposes, a thermolysis study was performed in which a dimethoxyethane solution of H_3NBH_3 (ca. 0.4 M) was monitored at 80 °C over 24 h using ¹¹B NMR. After 2 h, in addition to the starting material (δ -22 (q) ppm), a small amount of borazane was observed (δ -10 (t) ppm), subsequently losing hydrogen slowly to form borazine (δ 32 (d) ppm) after 24 h. At this temperature, starting material remained after 24 h.

In contrast, the addition of 10 mol% of proprietary, non-metal catalysts to H_3NBH_3 resulted in complete consumption of the starting material after the same time period and heating regimen. The product mixture included small amounts of the soluble products borazine and borazane and a significant amount of insoluble colorless solid (characteristic of polymeric aminoboranes). In addition to borazine and borazane, a triplet at ca. δ -25 ppm was observed, consistent with internal $-\text{BH}_2-$ units in linear oligomers of aminoborane. (Experiments utilizing ²H- and ¹⁵N-labeled substrates are underway.) The observed production of small amounts of borazine and borazane is likely due to the addition of heat to a reaction mixture containing H_3NBH_3 ; the thermal decomposition of H_3NBH_3 and the catalyzed reactions are competitive at 80 °C.

The proprietary, non-metal catalysts also react with H_3NBH_3 under mild conditions to yield hydrogen. In this case, immediate and copious bubbling ensued when 0.1 equiv catalyst was added at 22 °C. While the ¹¹B NMR spectrum is complex in the region from -15 to 10 ppm, it is clear that a triplet at approximately δ -25 ppm grows in over 24 h *at room temperature*. This is consistent with internal $-\text{BH}_2-$ units in an aminoborane oligomer.

The reaction of the catalyst with the alkyl-substituted dimethyl amine-borane (HMe_2NBH_3) resulted in oligomerization. When 0.1 equiv of the catalyst was used, no peaks attributable to the cyclic dimer $[\text{Me}_2\text{NBH}_2]_2$ were observed in the ¹¹B NMR spectrum, in contrast to metal-catalyzed reactions.^{5,6} A triplet of doublets around δ -20 ppm grows in over time, eventually becoming the major peak. Again, this upfield peak is due to the internal $-\text{BH}_2-$ units in an oligomeric product.

Conclusions

In contrast to transition metal catalysts, it can be concluded that these proprietary, non-metal catalysts increase the selectivity for linear oligomers. This discovery moves amine-boranes closer to commercialization as H_2 generating materials for portable power sources. Further experiments, including H_2 quantification, are underway to refine these experiments.

Acknowledgement. This work was performed in conjunction with the Chemical Hydrogen Storage Center of Excellence, supported by the Hydrogen, Fuel Cell, and Infrastructure Technologies Program of the Division of Energy Efficiency and Renewable Energy, U.S. Department of Energy, under contract DEPS-3603-G093013.

References

- (1) Wang, J. S.; Geanangel, J. S. *Inorg. Chim. Acta* **1988**, *148*, 185.
- (2) Wideman, T.; Sneddon, L. G. *Inorg. Chem.* **1995**, *34*, 1002.
- (3) Fazen, P. J.; Beck, J. S.; Lynch, A. T.; Remsen, E. E.; Sneddon, L. G. *Chem. Mater.* **1990**, *2*, 96.
- (4) Paine, R. T.; Narula, C. K. *Chem. Rev.* **1990**, *90*, 73.
- (5) Jaska, C. A.; Temple, K.; Lough, A. J.; Manners, I. *J. Am. Chem. Soc.* **2003**, *125*, 9424.
- (6) Chen, Y.; Fulton, J. L.; Linehan, J. C.; Autrey, T. *J. Am. Chem. Soc.* **2005**, *127*, 3254.
- (7) Gutowska, A. et al. *Angew. Chem. Int. Ed.* **2005**, *44*, 2.
- (8) Pangborn, A. B.; Giardello, M. A.; Grubbs, R. H.; Rosen, R. K.; Timmers, F. J. *Organometallics* **1996**, *15*, 1518.

CATALYSIS FOR HYDROGEN STORAGE

John C. Linehan¹, Tom Autrey¹, John L. Fulton¹, Yongsheng Chen¹
and Mahalingam Balasubramanian²

(1) Fundamental Science Division, Pacific Northwest National Laboratory, P. O. Box 999 MSIN K2-57, Richland, WA 99352, Fax: 509-375-6660, john.linehan@pnl.gov (2) Advanced Photon Source, Argonne National Laboratory

Introduction

The U.S. Department of Energy has recently issued a Grand Challenge in Hydrogen Storage.¹ The ambitious goals of this challenge demand the discovery of new hydrogen storage materials and new catalysts for H₂ release as well as regeneration. We have embarked upon a study of amine borane complexes to meet this challenge.² In previous work we examined the rhodium catalyzed dehydrocoupling of dimethylamine borane to release hydrogen at room temperature from this storage material. Below we describe a new aspect of our research on the hydrogen release from NH₃BH₃ using a homogeneous ruthenium catalyst. Other groups have investigated the ruthenium catalyzed dehydrocoupling of phorous boron bonds with concomit formation of hydrogen.⁴

Experimental

Methanol and tetrahydrofuran were purified and degassed before use. Borane ammonia complex was purchased from Aviaor and used as received. In situ ¹¹B NMR was performed on a Varian VXR-300 run unlocked in non-deuterated solvent referenced to BF₃·etherate as 0 ppm. The *in situ* Ru K-edge (22117 eV) XAFS spectra were collected on the bending magnet beamline (PNC-CAT, Sector 20) at the Advanced Photon Source, Argonne National Laboratory. Data were analyzed using AUTOBK and IFEFFIT routines.³

The reactions described here release large quantities of H₂ gas. The reactions can be exothermic and the gas release can be violent. Proper safety precautions including, but not limited to, pressure release devices, proper venting and personal safety equipment should be used.

Results and Discussion

The boron NMR results of the ruthenium (Ru(DMSO)₄Cl₂, DMSO is dimethylsulfoxide) catalyzed reaction of NH₃BH₃ in methanol at room temperature are shown in Figure 1. The boron cleanly and quickly converts from BH₃ attached to NH₃ to methylborate. The proton coupled boron NMR spectra of this reaction clearly shows that product peak contains no B-H bonds. Methyl borate forms very slowly at room temperature in methanol from NH₃BH₃ in the absence of a catalyst. At 80°C the non-catalyzed reaction occurs on a similar time-scale as the catalyzed reaction at room temperature.

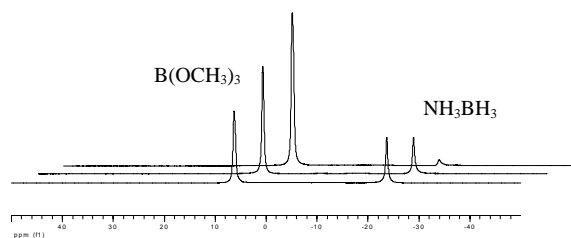


Figure 1. The ¹¹B{¹H} NMR of the reaction of NH₃BH₃ with methanol catalyzed with Ru(DMSO)₄Cl₂ at room temperature. The time evolution from front to back is 6 minutes, 11 minutes and 44 minutes after mixing.

The ruthenium edge EXAFS radial distribution functions of the ruthenium species relevant to this reaction are shown in Figure 2. These and the *in situ* EXAFS data (not shown) demonstrate that during the catalysis the Ru(DMSO)₄Cl₂ complex is completely converted to a new soluble catalytic species which does not contain any Ru-S or Ru-Cl bonds. The metal-containing catalytic species (or its resting state) only has light element (O, B, or N) ligands directly bound to the ruthenium.

XANES data (not shown) demonstrate that the initial Ru(II) oxidation state stays as Ru(II) throughout the reaction. There is no obvious precipitate and no obvious oxidation change during the reaction.

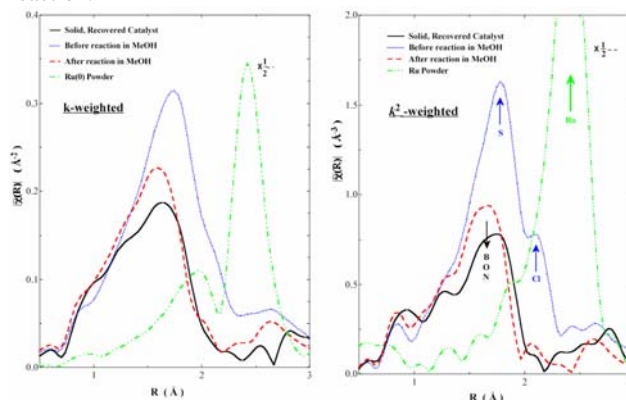


Figure 2. Radial distribution plots of ruthenium before and after reaction with NH₃BH₃ in methanol compared with ruthenium metal and the initial starting complex, Ru(DMSO)₄Cl₂.

Conclusions

In situ spectroscopies have been shown to be extremely useful in determining the reaction profiles of both the substrates and the catalysts during the reaction to release H₂ from hydrogen storage materials. While the structure of the ruthenium catalyst is unknown we know that the ligand field about the catalyst is completely changed during catalysis but the oxidation state remains +2. The boron-containing reaction products are dependent upon the solvent and the reaction conditions. Efficient release of H₂ from NH₃BH₃ has been demonstrated.

Acknowledgement. Work was supported by the Laboratory Directed Research and Development Program at the Pacific Northwest National Laboratory; the NS&T Initiative; and by the Department of Energy's Center of Excellence in Chemical Hydrogen Storage. Pacific Northwest is operated for the Department of Energy by Battelle. Use of the Advanced Photon Source was supported by the U.S. Department of Energy, Office of Science, Office of Basic Energy Sciences, under Contract No. W-31-109-ENG-38.

References

- (1) Hydrogen, Fuel Cells & Infrastructure Technologies Program, 2003 Merit Review and Peer Evaluation Meeting, May 19-22, 2003, Berkeley, CA.
- (2) Chen, Y. S.; Fulton, J. L.; Linehan, J. C. and Autrey, S.T. *J. Am. Chem. Soc.*, **2005**, *127*, 3254.
- (3) Newville, M. *J. Synchrotron Rad.* **2001**, *8*, 322.
- (4) Dorn, H., Singh, R. A., Massey, J. A., Nelson, J. M., Jaska, C. A., Lough, A. J. Manners, I. *J. Am. Chem. Soc.* **2000**, *122*, 6669.

SPECTROSCOPIC STUDIES OF HYDROGEN FORMATION FROM AMINEBORANE COMPLEXES

Nancy Hess, Craig Brown, Luke Daemen, Eugene Mamontov, R. Scott Smith, Bruce D. Kay, Wendy Shaw, John Linehan, Benjamin Schmid, Ashley Stowe, Maciej Gutowski & Tom Autrey

Pacific Northwest National Laboratory
Los Alamos National Laboratory
National Institute of Standards
The University of Maryland
University of Oregon

Introduction

Currently there is great scientific and public interest in the challenges facing the conversion from a petroleum based energy economy to one based upon hydrogen as an energy carrier for fuel cell power applications.^{1,2} The future of the Hydrogen Economy will depend upon significant scientific and engineering advances in hydrogen storage, hydrogen production and hydrogen utilization (fuel cells).³⁻⁶

We have been investigating the chemical and physical properties of chemical hydrogen storage materials containing boron and nitrogen as potential solid state hydrogen storage materials for on-board applications. Experimentally, we have focused on our efforts on determining the thermochemistry and kinetics of thermally activated release of hydrogen from ammonia borane (NH_3BH_3) confined within mesoporous silica and the catalytically activated release of hydrogen from dimethylamine borane (Me_2NHBH_3). We discovered that ammonia borane (AB) confined within the channels of mesoporous silica (SBA-15 or MCM-41) showed a significant rate enhancement for hydrogen release and a change in the enthalpy of reaction for the release of hydrogen.⁷ These results are summarized in Figure 1, (A) shows the decomposition of bulk AB to yield polyaminoborane (PAB), the activation barrier, E_a 28 kcal/mol, and enthalpy of reaction, ΔH_{rxn} -5 kcal/mol for loss of hydrogen in the solid state. (B) shows the decomposition of AB confined in SBA-15, E_a ca. 12 kcal/mol and ΔH_{rxn} -0.3 kcal/mol for loss of hydrogen. The observed change in thermochemistry and kinetics (ΔH_{rxn} and E_a) reflects a change in the chemical or physical properties of AB when it is confined within the nano-dimensional channels of SBA-15.

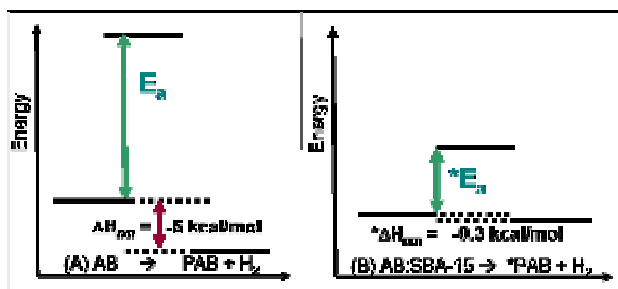


Figure 1. Energy level diagram comparison of E_a and enthalpy for H_2 formation from bulk AB and AB confined in SBA-15.

Recent mechanistic studies using deuterium labeling lead us to conclude that the formation of hydrogen from bulk AB occurs by a bimolecular pathway⁸ contrary to what has been suggested in the literature.⁹⁻¹¹ This was also in contrast to our in-situ spectroscopic studies of the catalyzed dehydrogenation of dimethylamine borane where the hydrogen formation appeared to proceed by an intramolecular pathway.¹² Thus, while we have learned much about

hydrogen formation from these solid state hydrogen storage materials one important question remains unanswered: What is the origin of the change in the activation barrier and enthalpy of reaction for hydrogen loss from AB in the mesoporous scaffold compared to the reaction in the bulk material? In this presentation we will highlight our recent spectroscopic studies aimed at elucidating the changes in the chemical and physical properties of AB in mesoporous silica.

Experimental

Ammonia borane from Aldrich (95%) was recrystallized from diethyl ether. Ammonia borane (99%) from Avibor and used as received. The synthesis and loading of the AB into the mesoporous silica has been described previously.

¹¹Boron and ¹H NMR Spectroscopy. Amino borane samples were run on a Varian Unity Inova spectrometer operating at 800 MHz ¹H frequency, with a 4mm, 3-Ch Doty MAS probe. The Bloch decay experiment utilized a 200 kHz sweep width, a 8 μs ¹¹B 90° pulse, with and without ~30 kHz decoupling, 16-64 scans and a pulse delay of 5 seconds. ¹¹B spectra were referenced to $\text{BF}_3\text{CH}_3\text{OH}$ (-0.9 ppm). The ¹H spectra utilized a 3 μs 90° pulse and were referenced to H_2O (4.8ppm), with 4 scans and a 10 second pulse delay. Samples were spun at 15 kHz, cooled to 10-20 °C and 128 scans were collected for each spectrum.

Raman Spectroscopy. Raman spectra were excited by 10mW of continuous wave, doubled diode YAG laser with output at 532 nm and collected on a Dilor XY 800 mm triple spectrometer with liquid nitrogen cooled charged couple device (CCD) detector with a spectral resolution of ca. 0.2 cm^{-1} at 500 nm. A confocal microscope with 50X objective with high numerical aperture was used to image the bulk and confined AB samples.

Quasi-elastic Neutron Spectroscopy. The Disk Chopper Spectrometer (DCS) and the High Flux Backscattering Spectrometer (HFBS) at the NIST Center for Neutron Research¹³ was used to study the bulk and confined ammonia borane. Isotopically enriched ¹¹B samples were loaded into annular aluminum cells and cooled in a closed cycle refrigerator. On DCS, data were collected at a series of temperatures above the structural phase transition at 225 C to extract activation energies for proton motion. Use of an incident wavelength of 3.6 Å results in an instrumental resolution of ~0.3 meV at the elastic line. On HFBS, data were collected at several temperatures below 225 C to extract information on proton motions at higher resolution (1.2 μeV). By using both spectrometers, we can follow fast proton motions that occur on picosecond time scale on DCS to slower motions on the nanosecond time scale on HFBS.

Results and Discussion

In previous work we discovered the barrier for hydrogen release from ammonia borane embedded in mesoporous silica is significantly lower than the barrier for hydrogen release from bulk AB. The origin of this beneficial rate enhancement was surprising and not fully understood. Furthermore, solid state ¹¹B NMR results suggested the non-volatile products formed upon release of hydrogen were different than observed in the bulk material resulting in a change in the reaction enthalpy for hydrogen formation. There are two distinct possibilities that may lead to the observed changes, (1) changes in the physical properties such as an increase in defects sites that may be responsible for the nucleation or an increase in disorder of the extended hydrogen bonding network of the molecular crystal, ammonia borane, and (2) changes in the chemical properties such as interfacial interactions that catalyze the formation of hydrogen from the molecular crystal AB, e.g. the acidic nature of the interface catalyzing the nucleation event..

Raman spectroscopy can be used to monitor changes in the B-N, B-H and N-H stretching and bending frequencies and line shapes between bulk AB and AB confined within the mesoporous materials or deposited on metal oxide interfaces. Initial work has shown that AB associated with SBA-15 or MCM-41 results in an increase in the B-N symmetric stretch line width and the possible appearance of a lower frequency B-N stretch mode while the B-H and N-H stretching moieties show little change (Figure 2). These results suggest that there is a greater distribution of energetically distinct B-N entities when AB is associated with the interface and may reflect the importance of an $-\text{SiOSi}$ bridge with B-N (e.g., O^-B). The polymerization reaction of AB can also be followed using in situ Raman spectroscopy. IR may be able to provide insight into the interaction between B-H or N-H bonds with SiO-H and Si-O-Si groups of the mesoporous silica. Many different electrostatic interactions ($\text{SiO-H}-\text{HBH}_2\text{NH}_3$, N-H or B may also coordinate to O in Si-O-Si) can be envisioned and spectroscopic approaches will facilitate their interpretation. The same changes will be calculated at the DFT and SCC-DF TB levels to assist in interpretation of the experimental results.

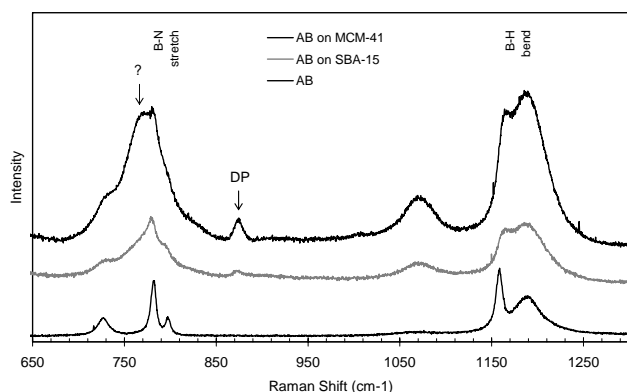


Figure 2. Raman vibrational spectra of bulk AB and AB confined in mesoporous MCM-41 and SBA-15. The B-N, B-H and N-H stretching and bending vibrations or AB occur in distinct energy regions of the vibrational spectrum. The B-N stretching mode at ca. 780 cm^{-1} and the B-H and the N-H rocking modes at ca. 1060 cm^{-1} appear most affected by the confinement in the mesoporous silica substrates. DP indicates the vibrational signature of possible decomposition products.

NMR Spectroscopy can be used to identify new species and/or changing environments. Qualitatively, the ^1H NMR shown here suggests a change in the environment when AB is deposited on a scaffold, based on the significant narrowing of the resonances. This is consistent with several interpretations, including an increase in the mobility or an increase in the crystallinity of AB in the scaffold. Further NMR studies, as well as other spectroscopic characterization will be necessary to fully understand these initial observations.

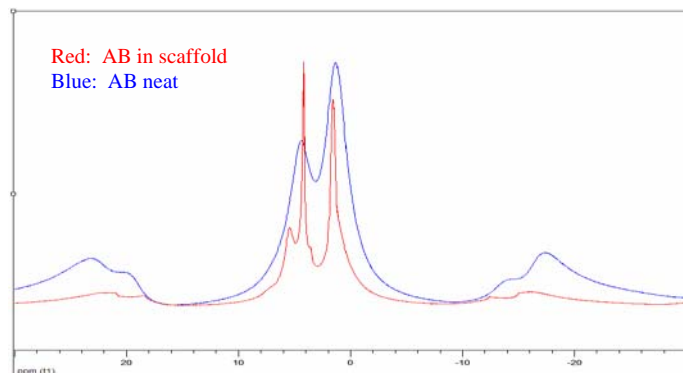


Figure 3. 800 MHz ^1H NMR of AB bulk (blue) and in the SBA scaffold (red). Confinement of AB results in significantly sharper lines, possibly due to an increased uniformity, or an increased mobility of the AB in the scaffold.

Quasi-elastic Neutron Spectroscopy can be used to probe the nano to picosecond timescales and sub-nanometer lengthscales of proton motion in materials. In general, the dependence of the ratio of the quasi-elastic scattering intensity to the total intensity on the momentum transfer provides information on the geometry and lengthscale of the individual proton motions. The timescale is extracted from the quasielastic peak widths. Results from both HFBS and DCS indicate that the deposition of AB on MCM-41 results in longer proton residence times and lower energy barriers for proton motion compared to bulk AB. The reduced activation energy for proton motions may partly explain the improved thermolysis and lowering the activation barrier for the loss of the first equivalent of H_2 . In addition, the phonon density of states for neat AB compares well with other spectroscopic results, with the intense peak at 22 meV assigned to the librational NH_3 and BH_3 modes, whereas AB on MCM-41 displays a broad, featureless spectrum indicating a poorly crystalline material (Fig. 4). Clearly, deposition of AB on MCM-41 profoundly impacts the crystallinity and proton motions in AB.

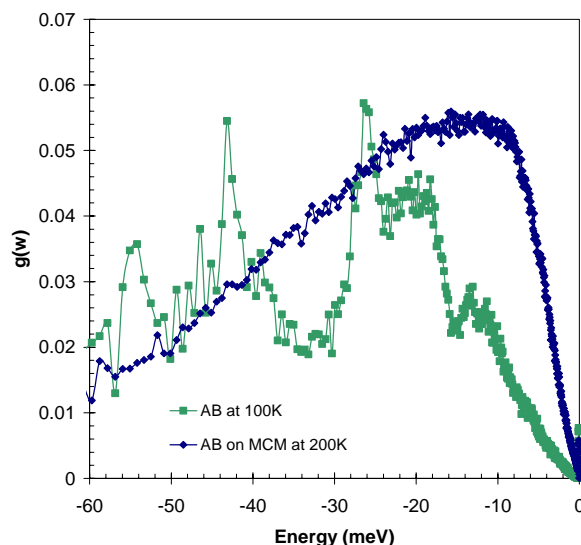


Figure 4. Phonon density of states for bulk AB and AB confined in MCM-41.

Conclusions

We have begun to combine multiple, complimentary spectroscopic tools to study the interfacial interactions between mesoporous silica scaffolds and ammonia borane. These experimental approaches combined with our theoretical efforts will provide information about the changes in the chemical and physical properties of AB at the interface.

Acknowledgement. The authors wish to acknowledge support from the Laboratory Directed Research and Development Program at the PNNL and the Nano Science and Technology Initiative. This research was performed in part using the Interfacial and Nano Science facility in the William R. Wiley Environmental Molecular Sciences Laboratory, a national scientific user facility sponsored by the U.S. Department of Energy's Office of Biological and Environmental Research and located at the Pacific Northwest National Laboratory. Pacific Northwest is operated for the Department of Energy by Battelle. We acknowledge the support of the National Institute of Standards and Technology, U.S. Department of Commerce, in providing the neutron research facilities used in this work. This work also utilized HFBS and DCS which are NIST facilities supported in part by the National Science Foundation under Agreement No. DMR-0086210. This work will continue in part

through the DOE Center of Excellence in Chemical Hydrogen Storage.

References

- ¹ Presidential State of the Union Address 2003. <http://www.whitehouse.gov/news/releases/2003/02/20030206-2.html>
- ² Scientific American, 2004, *Questions about a Hydrogen Economy*.
- ³ National Academy of Engineering, 2004, *The Hydrogen Economy: Opportunities, Costs, Barriers, and R&D Needs*.
- ⁴ Office of Science at the US Department of Energy. 2004, *Basic Research Needs for the Hydrogen Economy*.
- ⁵ American Physical Society, 2004, *The Hydrogen Initiative*.
- ⁶ http://www.eere.energy.gov/vehiclesandfuels/program_areas/freedomcar/index.shtml
- ⁷ Anna Gutowska, Liyu Li, Yongsoon Shin, Chongmin M. Wang, Xiaohong S. Li, John C. Linehan, R. Scott Smith, Bruce D. Kay, Benjamin Schmid, Wendy Shaw, Maciej Gutowski, and Tom Autrey. *Nano-Scaffold Mediates Hydrogen Release and Reactivity of Ammonia Borane*. Angew. Chemie International Ed. **2005**, in press.
- ⁸ R. Scott Smith, Bruce D. Kay, Liyu Li, Nancy Hess, Maciej Gutowski, Benjamin Schmid & Tom Autrey. *Mechanistic studies of hydrogen formation from amineborane complexes*. Prepr. Pap. –Am. Chem. Soc. Div. Fuel Chem. **2005**, 50, 112.
- ⁹ R. Komm, R. A. Geanangel, R. Liepins, *Inorg. Chem.* **1983**, 22, 1684.
- ¹⁰ V. Sit, R. A. Geanangel, W. W. Wendlandt, *Thermochim. Acta* **1987**, 113, 379.
- ¹¹ D. -P. Kim, K. -T. Moon, J. -G. Kho, J. Economy, C. Gervais, F. Babonneau *Poly. Adv. Tech.* **1999**, 10, 702.
- ¹² Yongsheng Chen, John L. Fulton, John C. Linehan and Tom Autrey, *In-situ XAFS and NMR Study of Rhodium Catalyzed Dehydrogenation of Dimethylamine Borane*. J. Am. Chem. Soc. **2005**, 127, 3254.
- ¹³ J.R.D. Copley and J.C. Cook, *Chem. Phys.* **2003**, 292, 477.

HYDROGEN EVOLUTION FROM ORGANIC “HYDRIDES”

Daniel E. Schwarz, Thomas M. Cameron, P.
Jeffrey Hay, Brian L. Scott, William Tumas,
David L. Thorn

Chemistry Division
MS J514, Los Alamos National Laboratory
Los Alamos, New Mexico 87544

Introduction

New concepts of hydrogen storage are being explored for applications from portable power to transportation for the future “hydrogen economy”.¹⁻³ The advantages of chemical hydrogen storage are the deliberate control of the thermochemistry, kinetics, and mass density for incorporating and releasing hydrogen. We are currently exploring an uncommon chemical process, the exergonic evolution of hydrogen gas at room temperature via catalysis from reduced organic compounds.

Experimental

2-(1,3-dimethylbenzimidazoline-2-yl)benzoic acid (**1**)⁴, 1,3-dimethyl-2-phenylbenzimidazoline (**3**)⁵, and 1,3-dimethylbenzimidazolium (**5**)⁶ were all synthesized according to literature methods. The powder diffraction data were collected at room temperature on a Scintag XDS2000 diffractometer equipped with an air-tight environmental chamber to prevent sample degradation.

Catalytic dehydrogenation of **1**: The following is for a typical heterogeneous reaction for **1**, **3**, and **5** (**3** and **5** require the addition of a proton source such as acetic acid). To 0.5 mL of CD₃CN solution of compound **1** (19 mg, 0.07 mmol) in a 20 ml vial was added an acetonitrile solution of Pd(O₂CCF₃)₂ (1 mg, 0.003 mmol). Upon mixing a black precipitate formed and effervescence was observed. The reaction mixture was then transferred to an NMR tube for analysis. Conversion of **1** to **2** was confirmed by ¹H NMR spectroscopy. 2-(1,3-dimethylbenzimidazolium-2-yl)benzoate (**2**) was crystallized from a concentrated CH₃CN solution at -20° C. The black precipitate has a powder XRD pattern consistent with finely-divided palladium metal.

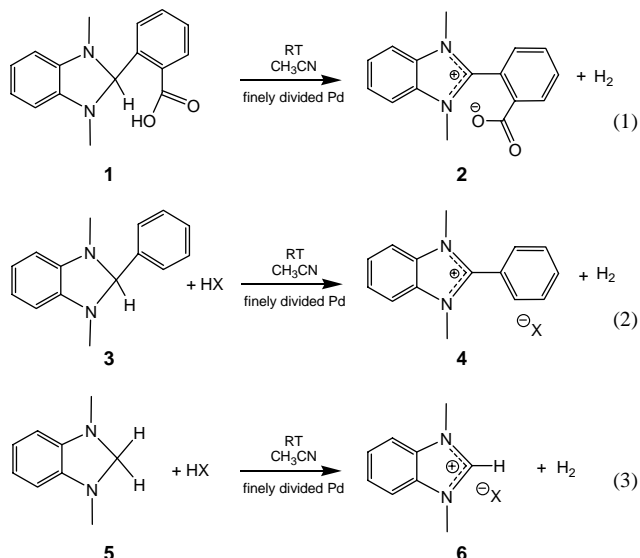
Catalytic dehydrogenation of **5**: For a homogenous system, using RhCl(PPh₃)₃ as the catalyst, a typical reaction is as follows: To 0.7 mL of CD₃CN in an NMR tube was added 15 mg (0.10 mmol) of **5** and 60 mg (1.0 mmol) of acetic acid (97% grade). This solution was mixed then 0.3 mg (0.37 μmol) of RhCl(PPh₃)₃ was added. The NMR tube was heated at 70° C for 1 hour. A 43% conversion of **5** to **6** (+ H₂, ¹H NMR 4.5 ppm) was confirmed by ¹H NMR spectroscopy.

Results and Discussion

Hydrogen elimination from compound **1** comprises the catalyzed reaction between the “hydride” from the unique C-H of the imidazolidine and a “proton” from the carboxyl group (eq 1). This reactivity was confirmed by the reaction of 1,3-dimethyl-2-phenylbenzimidazoline (**3**) with acetic acid or benzoic acid under an inert atmosphere in the presence of finely divided palladium to afford hydrogen (eq 2) and the phenylbenzimidazolium cation (**4**). Compound **3** is stable toward these acids for days when no catalyst is present.

We sought to reduce the molecular weight of the organic hydride donor and thus prepared 1,3-dimethylbenzimidazoline (**5**). Compound **5** evolves hydrogen in the presence of acetic or benzoic acid and catalyst, similar to **3** (eq 3). The product 1,3-

dimethylbenzimidazolium cation (**6**) can be re-converted to **5** with KBH₄.⁶ Along with the heterogeneous catalysts used for **1** and **2**, Wilkinson’s catalyst, RhCl(PPh₃)₃, is a functional homogeneous catalyst (or catalyst precursor) for this system (eq 3). We have measured a mean TOF of 117/hour at 70° C.⁷ Compound **5** is slightly unstable at elevated temperatures over the course of days in the presence of acid when no hydrogen-evolving catalyst is present, involving what we believe are intermolecular disproportionation reactions.⁶



So far, we have not been able to reverse the hydrogen evolution in eq 1, 2, or 3 using Pd or RhCl(PPh₃)₃ catalyst nor have we been able to determine the equilibrium pressure of hydrogen. However, we have observed the following: the reaction in eq 1 progresses to completion even under 3.5 atmospheres H₂ pressure; preliminary *ab initio* calculations on the ambient-temperature transformation of **1** to **2** (eq 1) predict a strongly exergonic reaction; and the reaction of eq 3 generates heat which means that both entropy and enthalpy drive this reaction. These observations suggest that ambient-temperature hydrogen formation from benzimidazolidines and carboxylic acids is strongly favored ($\Delta G \ll 0$) and that using hydrogen pressure alone to drive the reaction backwards will be extremely difficult.⁸ It stands to reason that acids much weaker than carboxylic acids could lead to hydrogen formation in eq 2 and 3, and preliminary results from our laboratory confirm that water is sufficiently acidic for Pd-catalyzed hydrogen evolution from compounds **3** and **5**. However, in the presence of water the reactions are far more complex than the reactions involving carboxylic acids due to further reactions of water and hydroxide with the benzimidazolium cations **4** and **6**. The organic products of the aqueous reactions are still under investigation.⁹

Conclusions

These “organic hydride” systems are sources of hydrolytically releasable hydrogen, reminiscent of inorganic hydrides such as NaBH₄ and LiH. However, by fine-tuning these organic systems for thermodynamically reversible hydrogen release we hope to enable more facile and efficient storage and regeneration than is possible for inorganic hydrides. We recognize that in addition to thermodynamic efficiency, the density of hydrogen storage is also a very important metric for hydrogen storage, and that organic frameworks with less substitution than compounds **1**, **3**, or even **5** are greatly preferred. A major emphasis of our ongoing research is realizing such higher-

density storage while maintaining favorable thermochemical and kinetic parameters for hydrogen evolution. Future work will also include detailed mechanistic studies and the development of more active heterogeneous and homogeneous catalysts for this process.

Acknowledgement. This work was supported as part of the DOE Center of Excellence for Chemical Hydrogen Storage through the Office of Energy Efficiency and Renewable Energy National Hydrogen Storage Project.

References

1. Fakioğlu, E.; Yürüm, Y.; Veziroğlu, T. N. *Int. J. Hydrogen Energy* **2004**, *29*, 1371-1376.
2. Seayad, A. M.; Antonelli, D. M. *Adv. Mater.* **2004**, *16*, 765-777.
3. Zuttel, A. *Naturwissenschaften* **2004**, *91*, 157-172.
4. Brunet, P.; Wuest, J. D. *Can. J. Chem.* **1996**, *74*, 689-696.
5. Reddy, A. P. R.; Veeranaiaiah, V.; Ratnam, C. V. *Indian J. Chem., Sect. B: Org. Chem. Incl. Med. Chem.* **1985**, *24*, 367-371.
6. El'tsov, A. V. *Zh. Obshch. Khim.* **1967**, *3*, 199-204.
7. 0.2 M **5** in CD₃CN, 10x acetic acid, closed NMR tube.
8. **5** can be formed from **6** and water by disproportionation reactions not involving molecular H₂: Konstantinchenko, A. A.; Morkovnik, A. S.; Pozharskii, A. F.; Tertov, B. A. *Khim. Geterotsikl. Soedin.* **1985**, *12*, 1694-1695. Thus proof of the reverse of any of the reactions of eq 1-3 requires more than observing the appearance of benzimidazolidine.
9. Bourson, J. *Bull. Soc. Chim. Fr.* **1971**, 152-159.

X-RAY DIFFRACTION AND H-STORAGE IN ULTRA-SMALL PALLADIUM PARTICLES

D.G. Narehood^a, H.Goto^b, S. Kishore^c, J.H. Adair^d, J.A. Nelson^d,
P.E. Sokol^e, and P.C. Eklund^{a,d}

^aDepartment of Physics

^dMaterials Research Institute and Department of Materials Science
and Engineering
Penn State University
University Park, PA 16802 USA

^bHonda Fundamental Research Laboratories
Tokyo, Japan

^cCenter for Magnetic Recording
UC San Diego
Lajolla, CA 92093 USA

^eIndiana University Cyclotron Facility
Indiana University
Bloomington, IN 47408 USA

Introduction

Although Palladium has been widely investigated for its H uptake and kinetics, there exist a great deal of current interest in the system. This interest stems from the extensive amount of information available on the system, which makes it an excellent test case in which to study the changes in properties of the hydride that can occur as the metal particle size is reduced to the nanometer scale.

Reduction in the grain size of a metal has been recognized to lead to significant differences in its hydrogen uptake characteristics. Specifically of interest are the more favorable kinetics and/or enhanced H-storage that may possibly occur in very small diameter metal nanoparticles. In this paper we investigate the structural transformations and wt% uptake isotherms of very small, carbon-protected Pd nanoparticles (nano-Pd) with average particle diameter ~ 2-3 nm. The nano-Pd data are compared to that from micron-size grained bulk-Pd.

Experimental

Nano-Pd Samples. The two nano-Pd sample investigated in these studies exhibited mean particle sizes of 2.1 nm and 3.1 nm. These particle sizes were determined from the transmission electron microscope (TEM) images and extracted particle size distributions shown in **Figure 1**. Particle sizes of the nano-Pd samples were also determined from the XRD patterns, shown in **Figure 2**, collected with the nano-Pd samples under vacuum and held at a temperature of 50 °C. From the widths of the peaks in the diffraction patterns, the mean particle sizes for the two samples have been estimated to be ~2 and ~ 3nm, which are consistent with the results from the TEM analysis.

Both samples studied possessed a H-permeable carbon coating ~ 1nm thick. This coating has been applied to the nano-Pd to prevent agglomeration and grain growth at the temperatures used to degass and H-load the pristine metallic material. Prior to the x-ray diffraction (XRD) and isotherm measurements, the samples utilized were degassed in vacuum at T=200 °C for several hours. In both studies, ultra-high purity hydrogen gas (99.999%) was utilized.

XRD Measurements. XRD patterns were collected on a Rigaku RU200 rotating anode equipped with an Ag anode. This system was operated at voltages in the range of 40 to 50 kV and currents in the range of 100 to 150 mA. Samples were placed in a high pressure capillary tube cell mounted on a modified powder

diffraction stage with a graphite analyzer between the sample and scintillation detector to eliminate background contributions in the collected patterns caused by fluorescence from the Pd samples. The orientation of the analyzer with respect to the scattered x-ray beam was adjusted such that the scattered K α ($\lambda = 0.56084$ Å) component was selected through Bragg diffraction from the (002) plane of the graphite analyzer. Diffraction patterns were collected over 2 θ ranges of 5 to 45 ° and 10 to 20 ° with a step size of 0.05 ° and time per points of 10 to 20 seconds.

Thermogravimetric Uptake Measurements. Isotherms of the wt% hydrogen uptake versus hydrogen loading pressure, shown in **Figure 4**, were collected for the 3.1 nm sample, with the sample held at temperatures of 50 °C and 90 °C, and the bulk-Pd sample, with the sample held at a temperature of 90 °C. These isotherms were measured gravimetrically on 80 mg of the nano-Pd sample using a high-pressure thermogravimetric analyzer (TGA Model # 003 Hiden, Inc.) The apparent weight of the samples was measured as a function of He and H gas overpressure (P). Before being admitted into the sample chamber, the hydrogen gas was first passed through an oxygen/moisture trap (Megasorb Gas Purifier, Supleco Inc.). The data was corrected for buoyancy effects with the tabulated mass densities of H and He versus (P,T). Diffraction data were collected with the sample held at fixed temperatures of 50 °C, 90 °C, 125 °C, and 150 °C. For each temperature, diffraction patterns were collected for a range of pressures from 0 to 10 atm.

Results and Discussion.

The structure of the nano-Pd samples has been determined from the XRD patterns shown in **Figure 2**. Comparison of the patterns reveals that for every peak present in the diffraction pattern for the bulk-palladium sample, there is a corresponding peak in the pattern for the nano-Pd samples. This correlation between the peaks in nano-Pd patterns with those in the bulk-Pd pattern allows us to confidently conclude that both nano-Pd samples possess the same FCC structure as the bulk. We find no substantial difference in the lattice parameter between the bulk-Pd sample and the nano-Pd samples. Using the positions of the (111) and (220) peaks for the bulk-Pd sample, we find a value for the lattice constant of 3.89 Å, which is in good agreement with the accepted value of 3.8907 Å¹. Again using the (111) and (220) peaks to determine the lattice spacing, we have determined that the 2 nm and 3 nm nano-Pd samples have a lattice constants of 3.90Å, which is essentially in agreement with the accepted bulk-Pd lattice constant.

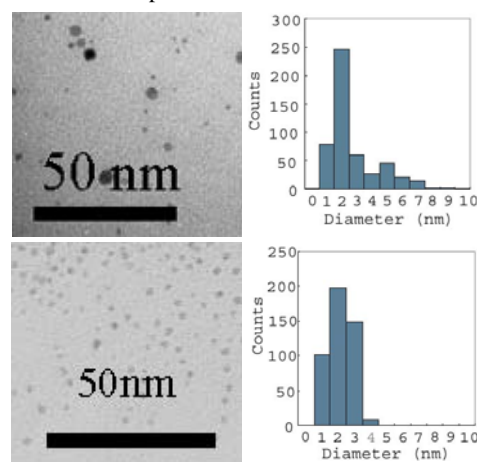


Figure 1. TEM images and extracted for the 3.1 mean diameter sample (upper) and the 2.1 mean diameter sample (lower).

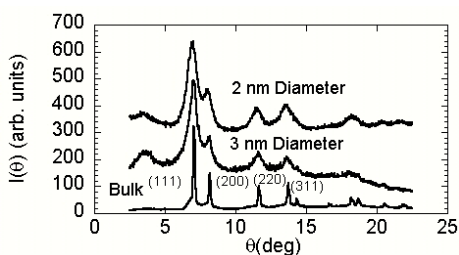


Figure 2. XRD scans collected from the 3 nm Pd sample, 2 nm Pd sample, and bulk Pd sample.

Shown in **Figure 3** are XRD patterns collected with the nano-Pd samples at a temperature of 50 °C in the limits of no hydrogen pressure and high hydrogen pressure. It is clear from a comparison of these patterns that the structure of the metal lattice is still the same, but that a shift in the position of the diffraction peaks to lower scattering angles occurs. Lower scattering angles correspond to larger lattice spacing and this shift is interpreted as the α to β phase transition. The lattice constant in the β phase has been determined to be 4.02 Å, which is consistent with that observed for the bulk-Pd hydride in the β phase.

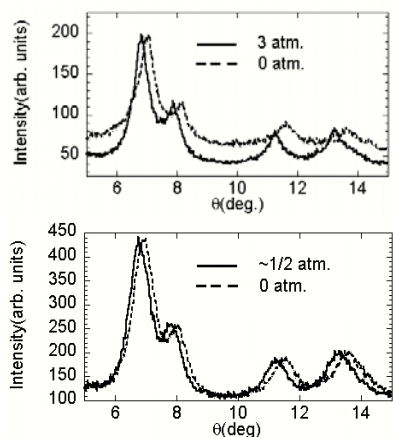


Figure 3. Comparison of the XRD patterns under low and high hydrogen loading pressure for the 3.1 mean diameter sample (upper) and the 2.1 mean diameter sample (lower).

Considerable differences are seen between the isotherm data of the bulk-Pd sample and the 3.1 nm nano-Pd sample, both of which are shown in **Figure 4**. As is easily seen in the isotherms, the bulk-Pd reference sample exhibits a flat plateau, characteristic of the co-existence of the α and β phases, and is in excellent agreement with the literature. This flat plateau is not present in the isotherm for the 3.1 nm Pd sample. Instead, in the region in which phase co-existence should occur and the isotherm should be flat, it exhibits a noticeable positive slope. We have recently reported similar results for unprotected nano-Pd particulates with somewhat larger particle sizes².

Also notable in the isotherm data is the large disparity between the wt % uptake of the bulk reference and our nano-Pd sample. This results predominately from the high percentage of carbon in the nano-Pd sample, which is present as the coating protecting the Pd nano-particles from agglomeration. After corrections for the carbon coating, the wt % of H relative to just the Pd in the sample is ~1 % for $T = 50$ °C at a pressure of ~1 atm. This wt% uptake is larger

than observed in the bulk-Pd sample under the same conditions, which is in agreement with our earlier work². This increase in hydrogen solubility in the α phase is attributed to the occupation of surface and subsurface sites, which occupy a greater percentage of volume in the nano-Pd samples.

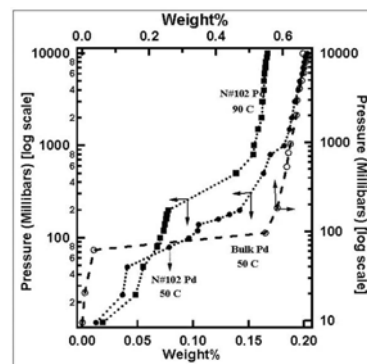


Figure 4. Hydrogen wt% uptake isotherms for both the nano-Pd sample (upper axis), at temperatures of 50 °C and 90 °C, and bulk-Pd (lower axis), for a temperature of 50 °C are shown.

The hydriding behavior of nano-Pd has been previously studied in both theoretical and experimental work. Suleiman et al.³ have performed similar studies to those reported here on Pd clusters with diameters of 6.0 nm and 3.8 nm. In their studies, they find that the 6.0 nm particles possess an FCC structure and still undergo the α to β phase transition, while the 3.8 nm particles do not undergo this transition. In addition, they claim that the structure of the 3.8 nm sample is icosahedral. It is suggested that the lack of a phase transition is related to the icosahedral structure, which is claimed to be favorable for such small particles. Wolf and Lee⁴ have examined the hydriding behavior of nano-Pd clusters that contain on the order of 500 Pd atoms through Monte Carlo simulations. They have also determined that the nano-Pd clusters do not undergo a phase transition. We find no support for either the experimental work or theoretical work. Both samples investigated possess smaller mean diameters and fewer atoms per particle than in previously mentioned work, yet both samples clearly maintain an FCC structure and undergo the α to β phase transition.

Conclusion

We report striking similarities in the hydriding behavior of nano-Pd and bulk-Pd samples. This is despite the incredibly small number of Pd atoms composing the particles. The nano-Pd samples utilized in this work contain on the order of 100 – 300 particles, which not only means that a substantial volume (at least 30%) of the Pd atoms are within one lattice constant of the surface, but also that short-range forces should dominate the Pd-H interactions.

Acknowledgement. This work was supported by the Department of Energy under Grant DE-FC36-05GO15077 and by Honda Research and Development

References

- (1) Rao, C.N.; Rao, K.K.; *Can. J. Phys.*, **1964**, 42, 1336.
- (2) Kishore, S.; Nelson, J.A.; Adair, J.H.; Eklund, P.C.; J. L. *J. Alloys and Compounds* **2005**, 389, 234
- (3) Suleiman, M.; Jisrawi, N.M.; Dankert, O.; Reetz, M.T.; Bähz, C.; Kirchheim, R.; Pundt, R.; Winans, R. E. *J. Alloys and Compounds* **2003**, 356-357, 644
- (4) Wolf, R.J.; Lee, M.W.; *Phys. Rev. Lett.* **1994**, 73 (4), 557.

PREDICTING HYDROGEN DIFFUSION RATES BY ACTIVATED HOPPING AND QUANTUM TUNNELING IN COMPLEX METALLIC STRUCTURES

Bhawna Bhatia*, Preeti Kamakoti*, and David S. Sholl*[#]

*Dept. of Chemical Engineering, Carnegie Mellon University,
Pittsburgh, PA. 15213, USA

[#]National Energy Technology Laboratory, Pittsburgh,
PA 15236, USA

Introduction

The use of metallic materials in hydrogen storage and purification demands not only a significant solubility of hydrogen in these materials but ideally also rapid diffusion by hydrogen in the bulk. In order to develop suitable hydrogen storage materials a detailed knowledge of the microscopic mechanisms of hydrogen motion in these systems is required. Although the diffusion of hydrogen in metals has been studied for decades, methods that can predict the diffusion rates of hydrogen in the complex materials of practical interest are still limited. In the past several years, we have demonstrated how a modeling approach based on deriving lattice models for hydrogen diffusion in disordered metal alloys from Density Functional Theory (DFT) calculations can give accurate predictions of the properties of macroscopic hydrogen purification membranes¹⁻³.

Our previous modeling efforts have focused on descriptions in which hydrogen hopping between adjacent interstitial sites in a metal take place via an activated process that can be described using either classical or quantum corrected transition state theory. An important issue that cannot be addressed by this approach is the contribution to hydrogen transport from quantum mechanical tunneling between adjacent sites. Several approaches exist that allow tunneling in metals or on metal surfaces to be described accurately via DFT calculations⁴⁻⁶. Unfortunately, these methods require very extensive DFT calculations to characterize a single pair of adjacent sites. This greatly limits the application of these methods to complex alloys where H occupies interstitial sites with different types of neighboring atoms and thus large numbers of distinct hopping transition rates must be predicted in order to characterize long range diffusion.

Here, we describe a computational approach that allows tunneling contributions to hydrogen hopping between interstitial sites in complex metals to be readily described using DFT calculations. To examine the validity of this method, we have examined H diffusion in a number of C15 Laves phase intermetallics with composition AB₂. This is a useful test case for our methods because their structure contains a number of distinct interstitial sites which must all be examined before net diffusion can be predicted and because high quality experimental data exists over large temperature ranges for some examples⁷⁻¹². The interstitial sites occupied by hydrogen in C15 AB₂ Laves phase intermetallics are tetrahedral sites formed by two A atoms and two B atoms (g sites), one A atom and three B atoms (e sites), and b sites formed by four B atoms. There are 17 tetrahedral interstitial sites per formula unit, 12 g sites, 4 e sites, and 1 b site for the C15 structure. Below, we show how we have used DFT-based methods to describe the contributions of activated hopping and quantum tunneling to hydrogen diffusion in ZrX₂ (X=V, Cr, Mn, Fe and Co) in the C15 Laves phase structure.

Computational Method

We have performed plane wave DFT calculations to examine H diffusion in ZrX₂, using the Vienna *ab initio* Simulation Package

(VASP)¹³ using the PW91-GGA exchange-correlation functional. Spin polarization was used for ZrMn₂, ZrFe₂, and ZrCo₂. A computational cell extended by periodic boundary conditions was used to describe a material of infinite extent. A cubic computational cell of A₈B₁₆ in the C15 structure was used for all calculations. *k-space* was sampled using 3×3×3 *k*-points positioned using the Monkhorst-Pack scheme. Results using larger numbers of *k*-points gave only very minor total energy differences from calculations with 3×3×3 *k*-points. A cutoff energy of 270 eV was used throughout. Geometries were optimized until the forces on all unconstrained atoms were less than 0.03 eV/Å. Unless otherwise specified, all atoms were allowed to relax during geometry optimizations.

For interstitial H in ZrX₂ we first optimized the C15 lattice constant in the absence of H. This gave lattice constants of 7.32, 7.12, 7.00, 7.06, and 6.90 Å for ZrV₂, ZrCr₂, ZrMn₂, ZrFe₂, and ZrCo₂ respectively. These compare well with the experimentally established lattice constants of 7.45, 7.21, 7.14, 7.07, and 6.95 Å¹⁴⁻¹⁷. All calculations for interstitial H in these materials were performed by placing a single H atom in the computational supercell, corresponding to a net stoichiometry of AB₂H_{0.125}.

Transition states for hopping of H between adjacent interstitial sites were determined using the Nudged Elastic Band (NEB)¹⁸ method. All atoms were allowed to relax during these calculations. Following convergence of the NEB calculations, the configuration most closely approximating a transition state was geometry optimized using a quasi-Newton algorithm that converges to critical points on the potential energy surface for starting points sufficiently close to a critical point. This procedure allowed the precise location of the transition states.

Vibrational frequencies for H in local minima and at transition states were calculated by assuming these frequencies are decoupled from metal atom vibrations. With this approximation, the metal atoms were constrained in the geometry associated with the minimum or transition state of interest and the Hessian matrix for local motion of the H atom was estimated using finite difference methods. This resulted in three real frequencies at each local minimum and two real frequencies at each transition state.

The local hopping rates between adjacent pairs of interstitial sites were predicted using the semiclassical corrected transition state formalism of Ferrman and Auerbach¹⁹. This formalism includes tunneling contributions and zero point effects but, crucially, only requires the energies and vibrational frequencies of H at the energy minima and transition state. Once the local hopping rates for each possible transition are known, an analytic expression exists to define the net diffusion coefficient of H in the C15 crystal structure²⁰.

Results and Discussions

The first step in describing the dynamics of interstitial H in Laves phase intermetallics is to calculate the binding energy of interstitial H in different environments in these materials. For all compounds, we examined H in all three interstitial sites described earlier. The adsorption and hence the site preference for H in C15 AB₂ intermetallics with A = Zr has been studied previously using DFT within the local density approximation (LDA) by Hong et al.²¹ These calculations predicted that the g site is the most stable site for ZrV₂ and ZrCr₂ while the e site is the most stable site for ZrMn₂, ZrFe₂, and ZrCo₂. Our DFT-GGA calculations yield a slightly different result, namely that the g site is favored in all of these materials except ZrCo₂. This prediction is the same regardless of whether zero point corrections are included in the site binding energies. In all cases studied, the binding energies are very similar for both the e and the g sites. The b site formed by 4A atoms, however is found much less favored of all tetrahedral sites thus in our diffusion model we neglect diffusion from and into these sites. H

diffusion among e and g sites in C15 AB₂ materials involves two distinct types of hops between g sites, hops from g to e sites, and the reverse e to g hop. After determining the stable adsorption sites for H adsorption, we used DFT to characterize each of these hopping barriers for all the materials listed above.

We first consider H diffusion in C15 ZrCr₂, where we can compare our results with extensive experimental data. The predicted self diffusivity of H in ZrCr₂ both with and without tunneling contributions is shown in Fig. 1, along with experimental data for ZrCr₂H_{0.2} from Renz et al.⁷ As shown in Fig. 1 harmonic TST alone is clearly incompatible with the complete set of experimental data. Including tunneling corrections, however, accurately captures the change in apparent activation energy that is observed as T is varied. Fitting our predictions to the standard Arrhenius expression, $D = \nu \exp(-E/kT)$, in the same T ranges as the experimental analysis of Majer⁹ yields $E = 0.161$ eV for $T > 260$ K and 0.049 eV for $T < 170$ K. The experimental values are $E = 0.167$ and 0.046 eV, respectively. An alternative analysis⁷ is to fit the entire data set to $D = \nu_1 \exp(-E_1/kT) + \nu_2 \exp(-E_2/kT)$. Experimentally, this yields $E_1 = 0.146$ - 0.157 eV and $E_2 = 0.021$ - 0.039 eV for ZrCr₂H_x with $x = 0.2$ - 0.5 . Analyzing our data in the same way for the same range of T gives $E_1 = 0.172$ eV and $E_2 = 0.049$ eV. While the predicted activation energies are in good agreement with experiment, it is clear from Fig. 1 that the pre-exponential factor associated with diffusion is overestimated by our computational methods.

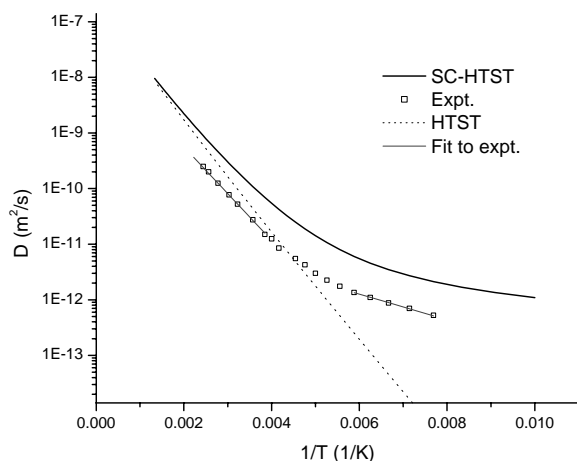


Figure 1. The net self diffusion rate for H in ZrCr₂ as predicted by harmonic transition state theory (HTST), semiclassically corrected harmonic transition state theory (SC-TST), and as measured experimentally by Renz et al.⁷. The fits to the experimental data in the low and high temperature regime reported by Majer⁹ are also shown.

Similar to ZrCr₂, the temperature dependent diffusivities for H were predicted in ZrFe₂, ZrMn₂, ZrCo₂, and ZrV₂ including tunneling contributions. In each case, the rates of each possible hopping event were computed with the DFT-based semiclassical approach defined above and the net diffusion rate was found using the analytic expression that combines the individual rates. At room temperature and above, tunneling contributions are negligible in all materials. At temperatures lower than 200 K, however, tunneling contributions become increasingly dominant. As with the case of ZrCr₂ discussed above, our theoretical calculations predict the activation energy of H diffusion with a high degree of accuracy.

Conclusions

We have shown that a combination of plane wave DFT calculations and semiclassically corrected harmonic transition state theory provides a useful description of hydrogen diffusion rates in complex metal alloys. We have demonstrated this method by analyzing all possible hops within five different C15 AB₂ intermetallics. Crucially, this approach is well suited to describing complex alloys in which large numbers of distinct site to site hops must be characterized. We anticipate that this method will be very useful in describing the diffusion of hydrogen in complex metal alloys and intermetallics.

Acknowledgements. This work was partially supported by the Department of Energy Coal Research Program. DSS is an NETL Faculty Fellow.

References

- (1) Kamakoti, P.; Sholl, D. S. *J. Membrane Sci.* **2003**, *225*, 145.
- (2) Kamakoti, P.; Morreale, B. D.; Ciocco, M. V.; Howard, B. H.; Killmeyer, R. P.; Cugini, A. V.; Sholl, D. S. *Science* **2005**, *307*, 569.
- (3) Kamakoti, P.; Sholl, D. S. *Phys. Rev. B* **2005**, *71*, 014301.
- (4) Sundell, P. G.; Wahnstrom, G. *Phys. Rev. Lett.* **2004**, *92*, 155901.
- (5) Sundell, P. G.; Wahnstrom, G. *Phys. Rev. B* **2004**, *70*, 081403.
- (6) Kallen, G.; Wahnstrom, G. *Phys. Rev. B* **2001**, *65*, 033406.
- (7) Renz, W.; Majer, G.; Skripov, A. V.; Seeger, A. *J. Phys. Cond. Mat.* **1994**, *6*, 6367.
- (8) Skripov, A. V.; Pionke, M.; Randl, O.; Hempelmann, R. *J. Phys. Cond. Mat.* **1999**, *11*, 1489.
- (9) Majer, G. *Mat. Res. Soc. Symp. Proc.* **1998**, *513*, 109.
- (10) Majer, G.; Kaess, U.; Stoll, M.; Barnes, R. G.; Shinar, J. *Defect and Diffusion Forum* **1997**, *143-147*.
- (11) Eberle, U.; Majer, G.; Skripov, A. V.; Kozhanov, V. N. *J. Phys. Cond. Mat.* **2002**, *14*, 153.
- (12) Skripov, A. V.; Combet, J.; Grimm, H.; Hempelmann, R.; Kozhanov, V. K. *J. Phys. Cond. Mat.* **2000**, *12*, 3313.
- (13) Kresse, G.; Furthmuller, J. *J. Comp. Mat. Sci.* **1996**, *6*, 15.
- (14) Pebler, A.; Gulbransen, E. A. *Trans. Met. Soc. AIME* **1967**, *239*, 1593.
- (15) Pedziwiatr, A. T.; Craig, R. S.; Wallace, W. E.; Pourarian, F. *J. Solid State Chem.* **1983**, *46*, 336.
- (16) Jacob, I.; Davidon, D.; Shaltiel, D. *J. Magn. Magn. Mater.* **1980**, *20*, 226.
- (17) Miron, N. F.; Shcherbak, V. I.; Bykov, V. N.; Levdi, V. A. *Sov. Phys. - Crystallogr.* **1971**, *16*, 266.
- (18) Henkelman, G.; Uberuaga, B. P.; Jónsson, H. *J. Chem. Phys.* **2000**, *113*, 9901.
- (19) Fermann, J. T.; Auerbach, S. *J. Chem. Phys.* **2000**, *112*, 6787.
- (20) Sholl, C. A. *J. Phys. Cond. Mat.* **2005**, *17*, 1329.
- (21) Hong, S.; Fu, C. L. *Phys. Rev. B* **2002**, *66*, 094109.